Proceedings
Compte-rendus

CNA/CNS Student Conference
ANC/SNC Conference d'etudiants

1990

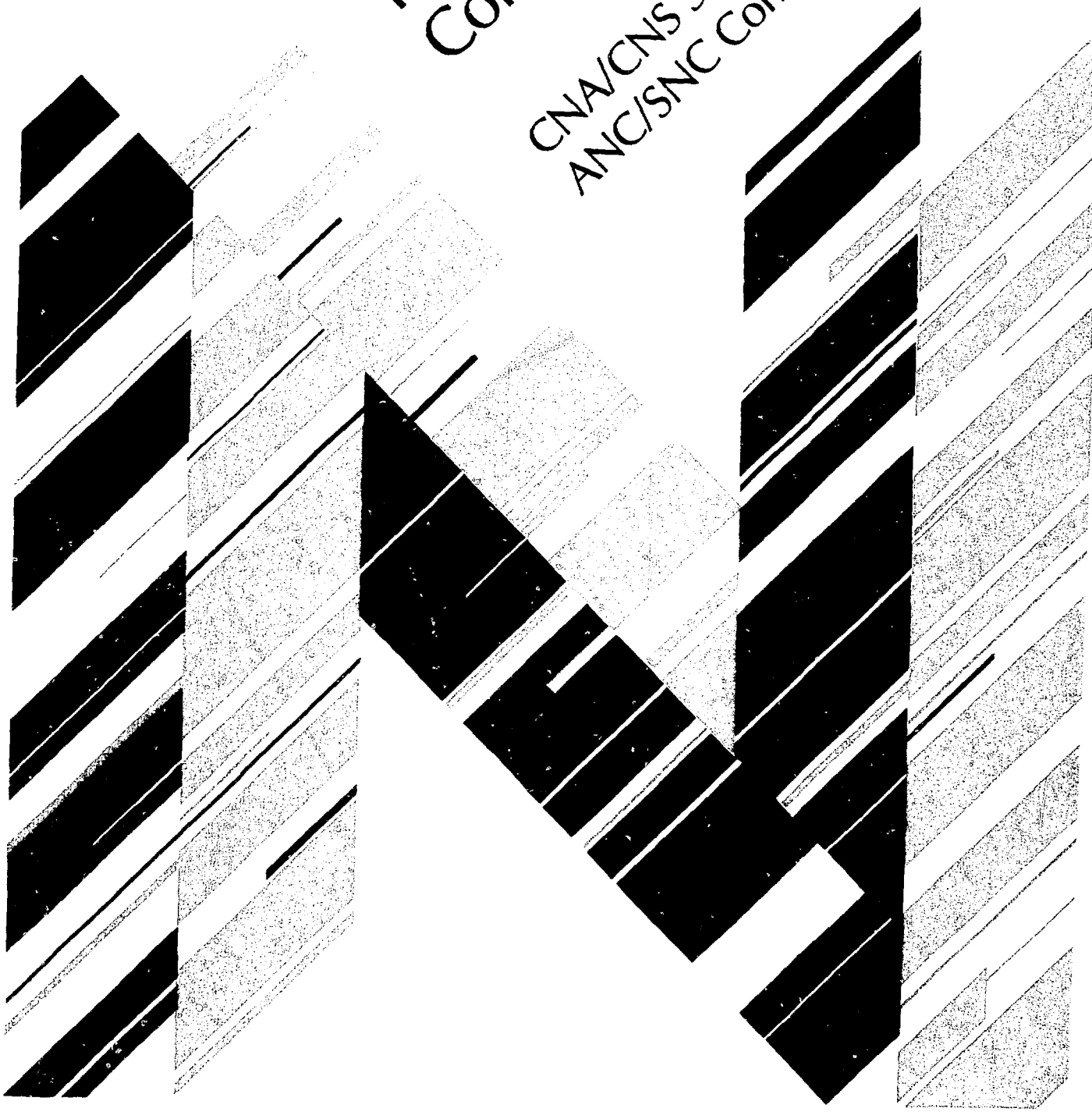

CNA/CNS Student Conference
ANC/SNC Conference d'etudiants

Proceedings
Compte-rendus

Editor
Editeur

J.W. Jury

Organizing Committee
Comite d'organization

J.W. Jury, Trent University
Ed Adams (G.E. Canada) (Ret.))
Ken Garrow, Trent University
Dan Meraw, Ontario Hydro

Sponsors
Organizateurs

Canadian Nuclear Assoc./Assoc. Nucleaire Canadienne
Canadian Nuclear Society/Societe Nucleaire Canadienne

Dates

23-24 March 1990
23-24 le mars 1990

Location

Trent University, Peterborough, Ontario, Canada

Contents
Table des matières

	Page Number
Table of Contents/Table des matières	i
Schedule/l'horaire	iii
Session/Séance I Reactor Systems and Fuel I	
Christopher J. Westbye, University of Toronto BOILING HEAT TRANSFER AND TWO-PHASE FLOW UNDER MICROGRAVITY CONDITIONS	1
A.L. Jorgensen, Royal Military College of Canada MEASUREMENTS FOR AN APPROACH-TO-CRITICAL EXPERIMENT FOR THE SLOWPOKE-2	10
P. Tye, Ecole Polytechnique de Montréal AN ANALYSIS OF THE LATERAL VOID TRANSFER MECHANISMS IN THE ASSERT SUBCHANNEL CODE	16
Izundu F. Obinelo, McMaster University THE EFFECT OF PULSED STEAM FLOW ON REFLUX CONDENSATION PHENOMENA IN A NUCLEAR STEAM GENERATOR	26
Session/Séance II Reactor Systems & Fuel II	
Michael A. Graf, University of Toronto THE MANUFACTURE AND ANALYSIS OF A REFERENCE DEFECT FOR HIGH FREQUENCY ULTRASONIC INSPECTIONS OF CANDU PRESSURE TUBES	40
C.B. Kwok, M.S. Mathur & J.S.C. McKee, University of Manitoba PLASMA INTERACTION WITH THE REFRACTORY MATERIALS INSIDE A FUSION REACTOR	45

Session/Séance III Applied Nucleonics

Matthew M.C. Ko, University of Toronto 57
TRACE ANALYSIS OF EMISSIONS FROM HOSPITAL INCINERATORS

M. Mirzai, University of Manitoba 72
COMPARTMENTAL MODELING OF HMPAQ AND CALCULATION OF REGIONAL CEREBRAL BLOOD FLOW

Ken Garrow, Queen's/Trent University 82
INSTRUMENTATION OF A HIGH ENERGY PROTON DETECTOR AND THE PHOTON TAGGER AT SAL

Guy Desnoyers, Royal Military College of Canada 89
NEUTRON DOSIMETRY USING BUBBLE DETECTORS AND AN ANTHROPOMORPHIC PHANTOM

Session/Séance IV Simulation Theory & Thermohydrolics

G.P. Cottingham, Royal Military College of Canada 103
A REAL-TIME SIMULATOR FOR THE SLOWPOKE-2

Glenn Harvel, McMaster University 116
MODELLING OF SINGLE PHASE NATURAL CIRCULATION FOR THE MAPLE - MNR REACTOR

Nirmala Arifin, University of Toronto 126
CRITICAL HEAT FLUX ON HORIZONTAL CYLINDERS IN A CROSS FLOW

A.A. Mirzai, University of Manitoba 139
X-RAY SPECTRUM ANALYSIS USING FOURIER TRANSFORM TECHNIQUES

R. Dowlati, University of Toronto 149
THE EFFECT OF BUNDLE GEOMETRY ON VOID FRACTION AND FRICTION PRESSURE DROP IN ADIABATIC TWO-PHASE FLOW ACROSS A HORIZONTAL ROD BUNDLE

Schedule
L'horaire

TRENT UNIVERSITY

CNS/SNC ANC/CNA

STUDENT CONFERENCE 1990 CONFERENCE d'ETUDIANTS

MARCH 23-24, 1990 MARS

FINAL PROGRAM

FRIDAY, MARCH 23

12:00-13:30 Registration/Inscription
(Champlain College Council Chamber, Trent University)

13:30 Welcome/Mot de bienvenue:

Prof. J.W. Earnshaw
Vice President
Trent University

13:45 Session/Séance I Reactor Systems and Fuel I
(Champlain College Council Chambers)

Chair/President: Prof. J.W. Jury, Trent University

Speakers/Conférenciers:

C.J. Westbye	University of Toronto	Boiling Heat Transfer & Two-Phase Flow Under Microgravity Conditions
A. Jorgensen	Royal Military College	Measurements for an Approach to Critical Experiment on the Slowpoke-2
P. Tye	Ecolé Polytechnique	An Analysis of the Lateral Void Transfer Mechanism in the ASSERT Subchannel Code
I. Obinelo	McMaster University	Steam Condensation in a Nuclear Steam Generator Under Reflux Condensation Mode

15:15	Coffee/Café		
15:45	Session/Séance II Reactor Systems & Fuel II (Champlain College Council Chamber) Chair/President: Mr. Ed Adams, Consultant & General Electric of Canada Nucl. Prod. (Ret).		
M. Graf		University of Toronto	Manufacture and Analysis of a Reference Defect for High Frequency Ultrasonic Inspection of CANDU Pressure Tubes
C.-B. Kwok		University of Manitoba	Plasma Interaction with the Refractory Materials Inside a Fusion Reactor
17:30-18:30	Check in at Red Oak Inn Hotel in Peterborough		
18:30-19:00	Cash Bar at the Red Oak Inn		
19:00	Banquet at the Red Oak Inn Guest Speaker: Mr. Dennis McQuade Technical Manager Darlington Nuclear Generating Station		

Saturday, March 24, 1990

08:30	Session/Séance III Applied Nucleonics (Champlain College Council Chamber) Chair/Président: Mr. Dan Meraw Ontario Hydro		
M.M.C. Ko		University of Toronto	Trace Analysis of Emmisions from Hospital Incinerators
M. Mirzai		University of Manitoba	Compartmental Modelling of HMPAQ and calculation of Regional Cerebral Blood Flow

K. Garrow	Trent University	Development of Energy-loss Proton Detectors
G. Desnoyers	Royal Military College	Neutron Dosimetry Using Bubble Detectors and an Anthropomorphic Phanton

09:45 Coffee/Café

10:10 Session/Séance IV Simulation Theory & Thermohydrolics
(Champlain College Council Chambers)

Chair/Président: Prof. Hughes Bonin
RMC and Representation of the CNS

G. Cottingham	Royal Military College	A Real-Time Simulator of the Slowpoke-2 Reactor
G. Harvel	McMaster University	Modelling of Natural Circulation for the Maple-MNR Reactor
N. Arifin	University of Toronto	A Review of Critical Heat Flux in Two-Phase Flow
A.A. Mirzai	University of Manitoba	Development of an Automated X-Ray Spectrum Analysis System Using Fourier Transform Technique
R. Dowlati	University of Toronto	The Effect of Bundle Geometry on Void Fraction and Friction Pressure Drop in Adiabatic Two-Phase Flow Across a Horizontal Rod Bundle

11:50 End of Session

12:00 Depart for Darlington Nuclear Generating Facility

13:00 Arrive Darlington

13:15 Lunch at Darlington
(Awards for best papers and introduction to Darlington NGS

14:00 Site tour of Darlington

16:00 END OF CONFERENCE.

Boiling Heat Transfer and Two-Phase Flow Under Microgravity Conditions

by

Christopher J. Westbye
Dept. of Chemical Engineering & Applied Chemistry
University of Toronto
Toronto, Ontario M5S 1A4

Modelling of two-phase flow patterns and flow regime transistions during quenching processes in microgravity is an essential step in the development of space-based nuclear reactors, or nuclear propelled space vehicles. To investigate these phenomena, a compact experimental test platform was designed and constructed. It consists of a positive displacement pump which forces freon-113 through a heated quartz tube. The vapour is then condensed and returned to the pump. Thermocouples placed along the length of the quartz tube record the progress of the quench front and indicate heat transfer characteristics, while various photographic equipment record the flow pattern. Preliminary ground testing of the apparatus provides reference data, and microgravity tests aboard a NASA KC-135 aircraft will be performed in June 1990.

There are many important processes that occur under microgravity which would involve gas-liquid two-phase flow and boiling/condensation heat transfer phenomena. In refilling of Space Transfer Vehicles with liquid hydrogen/oxygen fuel under microgravity, a transient quenching process is expected involving liquid-vapour two-phase flow and convective boiling heat transfer due to the low boiling points of the fluids and high initial wall temperatures of the refueling lines and receiving tanks. Similar phenomena are also expected in the emergency cooling of space nuclear power or propulsion reactors under loss-of-coolant accident conditions, transfer and storage of cryogenic fluids and processing of certain materials on the space station.

In the past, only few studies on two-phase flow under microgravity have been conducted (see References). Several researchers have used the NASA KC-135 aircraft to simulate zero-gee conditions in the study of two component, adiabatic two-phase flow. However, these results are not directly applicable to the transient, diabatic quenching flow situations described above.

The flow patterns existing under quenching conditions

are quite different from those observed under adiabatic, or even boiling but non-quenching conditions. Typically, inverted annular flow and dispersed flow patterns occur with film boiling heat transfer characteristics that are highly dependent on the hydrodynamics. Since the two-phase flow patterns existing under microgravity are yet relatively unknown, but are expected to strongly affect both precursory cooling and quenching rates, it is important to conduct such an experiment to elucidate their behaviour under microgravity conditions.

To this end, a series of quenching experiments will be performed on board the KC-135 to investigate the two-phase flow and convective boiling heat transfer phenomena which occur during rapid cooling and quenching of a hot quartz tube under microgravity.

A compact test loop has been constructed incorporating a transparent, 12.0 mm I.D., 1.2 m long quartz tube test section which is heated externally by a nichrome heating tape connected to an AC powerstat. The working fluid is freon-113 (R-113), chosen for it's low boiling point (47.6 °C). A positive displacement pump, consisting of a piston cylinder connected to a DC motor driven linear actuator, is used to inject the coolant into the test section. Varying the DC input voltage to the linear actuator controls the flow rate, and flow rates in the range from 2.6 to 20 mL/sec can be obtained. The pump is designed to be used in a "one-shot" manner, since the KC-135 only develops microgravity conditions for 20 to 30 seconds during each parabola. After exiting the test section, the freon vapour is condensed in an ice condenser. The condenser consists of ten rectangular hollow copper fins filled with ice, contained in a lucite housing. The transparent lucite allows for future condensation visualization studies in microgravity. The condensed freon is collected in a reservoir at the bottom of the condenser, and is ready to be used for another run. See Figure 1 for a schematic diagram of this apparatus.

A pressure transducer is located at the test section outlet to record the maximum pressure rise. A number of type T thermocouples are located along the test section to measure the wall temperature response. The wall temperature data will be examined to study the effect of gravity on precursory cooling and quenching characteristics. The quenching velocities, as functions of gravity, initial wall temperature and coolant flow rate will be computed from the time histories of wall temperature responses for each run.

In addition, a 35mm still camera, a video camcorder and a 16mm movie camera are installed at various positions along the test section to record the two-phase flow patterns prevailing during the experiment. The photographs, video films and 16mm movie films will be studied in detail in order to determine the flow patterns that occur at various

axial positions downstream of the quench front, and the heat transfer characteristics obtained from the thermocouple data will be related to the two-phase flow characteristics.

To date, only some preliminary ground tests have been performed. With the test section in a horizontal orientation, data from seven thermocouples and a pressure transducer have been acquired using a chart recorder for various flow rates (6 to 10.9 mL/sec) and initial wall temperatures (360 to 430°C).

As the freon enters the test section, it immediately vapourizes to form a vapour barrier which prevents the liquid from quenching the tube. Film boiling continues until enough heat has been removed from the quartz tube by convection to allow the liquid to come into contact with the wall. At this point, the wall temperature decreases rapidly and quenching is said to have begun. The quench front moves along the tube from inlet to outlet until the entire tube has been cooled to the bulk temperature of the fluid. Since the test section is horizontal, the top half of the tube never comes directly in contact with the liquid coolant, and heat is removed by the much more inefficient mechanisms of convection and conduction through the tube wall. See Figure 2 for a comparison of the temperature profiles from two thermocouples, one mounted at the top of the tube and one at the bottom, at the same axial location. For a vertical test section, or in microgravity, inverted annular flow is expected until quenching is initiated.

For constant flowrate, an increase in initial wall temperature causes the onset of quenching to be delayed. The results gathered suggest that quenching is initiated when the wall reaches a particular temperature, dependent only on the flow rate and not on the initial conditions (see Figure 3). When the initial conditions are constant but the flow rate increases, quenching seems to be initiated earlier, although this effect is small for the flow rates examined (Figure 4).

The pressure transient resulting from the quenching process was also examined. It took some time (about 10 seconds) from the moment of injection before any pressure change was recorded. The pressure then increased rapidly to it's maximum value, 0.7 psig (6.9 kPa) for a flow rate of 8.9 mL/s and an average wall temperature of 350 °C. The pressure then fell slowly as the gaseous freon condensed. See Figure 5 for the pressure response. In microgravity, larger pressure rises are expected because the entire tube wall is in contact with the freon, producing more vapour, and because there is no gravity to cause condensed liquid to flow off of the fins, reducing the condensing surface area.

To complete the ground tests, more thermocouples will be attached to the test section and their output read directly by a data acquisition system. This will provide

more detailed numerical results, and facilitate analysis. Also, experiments will be performed in a vertical configuration. Finally, in June 1990 the experiment will be flown on the KC-135 in Houston under the same boundary conditions to allow direct comparison to the 1-g results. The post-flight data analysis should yield valuable information on the effects of gravity, initial wall temperature, liquid injection rate and liquid subcooling of the two-phase flow, precursory cooling heat transfer and quenching phenomena.

References

J.A. Bamberger, J.M. Bates et al., "Understanding Boiling and Condensation in Microgravity: The Test Bed Approach", AIChE Symposium Series, No 269 vol 85, 1989.

I.Y. Chen, R.S. Downing, "A Reduced Gravity Flight Experiment: Observed Flow Regimes and Pressure Drops of Vapor and Liquid Flow in Adiabatic Piping", AIChE Symposium Series, No 263 vol 84, 1988.

A.E. Dukler, J.A. Fabre et al., "Gas-Liquid Flow at Microgravity Conditions: Flow Patterns and their Transistions", International Journal of Multiphase Flow, Vol 4 No 4, 1988.

D.B. Heppner, C.D. King et al., "Zero-G Experiments in Two-Phase Fluids Flow Regimes", ASME paper 75-ENAs-24, 1975.

L. Kachnik, D. Lee et al., "A Microgravity Boiling and Convective Condensation Experiment", ASME paper 87-WA/HT-12, 1987.

K.S. Rezkallah, C.S. Huckerby, "Microgravity Two-Phase Experiments for Spacecraft Thermal Control Studies", AIChE Symposium Series, Vol 269 No 85, 1989.

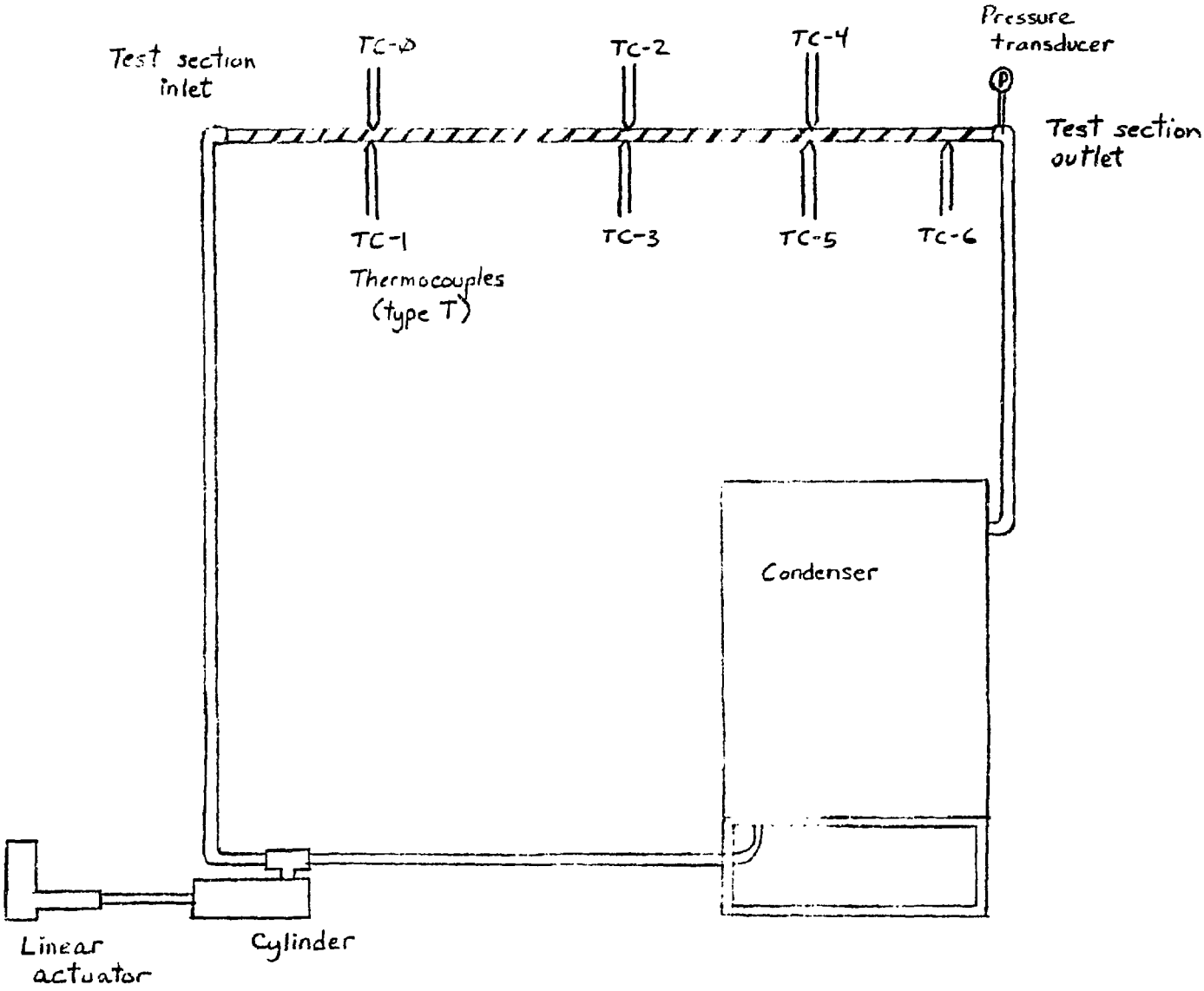

Experimental Apparatus
Schematic Diagram

Figure 1

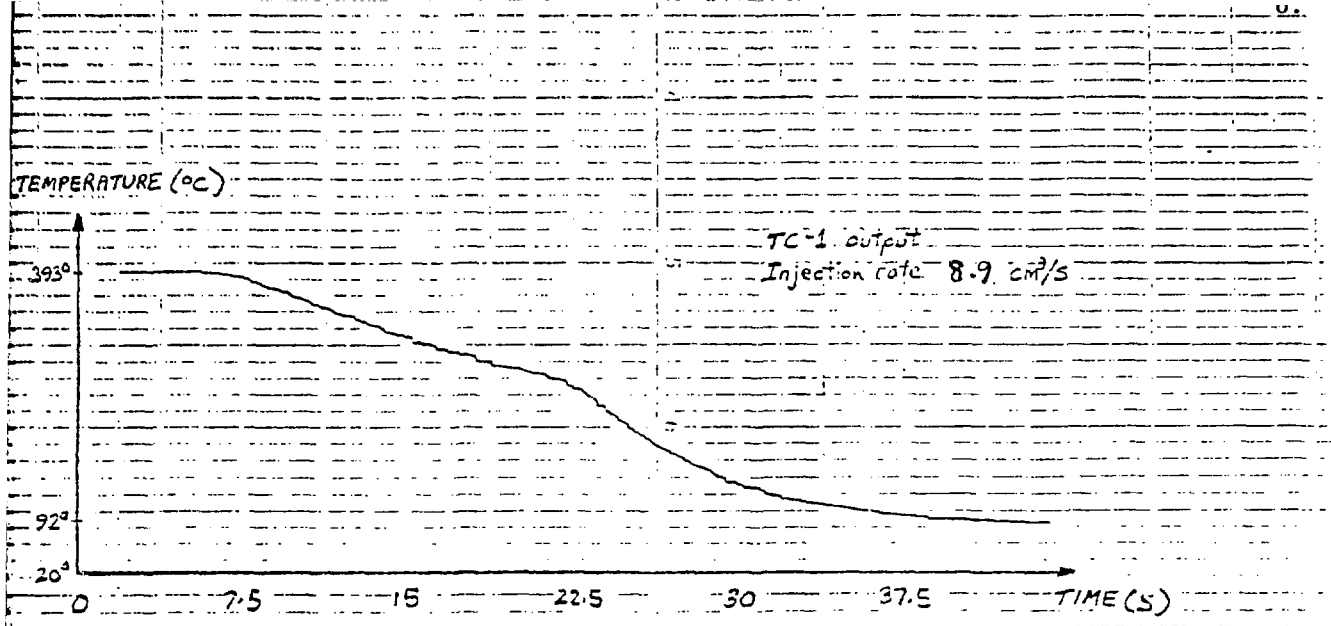

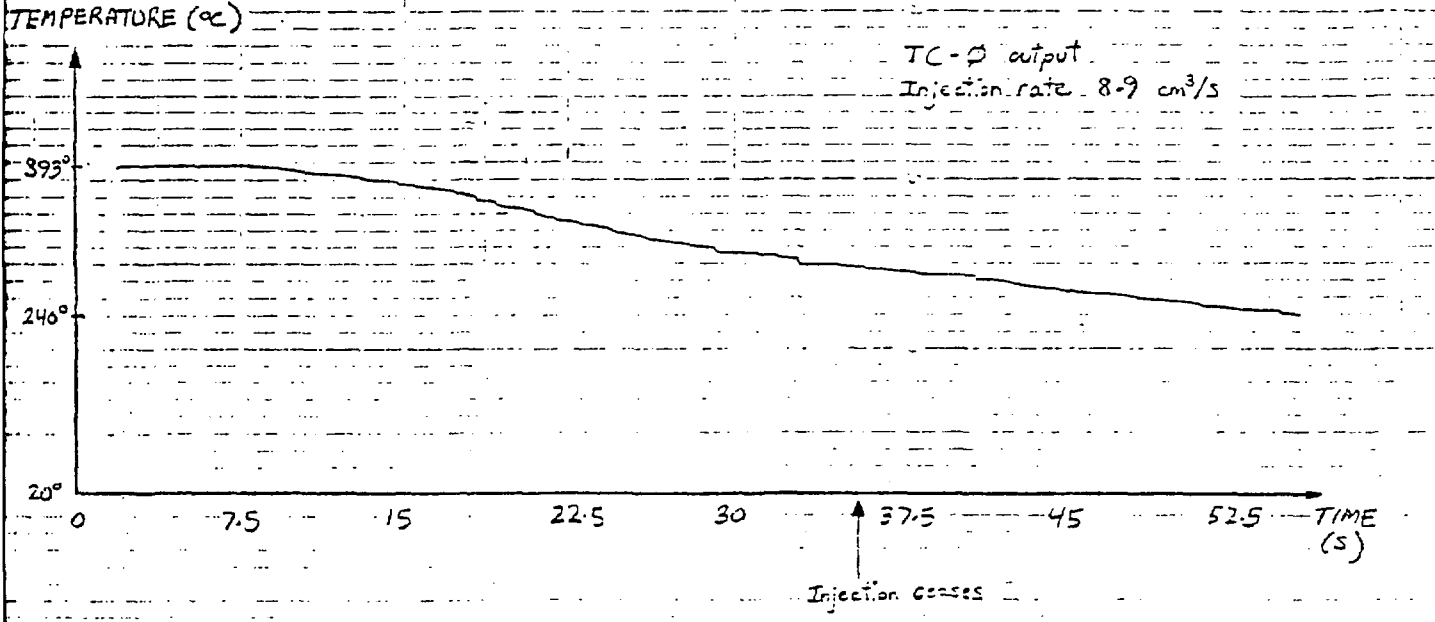

Figure 2: Comparison of temperature response from bottom and top of quartz tube at same axial location

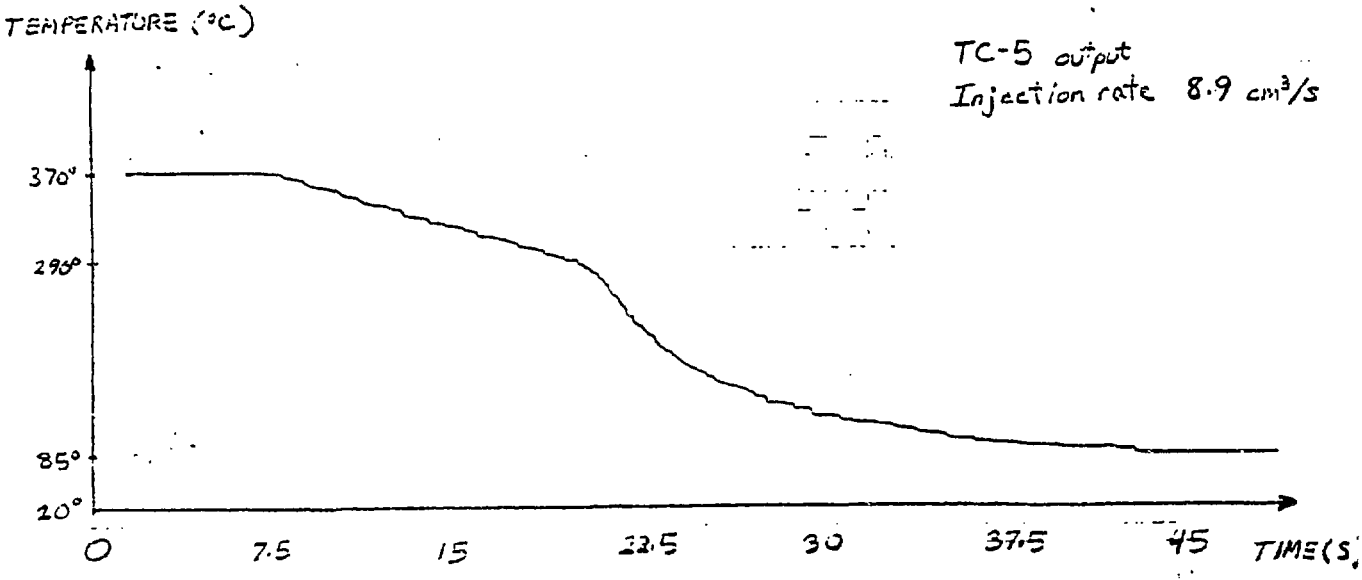

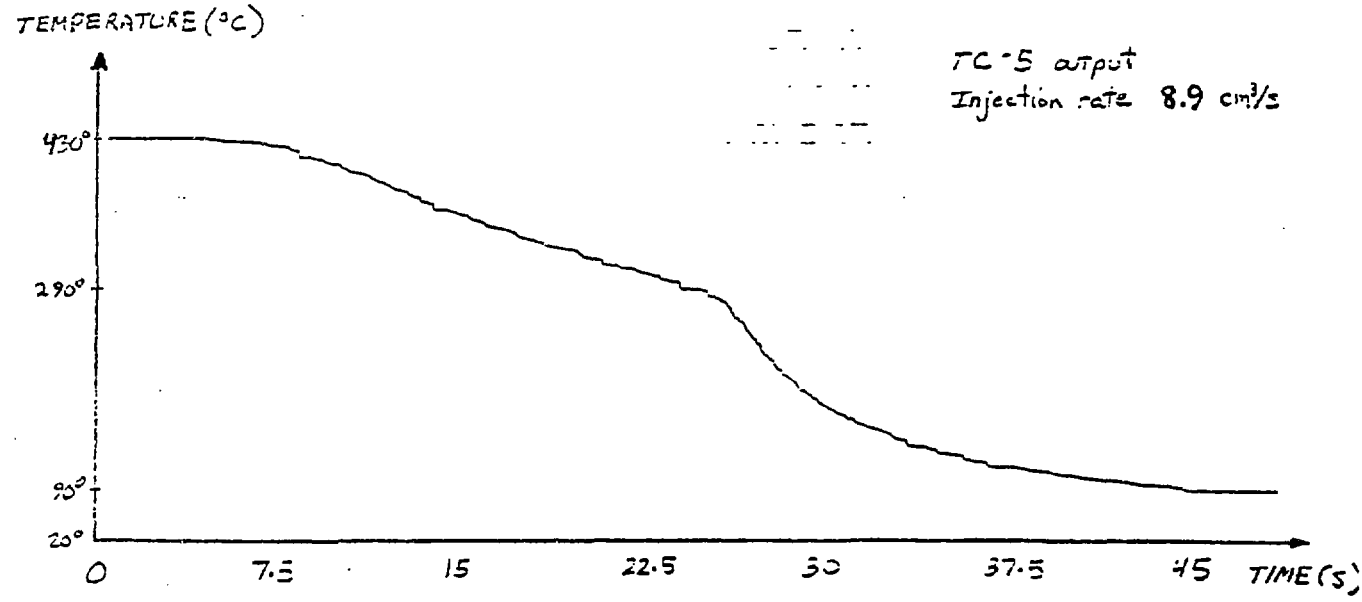

Figure 3: Comparison of quench rates for different initial temperatures

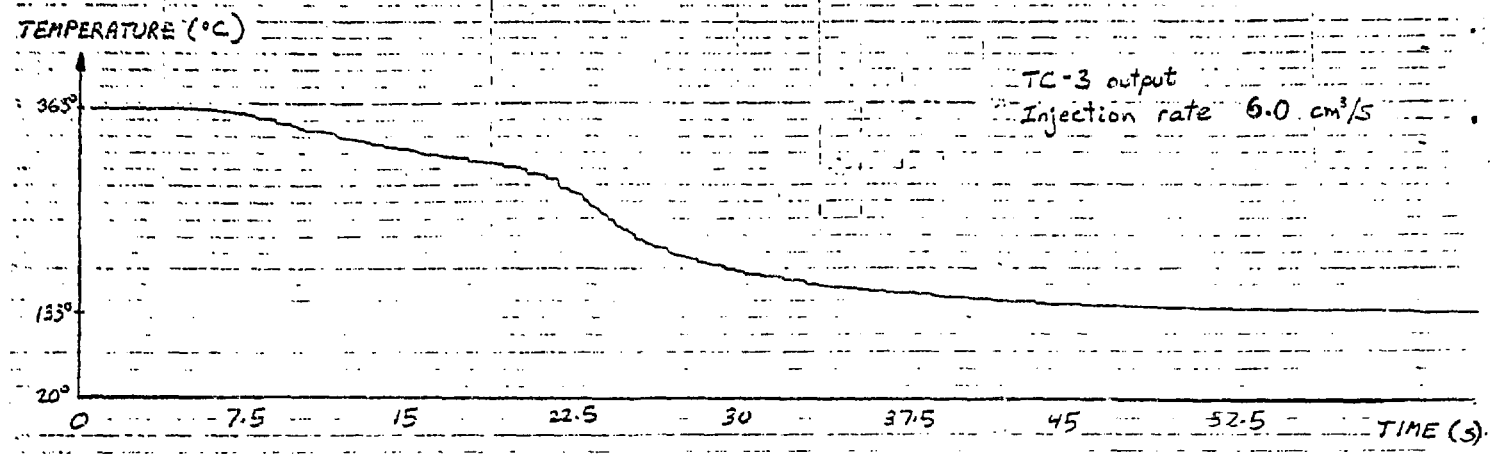

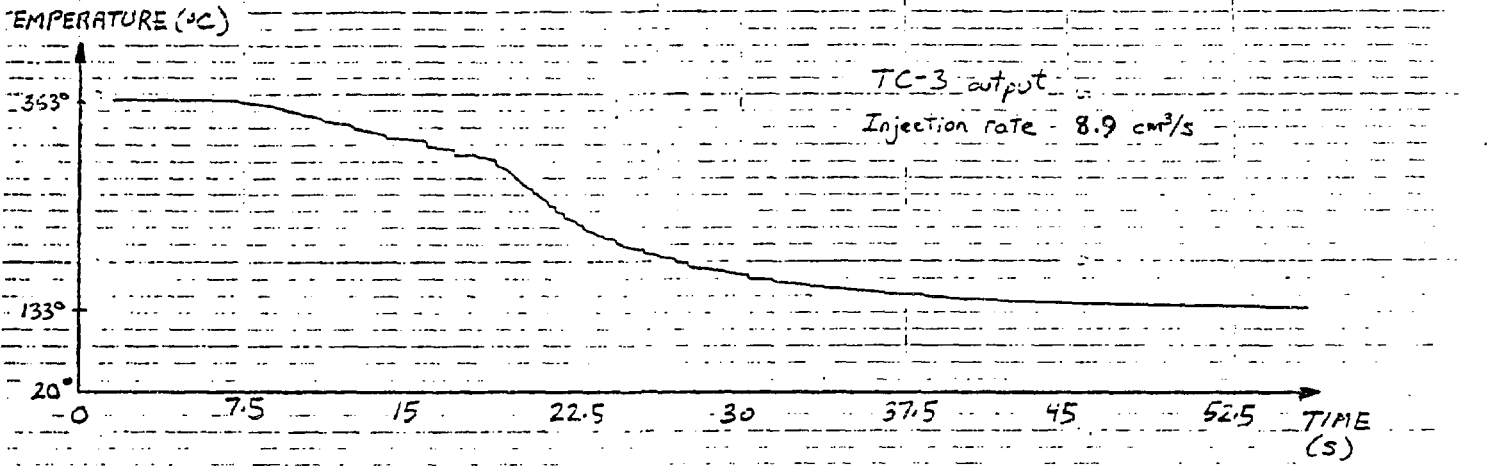

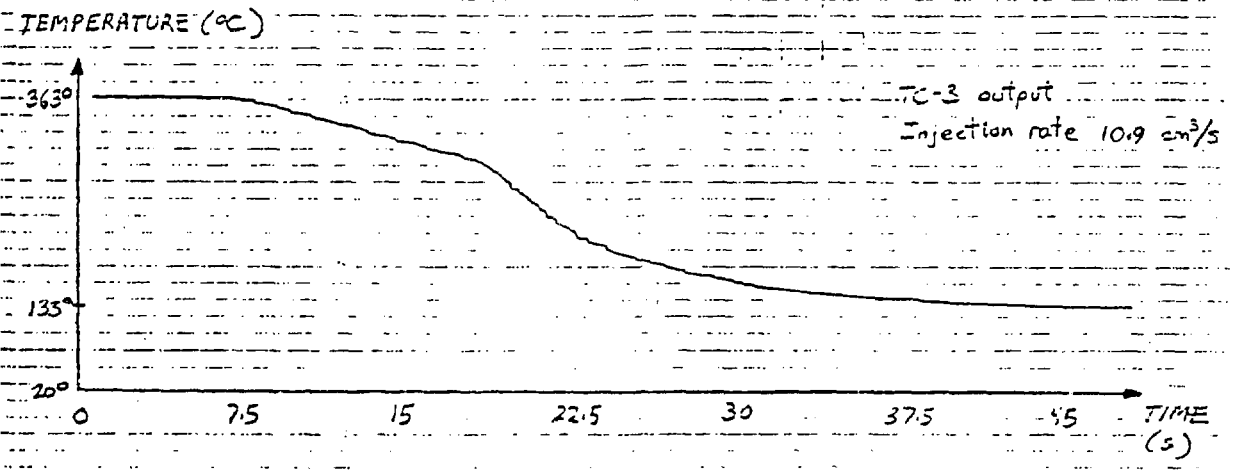

Figure 4: Variation of temperature profile with flowrate

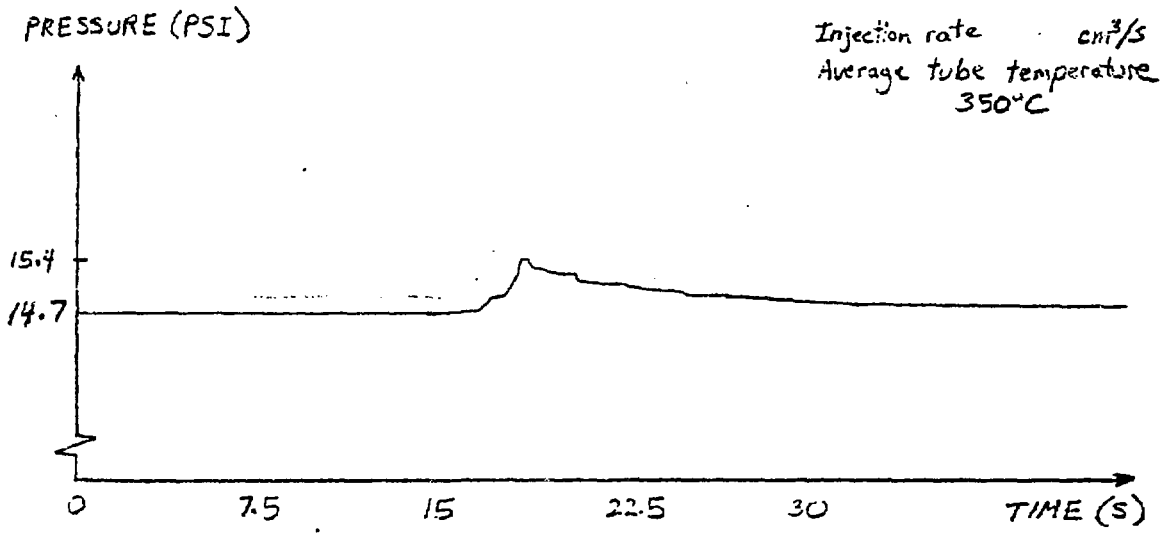

Figure 5: Pressure response

MEASUREMENTS FOR AN APPROACH-TO-CRITICAL EXPERIMENT FOR THE SLOWPOKE-2

A.L. JORGENSEN
DEPARTMENT OF CHEMISTRY AND CHEMICAL ENGINEERING
ROYAL MILITARY COLLEGE OF CANADA

The approach-to-critical experiment is being devised as an undergraduate laboratory experiment. As part of the development the neutron flux available from ^{252}Cf sources and the reactor core itself after shutdown was studied as possible sources for the experiment. Also the means of simulating fuel addition by the withdrawal of cadmium capsules or the control rod were studied.

INTRODUCTION:

The SLOWPOKE-2 is a small, light water, pool type research reactor designed by the Atomic Energy of Canada Limited (AECL). The advantages of the SLOWPOKE-2 for teaching are its relatively simple operation, small size, and accessibility. Because of these advantages, an approach-to-critical experiment can be easily performed at the undergraduate level.

For the approach-to-critical experiment, the reactor is to be operated at subcritical conditions. A neutron source is used to induce neutron multiplication from the fuel present. Cadmium capsules placed in the core are then

slowly removed or the control rod withdrawn to simulate the addition of fuel to the core. As fuel is "added" the inverse effective multiplication is plotted and the critical point is determined by extrapolation.

The neutron source to be used in the experiment has been studied. A number of ^{252}Cf sources and the core itself after shutdown have been measured by indium foil activation to determine their fluxes. The suitability of these sources will depend upon their relative strengths and location in the reactor pool with respect to the neutron detector.

Approach-to-Critical:

With a neutron source placed adjacent to fuel, neutron multiplication, k, occurs in the core. Multiplication, k can be defined as the ratio of the number of neutrons produced, due to the source and the fissions, to the number of neutrons produced due to the source only. If S neutrons are emitted from the source, then Sk neutrons will be produced at the end of one generation, Sk^2 at the end of the second generation and so on. Then the effective multiplication in the reactor will be:

$$\text{Multiplication} = \frac{S+Sk+Sk^2+\ldots}{S}$$

$$= 1/(1-k) \qquad k<1 \text{ subcritical}$$

As more fuel is added, or in this case simulated by fewer cadmium capsules or the control rod removed from the core, the core will approach critical. Hence k will tend towards unity and the effective multiplication will tend to infinity. Therefore if the reciprocal of the effective multiplication is plotted against the fuel mass and the plot is extrapolated to zero on the abscissa, the critical size or mass of the reactor can be found.(1)

INDIUM FOIL ACTIVATION:

In order to determine an appropriate neutron source (S) and its intensity, the neutron flux of the shutdown core and a ^{252}Cf source was measured. The activity of the indium foil can be expressed by the following equation:(2)

$$A=[(mCF_I)/M]NB(\phi_{th}\sigma_{th}+I_R\phi_{epi})(1-e^{-\lambda T_{irr}})e^{-\lambda T_d}(1-e^{-\lambda T_c})$$

where
- ε is the counting efficiency
- m is the mass of the foil irradiated
- C is the concentration of Indium in the foil
- F_I is the isotopic abundance of ^{115}In
- M is the atomic weight of ^{115}In
- λ is the decay constant for the radioactive species
- N is Avogadro's number
- B is the branching ratio
- ϕ_{th} is the thermal flux
- σ_{th} is the absorption cross section
- I_R is the resonance integral
- ϕ_{epi} is the epithermal flux
- T_{irr} is the irradiation time
- T_d is the decay time
- T_c is the counting time

The indium foils were placed in the reactor, after shut down, in four sites: an inner irradiation site, SITE 1; an elevator in the pool, placing the foil just below the beryllium annulus; SITE P1, a transfer system in the pool devised for the ^{252}Cf source to be placed near the core; and POOL, a site as close as possible to SITE P1 in the pool. The foils were counted using a ND66 Multichannel Analyzer with a HPGe detector and the spectra were analyzed by the Gamanal computer program.(3)

RESULTS:

The thermal flux, as measured by indium foil activation, of the ^{252}Cf source was found to be $4.6x10^{3}$ $n/cm^{2}s$. A smaller ^{252}Cf source which was a quarter of the strength of the measured source has then an estimated flux of $10^{3}n/cm^{2}s$. Another available ^{252}Cf source which was approximately 100 times stronger than the measured source would then have an estimated flux of $10^{5}n/cm^{2}s$. However, the average thermal flux of the core was found to be $10^{5}n/cm^{2}s$.

The thermal flux was measured at various times after the reactor was shut down. The flux after approximately 20 hours was measured to be $4x10^{6}n/cm^{2}s$ (an average of the three outer pool sites). The flux then decreased steadily and leveled off after approximately 50 hours after shutdown

at a flux of $10^5 n/cm^2 s$.

The worths of the cadmium capsules were determined from irradiations in SITE 1 and the control rod calibration curve to be about -1.2, -0.7 and -0.5 mk for cadmium sleeves full, 3/4 and 1/2 length in the irradiation capsules.

CONCLUSIONS:

The approach-to-critical experiment is feasible but has not yet been performed since the in pool borated ion chamber is not available.

The thermal flux of the core is much greater than that from the combination of all three ^{252}Cf sources. Therefore, the core itself can be used as the neutron source for the experiment.

Either withdrawal of the cadmium capsules or the control rod will simulate the fuel addition to the core. The worth of a 1/2 cadmium capsule and a 1/2" withdrawal of the control rod (up to 3.5") is identical at about -0.5 mk.

RECOMMENDATIONS:

Once the borated ion chamber is available for use the experiment can be performed with the cadmium capsules or the control rod for the simulation of fuel addition and the core flux as a neutron source.

REFERENCES:

(1) Glasstone, S. and A. Sesonske Nuclear Reactor Engineering. Van Nostrand & Reinhold: Toronto, 1981.

(2) Kennedy, G., J. Marcotte, L. Zikovsky. "An Activation Analysis System for Short Lived Radioisotopes including Automatic Dead-Time Corrections with a Microcomputer" Journal of Radioanalytical and Nuclear Chemistry. Articles, Vol. 110, No. 1 (1987) 61-66.

(3) Heimlich, M., P.A. Beeley, J.A. Page. "Gamanal-PC: A Program for Gamma-ray Spectrum Analysis using a Microcomputer" Journal of Radioanalytical and Nuclear Chemistry. Articles, Vol. 132, No. 2 (1989) 281-291.

(4) Lamarsh, J.R. Introduction to Nuclear Engineering Addison-Wesley Pub.: Don Mills, Ontario, 1975.

AN ANALYSIS OF THE LATERAL VOID TRANSFER MECHANISMS IN THE **ASSERT** SUBCHANNEL CODE

P. Tye
Institut de Génie Energétique
Ecole Polytechnique de Montréal
Montréal, Québec, Canada H3C 3A7

1. INTRODUCTION

The current aim of this research is to conduct the verification of the hydraulic aspect of subchannel codes. The experiments were conducted on two laterally interconnected horizontal bundle type subchannels [1] under adiabatic two-phase flow conditions. The two phase flow was a mixture of air and water initially having a different void fraction in each subchannel. The main parameters measured in the channels were: void fraction, liquid and gas mass flow rates and pressures. Since, in horizontal two-phase flow the mass exchanges between interconnected subchannels are greatly influenced by the relative position of the high void channel (denoted HV) with respect to the low void channel (denoted LV), the former channel has been rotated to different positions about the latter one. The experimental results are compared with the predictions of the ASSERT-4 (Version 1.5) subchannel code [2 & 3] to ascertain how well they can be predicted.

2. ASSERT SUBCHANNEL CODE DESCRIPTION

The ASSERT subchannel code [2 & 3] has been developed to model single and two phase flows through vertical and horizontal rod bundles. ASSERT uses a 5 equation advanced drift flux model to account for the effect of thermal non-equilibrium as well as unequal phasic velocities. The relative velocity model has been used to account not only for the different velocities between the phases in the axial direction but also to model some of the lateral transport mechanisms which are important in subchannel flows. These mechanisms, as identified by different authors [2], are: Diversion Crossflow, Turbulent Void Diffusion, Void Drift and Buoyancy Drift.

2.1 Conservation equations

The discretized form of the equations solved by ASSERT are shown below.

Mixture Mass Conservation

$$A_{i,j}\frac{\rho_{i,j}-\rho^n_{i,j}}{\Delta t}+\frac{F_{i,j}-F_{i,j-1}}{\Delta z_j}+D_{ik}W_{k,j}=0 \qquad (1)$$

where, $\rho_{i,j}=(\alpha\rho)_{v_{i,j}}+(\alpha\rho)_{\ell_{i,j}}=\alpha_v\rho^+_{v_{i,j}}+\alpha_\ell\rho^+_{\ell_{i,j}}$

Mixture Momentum Conservation

Axial

$$A_{i,j}\frac{F_{i,j}-F^n_{i,j}}{\Delta t}+\frac{(FU)_{i,j}-(FU)_{i,j-1}}{\Delta z_j}+D_{ik}(WU^*)_{k,j}+\overline{A_{i,j}}\frac{P_{i,j}-P_{i,j-1}}{\Delta z_j}=$$

$$-\overline{A}(K|F|F)^\dagger_{i,j}-g\overline{A}\overline{\rho}_{i,j}\cos\theta \qquad (2)$$

where,

$$(WU^*) = WU^* + s\frac{(\alpha\rho)_v^*(\alpha\rho)_\ell^*}{\rho^*}U_r^*V_r^\dagger$$

Lateral

$$\frac{W_{i,j} - W_{i,j}^n}{\Delta t} + \frac{(W\overline{U})_{i,j}-(W\overline{U})_{i,j-1}}{\Delta z_j} + \left(\frac{s}{\ell}\right)_k D_{ik}P_{i,j-1} =$$

$$-\left(\frac{s}{\ell}\right)_k (C|W|W)_{i,j}^\dagger - g s_k \overline{\rho}_{i,j}\cos\phi_k \sin\theta \qquad (3)$$

where,

$$(W\overline{U}) = W\overline{U} + s\frac{(\overline{\alpha}\,\overline{\rho})_v(\overline{\alpha}\,\overline{\rho})_\ell}{\rho^*}\overline{U}_r V_r^\dagger$$

Mixture Energy Conservation

$$A_{i,j}\rho_{i,j}^n\frac{h_{i,j} - h_{i,j}^n}{\Delta t} + F_{i,j-1}\frac{h_{i,j}-h_{i,j-1}}{\Delta z_j} + \frac{f(\alpha,F)_{i,j} - f(\alpha,F)_{i,j-1}}{\Delta z_j} + D_{ik}(Wh^*)_{k,j} - h_{i,j}D_{ik}W_{k,j} =$$

$$(q_w)_{i,j}^{'\dagger} - D_{i,k}((\alpha q^{'})_v + (\alpha q^{'\dagger})_\ell)_{k,j} \qquad (4)$$

where,

$$f(\alpha,F) = (h_v - h_\ell)\frac{(\alpha\rho)_v(\alpha\rho)_\ell}{\rho}AU_r^\dagger$$

Phasic Energy

Liquid

$$A_{i,j}(\alpha\rho)_{\ell_{i,j}}^n\frac{h_{\ell_{i,j}} - h_{\ell_{i,j}}^n}{\Delta t} + F_{\ell_{i,j-1}}h_{\ell_{i,j}} - h_{\ell_{i,j-1}z_j} + D_{ik}(Wh^*)_{\ell_{k,j}} - h_{\ell_{i,j}}D_{ik}W_{\ell_{k,j}} =$$

$$(q_{w\ell}^{'})_{i,j}^\dagger - D_{i,k}(\alpha q^{'})_{\ell_{k,j}}^\dagger + q_{i\ell_{i,j}}^{'\dagger} \qquad (5)$$

Vapour

$$A_{i,j}(\alpha\rho)_{v_{i,j}}^n\frac{h_{v_{i,j}} - h_{v_{i,j}}^n}{\Delta t} + F_{v_{i,j-1}}\frac{h_{v_{i,j}} - h_{v_{i,j-1}}}{\Delta z_j} + D_{ik}(Wh^*)_{v_{k,j}} - h_{v_{i,j}}D_{ik}W_{v_{k,j}} =$$

$$(q_{wv}^{'})_{i,j}^\dagger - D_{i,k}(\alpha q^{'})_{v_{k,j}}^\dagger + q_{iv_{i,j}}^{'\dagger} \qquad (6)$$

Where † denotes variables that must be defined by constitutive relationships, + denotes variables defined by state relationships and * denotes donor values.

2.2 DRIFT FLUX MODEL

The relative velocity is modelled using the Ohkawa-Lahey full range drift flux model [4]. The relative velocity $\vec{V}_r$ is expressed in terms of the mixture volumetric flux $\vec{j}$:

$$\vec{V}_r = \frac{(C_0 - 1)\vec{j}}{(1-\alpha)} + \frac{\vec{V}_{gj}}{(1-\alpha)} - \frac{\varepsilon}{\alpha(1-\alpha)}\vec{\nabla}(\alpha - \alpha_0) \tag{7}$$

The first term on the right hand side accounts for the relative velocity due to cross sectional averaging. C_0, the phase distribution coefficient, is the correlating parameter. The second term represents the local relative velocity between liquid and vapour driven by gravity. The last term acconts for turbulent void diffusion and diffusion towards a prefered void distribution.

2.2.1 AXIAL RELATIVE VELOCITY

The axial relative velocity is modelled using only the first two terms of equation(7).

$$U_r = \frac{(C_0 - 1)j}{(1-\alpha)} + \frac{U_{gj}}{(1-\alpha)} \tag{8}$$

2.2.2 LATERAL RELATIVE VELOCITY

In the lateral direction the value of C_0 is assumed to be 1. Thus, the first term of equation (7) would be zero and only the last two terms are used to represent the lateral relative velocity.

$$V_r = \frac{V_{gj}}{(1-\alpha)} - \left(\frac{\varepsilon}{\alpha(1-\alpha)\ell}\right)\Delta_{i,j}(\alpha - \alpha_0) \tag{9}$$

The first term, the local relative velocity V_{gj} is expressed in terms of the terminal rise velocity of a bubble in an infinite medium V_∞,

$$V_{gj} = \bar{\alpha}(1-\bar{\alpha})^n V_\infty \quad , \tag{10}$$

The term $\bar{\alpha}(1-\bar{\alpha})^n$ is used to account for the presence of other bubbles, the recommended value of n is 0 [3], and V_∞ is given by[3]:

$$V_\infty = 2K_1\left(\frac{(\rho_\ell - \rho_g)}{\rho_\ell^2}\sigma g\right)^{0.25}\sin\phi \quad , \tag{11}$$

where σ is the surface tension and ϕ is the angle of the centroid to centroid connection measuring the inclination from the vertical and the recommended value of K_1 is equal to 2 [3]. The second term accounts for both the turbulent void diffusion and the void diffusion to a preferred void distribution. The void diffusivity, ε, is calculated from the Peclet number using the correlation:

$$P_e = \frac{\varepsilon}{\bar{U}\bar{D}h} = a\left(\frac{\alpha_m}{0.6}\right)^6 \quad , \tag{12}$$

where the recommended value of a is 0.075, $\bar{U}$ is the average mixture axial velocity of the adjacent subchannels i,j and $\bar{D}_h$ is the average hydraulic diameter of the adjacent subchannels, and α_m is

the maximum of the void in the two adjacent subchannels. Thus the lateral relative velocity is modelled using:

$$V_r = \frac{\left[4\bar{\alpha}\left(\frac{\rho_\ell - \rho_a}{\rho_\ell^2}\sigma g\right)^{0.25}\sin\phi - \frac{\varepsilon}{\bar{\alpha}\ell}\Delta\left(\bar{\alpha} - \bar{\alpha}_0\right)_{ij}\right]}{(1-\bar{\alpha})} \quad , \tag{13}$$

where $\bar{\alpha}$ is the average void fraction of the adjacent subchannels i,j.

3. COMPARISON OF ASSERT-4 PREDICTIONS AND DATA

Both experiments where simulated using ASSERT-4 (Version 1.5) with the default parameters for the coefficient a in the correlation used to determine the void diffusion term (Eq. 12) and the coefficient K_1 in the calculation of the terminal rise velocity of a bubble in an infinite medium (Eq. 11). A series of runs were done where the coefficent a in the void diffusion correlation was varied from 0.075 (default) to 0.25. It was observed that the default value lead to an under-prediction of the lateral void diffusion. Gencay [5] has calculated the value of the diffusion coefficient for a large number of experiments and has observed that the values of the diffusion parameter were larger than those obtained from the correlation used in ASSERT.

Further, results of simulations done suggest that the effect of gravity on the void transfer is over emphasized. The effects of gravity are taken into account in the calculation of the terminal rise velocity of the vapour bubbles. This correlation was developed for a single bubble rising in a stagnant infinite medium. It is well known that certain effects can act to decrease this terminal rise velocity [6], these are the presence of other bubbles, the presence of walls and the effects of a non-stagnant medium. Since, for our case, there are other bubbles and there are walls, in the form of a small gap, as pointed out by Carver et.al.[7] it would not be unrealistic to assume that the constant K_1 should be smaller than what is currently used. Wallis[6] recommended a value of between 1.414 and 1.56 for the leading coefficient in the calculation of the terminal rise velocity. With regard to the term $\alpha(1-\alpha)^n$ in (eq. 10) used to account for the influence of other bubbles Wallis has recommended a value of 2 for the coefficient n whereas ASSERT uses a value of 0. This, again increases the magnitude of the gravity term, as $(1-\alpha)^n$ will always be less than 1 for any value of n greater than 0. We, therefore reduced the value of K_1 in the correlation describing the terminal rise velocity of a bubble in an infinite medium from 2 (the recommended value) to 1.4.

3.1 Comparison of ASSERT-4 (Version 1.5) Predictions with Experimental Results

Figures 1a-d to 2a-d show the experimental results for the two cases discussed as well as the computed values with ASSERT being run with the recommended values of K_1 and a as well as our suggested values.

3.1.1 High Void Channel Below Low Void Channel

Figure 1a gives the void fraction variation along the length of the channel. Both the default parameters of K_1 and a and our suggested values are seen to give good results with our values being slightly better. The initial increase in the void fraction before the interconnected region is simply due to expansion of the gas due to a decrese in pressure. The increase in void fraction immediately downstream of the begining of the interconnected region is due to a flattening of the void profile. It is not surprising that ASSERT is not capable of predicting this trend as it is a 3 dimensional effect and ASSERT is a quasi 1-D code.

Figure 1b shows the liquid mass flow rates in the channels. ASSERT with both default values of K_1 and a and our suggested values captures the trend of the mass flow rate; in the lower channel

(HV channel) the flow rate first decreases then increases to assume a higher value than that in the upper channel (LV channel). However, the magnitude of the initial transfer was underpredicted in both cases.

Figure 1c shows the axial pressure variation along the channel. The predicted values are not quite perfect. This is due to an uncertainty in the single friction factor. Teyssedou [8] has found that in single-phase flows the friction factor should be increased by about 5% for two interconnected subchannels as compared to a single channel, for this reason the following single phase friction factor is used:

$$f = 1.05 * f_0$$

where $f_0 = .488Re^{-0.311}$ was the value obtained from our single channel calibration runs.

Figure 1d shows the interchannel pressure difference. It can be seen that the interchannel pressure difference is resonably well predicted, although over-estimated slightly.

3.1.2 High Void Channel Above Low Void Channel

Figure 2a gives the void fraction variation along the lenght of the channels. In this case buoyancy drift and void diffusion act in opposition to each other. ASSERT using default values of K_1 and a significantly underpredicts the void transfer. This is to be expected as the gravitational effects are over-emphasized and the void diffusion effect is under-emphasized.

Figure 2b shows the liquid mass flow rates. It can be seen that our recommended values of K_1 and a lead to a better prediction at the end of the channel whereas the recommended values capture the flow more accurately at the mid-point of the channel. In neither case is the recovery of the liquid by the high void channel captured.

Figure 2c shows the axial pressure variation along the channel. In this case the pressure drop is underpredicted by a significant amount. If one compares the high inlet void below low inlet void cases against the high inlet void above low inlet void cases it is interesting to note that the experimental pressure drops are identical whereas ASSERT predicts different total pressure drops depending on the respective locations of the high and low inlet void channels.

Figure 2d shows the interchannel pressure difference. It is understandable that ASSERT is in poor agreement with the experimental results just after the the beginning of the interconnection as the pressure equalization in the two channels is carried out by a mass transfer (mainly liquid) and ASSERT is unable to predict the initial large liquid transfer just after the beginging of the interconnection. The acceptable agreement between the predicted and experimental interchannel pressure difference near the end of the channel is expected as the total liquid mass flow rate is quite well predicted by this point.

4. CONCLUSIONS

We have seen, in comparing ASSERT-4 (Version 1.5) predictions with experimental data, that if the default parameters are used in the correlations which account for the void diffusion and the gravity driven phase seperation, the void diffusion is under-predicted and the effect of gravity is over-predicted in the mechanisms for lateral void transfer in ASSERT. Suggestions for values of these parameters which seem to improve the predictions have been made.

5. REFERENCES

[1] Tapucu, A., Geckinli, M., Troche, N."Experimental Investigation of Mass Exchanges Between Two Laterally Interconnected Two-Phase Flows" "Part-II: Subchannel Geometry-Horizontal

Flow" Ecole Polytechnique de Montreal, Report IGN-557, (1984)

[2] Tahir, A. and Carver, M.B. "Comparison of ASSERT Subchannel Code with Marviken Bundle Data",AECL-8352, 1984

[3] Judd,R.A., Tahir,A., Carver,M.B., Kiteley,J.C., Rowe,D.S., Stewart,D.G. and ThibeaultP.R.; Two-Phase Flow and Heat Transfer in Rod Bundles. ASSERT-4 User's Manuel. AECL-8573, 1984.

[4] Ohkawa,K. and Jahey Jr.,R.T.; "The Analysis of CCFL Using Drift-Flux Models", Nuclear Engineering and Design,Vol. 61, 1980

[5] S. Gencay: Private Communication

[6] Wallis, G.B., "One-Dimensional Two-Phase Flow" McGraw-Hill, (1969)

[7] Carver, M.B., Tahir, A., Rowe, D.S., Tapucu, A. and Ahmad, S.Y. "Computational Analysis of Two-Phase Flow in Horizontal Bundles", Nucl. Eng. and Design, V82, P12 (1983)

[8] Teyssedou, A.J.; "Thermo-Hydraulic Behavior of Interconnected Subchannels with Blockages" Ph.D. Thesis, University of Montreal, Ecole Polytechnique de Montreal, Sept. 1987

Acknowledgement

The author would like to thank Dr. M.B. Carver and Mr. J.C. Kiteley of the Advanced Reactor Development Division, Thermal Hydraulics Development Branch of Chalk River Nuclear Laboratories for the invaluable help they have given him in the course of this work. I would also like to thank Mr. M. Davidson for producing the graphs for this paper.

ASSERT was made available to Ecole Polytechnique by agreement with the CANDU OWNERS GROUP (COG) Fuel Channel Critical Power Working Party.

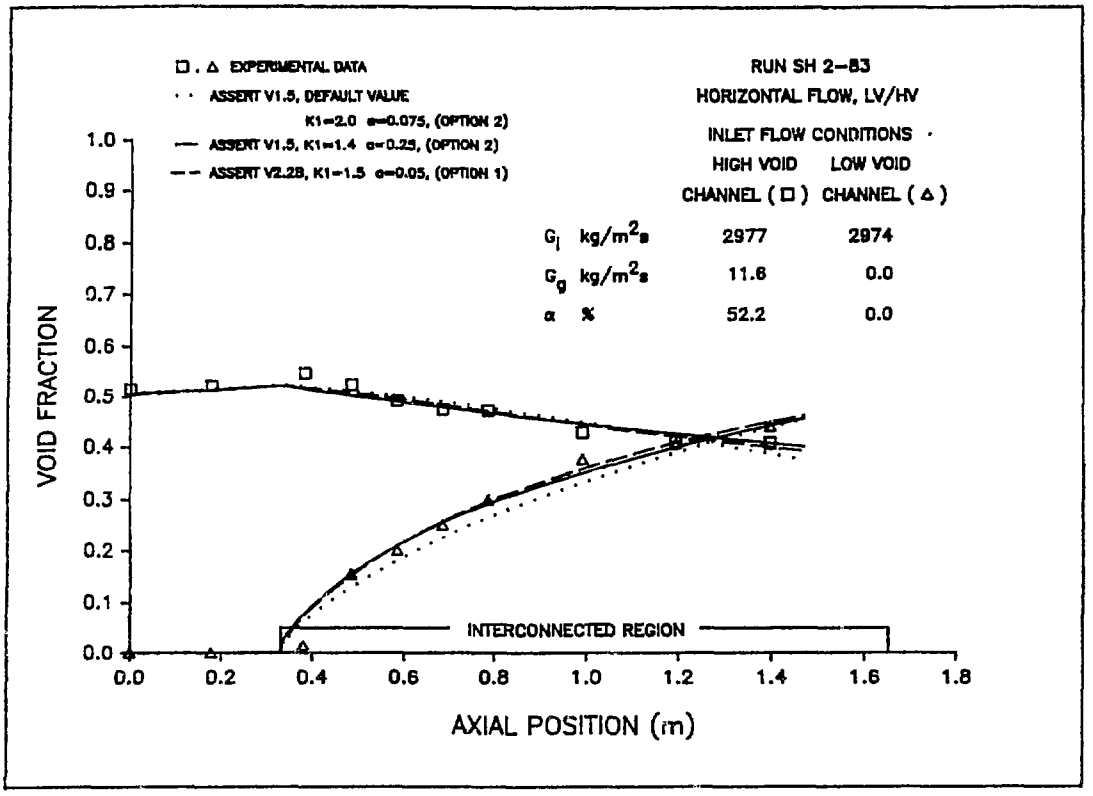

Fig. 1a. Comparison of the ASSERT–4 Predictions With Experimental Data – Void Fractions.

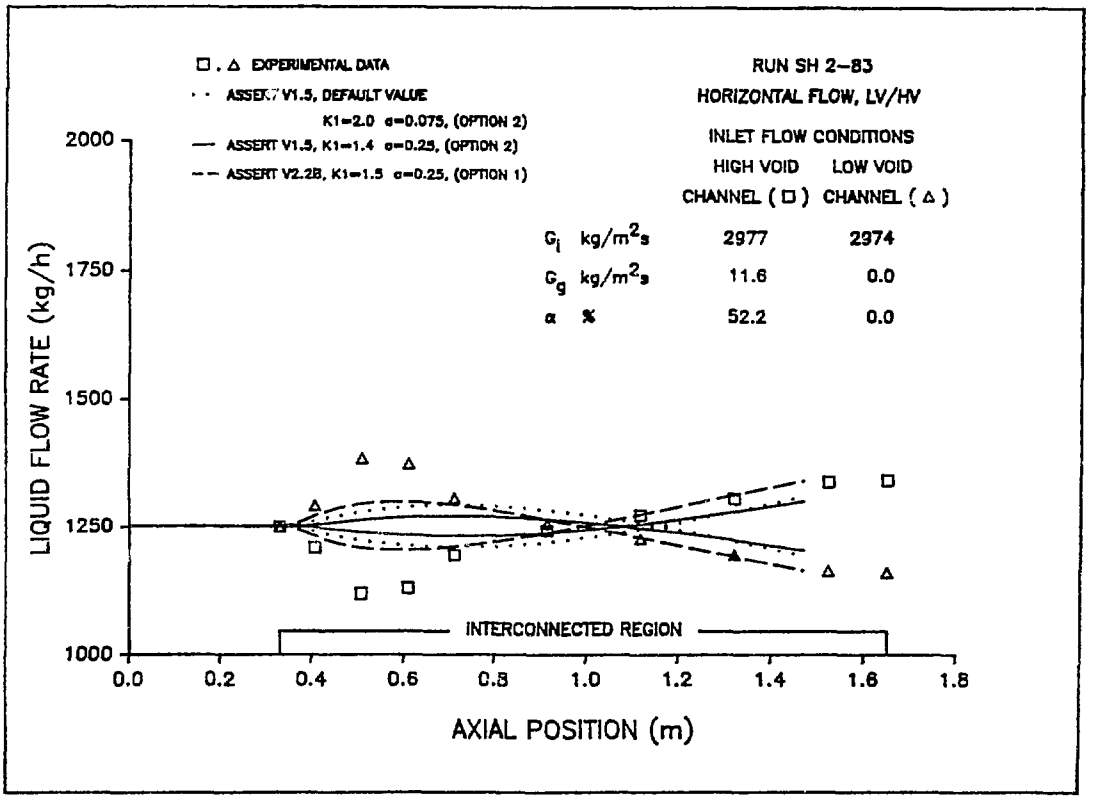

Fig. 1b. Comparison of the ASSERT–4 Predictions With Experimental Data – Liquid Mass Flow Rates.

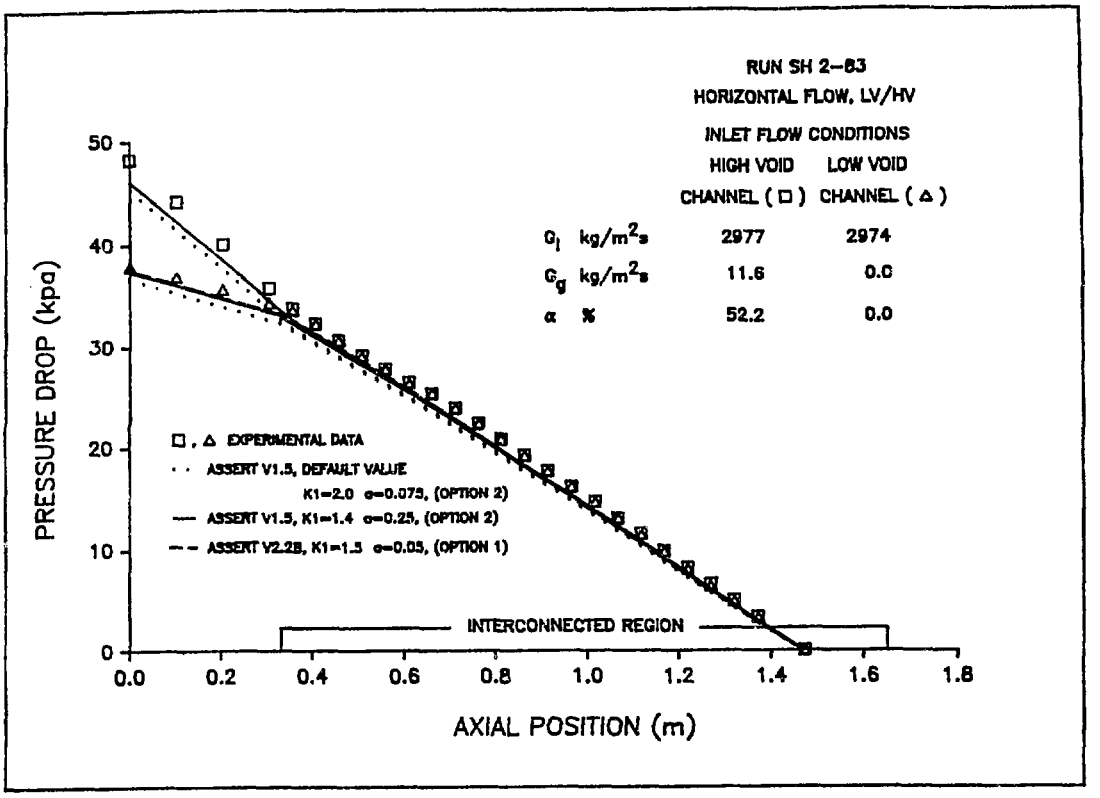

Fig. 1c. Comparison of the ASSERT-4 Predictions With Experimental Data - Axial Pressure Variation.

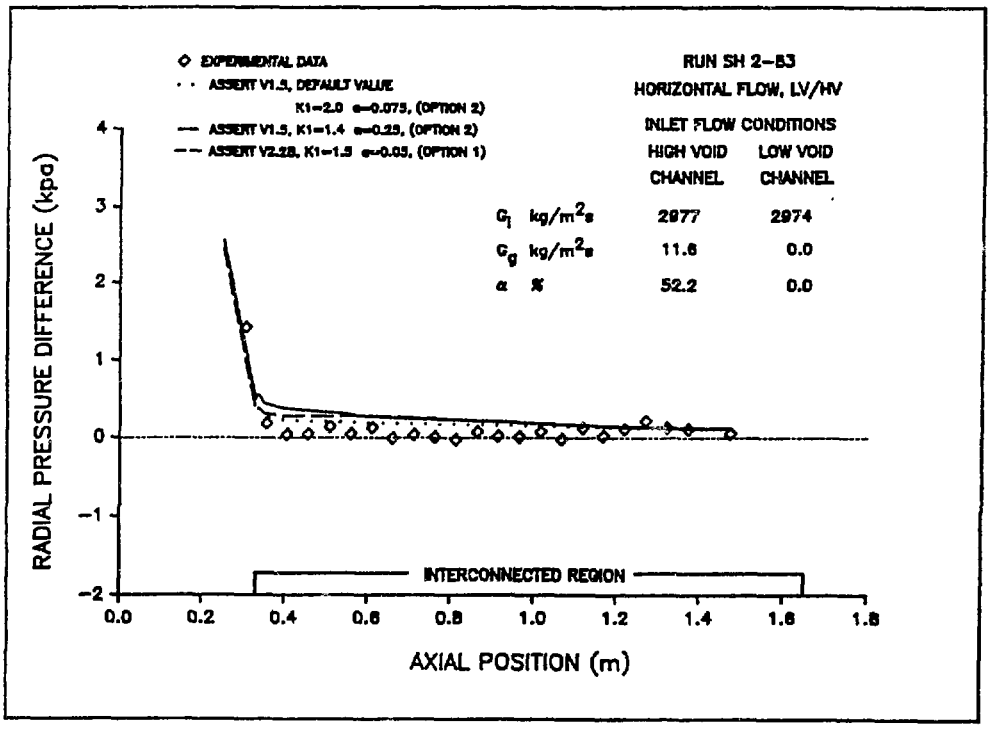

Fig. 1d. Comparison of the ASSERT-4 Predictions With Experimental Data - Interchannel ΔP.

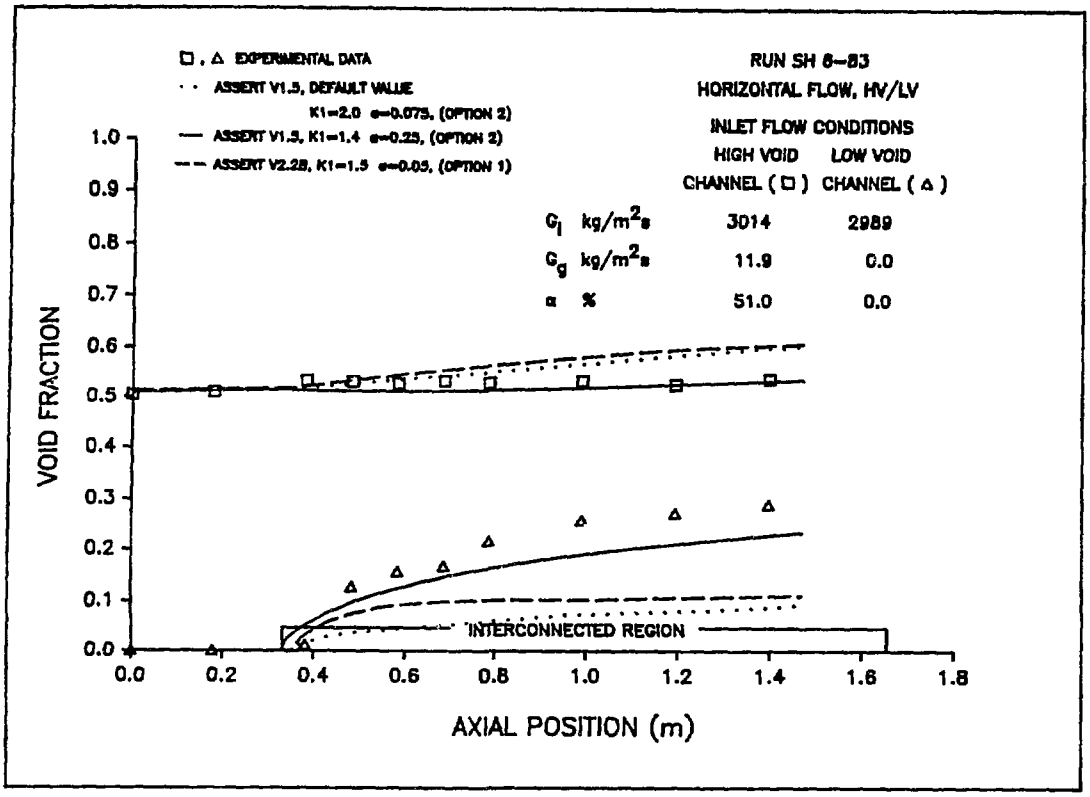

Fig. 2a. Comparison of the ASSERT-4 Predictions With Experimental Data - Void Fractions.

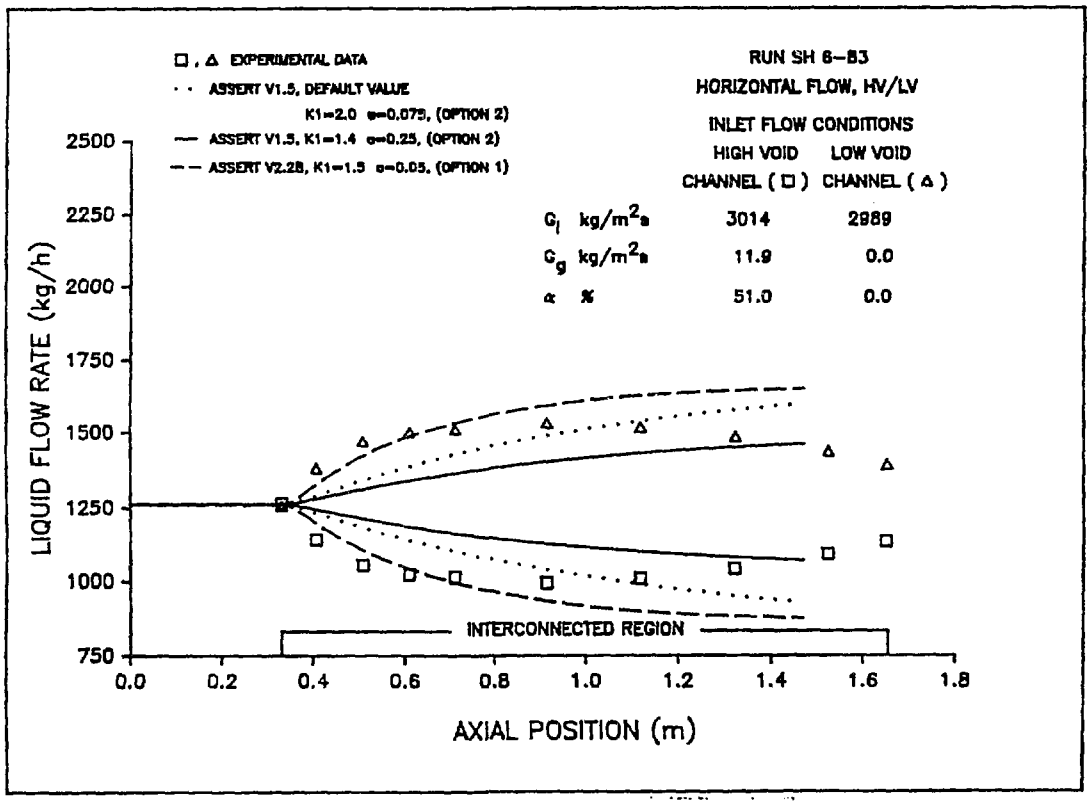

Fig. 2b. Comparison of the ASSERT-4 Predictions With Experimental Data - Liquid Mass Flow Rates.

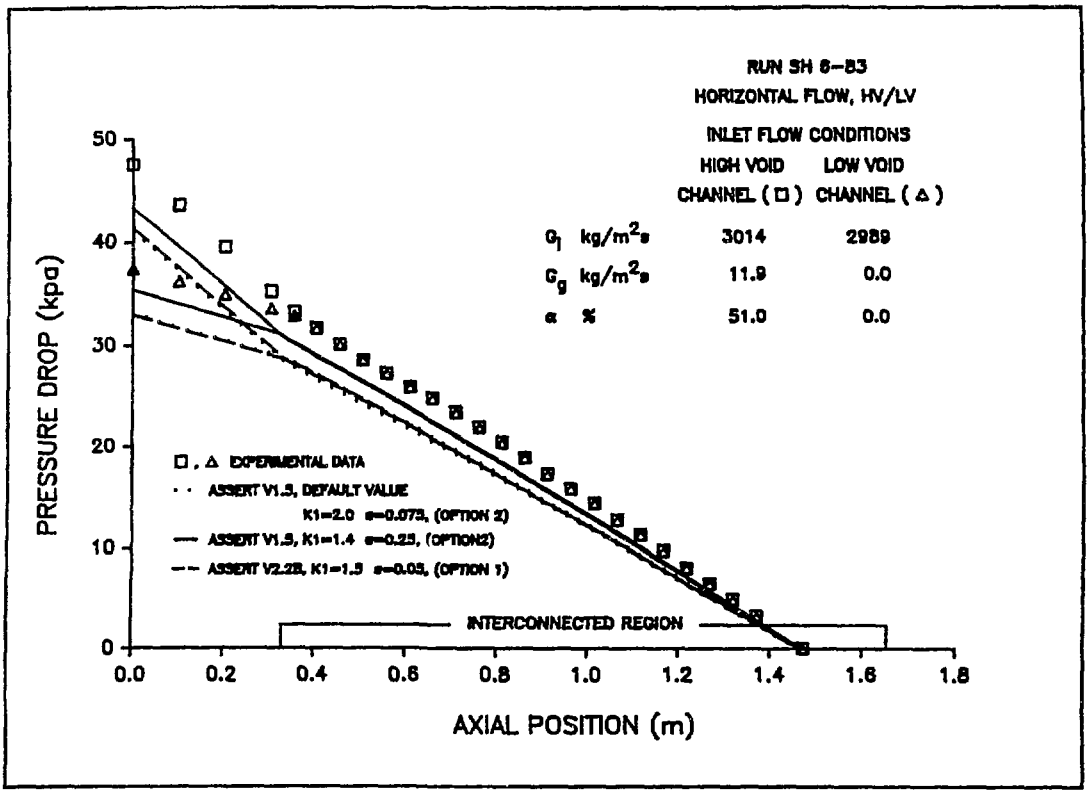

Fig. 2c. Comparison of the ASSERT-4 Predictions With Experimental Data - Axial Pressure Variation.

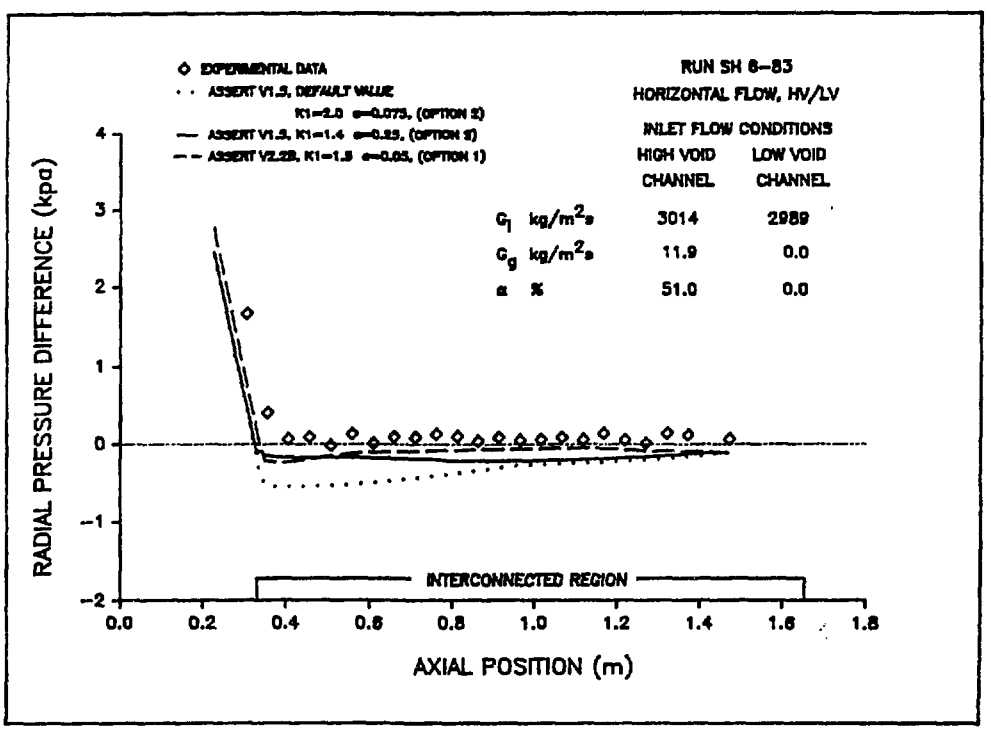

Fig. 2d. Comparison of the ASSERT-4 Predictions With Experimental Data - Interchannel ΔP.

THE EFFECT OF PULSED STEAM FLOW ON REFLUX CONDENSATION PHENOMENA IN A NUCLEAR STEAM GENERATOR

Izundu F. Obinelo
Department of Mechanical Engineering,
McMaster University,
Hamilton, Ontario, Canada.

March 1990

Abstract

Reflux condensation in a long vertical tube is experimentally investigated for both the case in which the inlet mass flow rate is steady and the case in which steady controlled pulsations are applied to the inlet steam flow. The steam flow and heat removal capability of steady inlet steam flow reflux condensation was found to be severely limited by the formation of a plug of single-phase condensate on top of the two-phase condensing region, as a result of flooding at the tube inlet. Subsequently, steady controlled pulsations were applied to the inlet steam flow, using three pulsing frequencies, 0.08Hz, 0.14Hz, and 0.25Hz. It was found that the steam jetting associated with the controlled pulsations distabilises the limiting water column, increasing steam flow and the heat removal rate by several orders of magnitude. Furthermore the experimental results suggest that these enhanced effects are more pronounced as the frequency of pulsation is decreased.

1 Introduction

When steam flows upward at moderate flow rates through a vertical pipe with wall temperature lower then saturation temerature corresponding to the pressure of the steam, part, or all, of the steam, depending on the prevalent flow conditions, will condense, producing a film of condensate flowing downward countercurrent to the steam flow. This phenomena, termed reflux condensation, is of immense importance nuclear power plant primary cooling system under abnormal operation.

Experiments conducted on the semi-scale MOD-2A by Loomis and Soda [2], and on the PKL test facility by Mandl and Weiss [4], indicate that reflux condensation is the prevalent cooling phenomena at low system mass inventories in an abnormal transient following a small-break LOCA (Loss-of-Coolant Accident) in a nuclear power plant primary heat transport system. Results from tests conducted on the PKL test facility by Weishauppl and Brand [4] indicates that following a small break LOCA, reflux condensation is a more effective mode of core cooling than single- and two-phase natural circulation.

More recent investigations carried out on the reflux condensation phenomena has concentrated on the parametric depedence of its heat removal capability.

Loomis and Soda [2], and Weisshauppl and Brand [4] studied the effect of noncondensible gases on the phenomena. Their experimental results showed that the presence of noncondensible gases resulted in higher system presssures, leading to a redistribution of the condensation phenomena and the reduction in the heat removal rate.

Barnejee et al. [7], and Girrard and Chang [8] conducted a detailed investigation of reflux condensation in a single long vertical tube. They postulated that flooding at the tube inlet lead to the formation of a liquid column above the two-phase condensing region, which in turn substantially increases the pressure drop across the tube and limits the amount of steam that could be condensed.

Calia and Griffith [10] studied the flow patterns in a 4-inverted U-tube array and reported successive blockage of the tubes by single phase water columns leading to a cyclic fill-and-dump operation with a high system pressure drop.

Nguyen and Barnejee [12] studied reflux condensation in a single inverted U-tube condenser and reported oscillatory behaviour due to the formation of a liquid column, resulting in a high tube pressure drop.

Chang et al. [11] studied complete reflux condensation in four- and eleven- tube banks and reported cyclic fill-and-dump operation due to liquid-column blockage of the tubes.

Other aspects of these and other studies [7-14] deal with the influence of other system parameters–imposed pressure drop, imposed mass flow rate, wall heat flux, tube diameter and length, multiple tubes, and noncondensible gas concentrations–on heat removal capability under the reflux condensation mode.

In this work, the effect of steam folw pulsations on the reflux condensation phenomena is experimentally investigated. It is expected that pulsing the steam flow will bring such

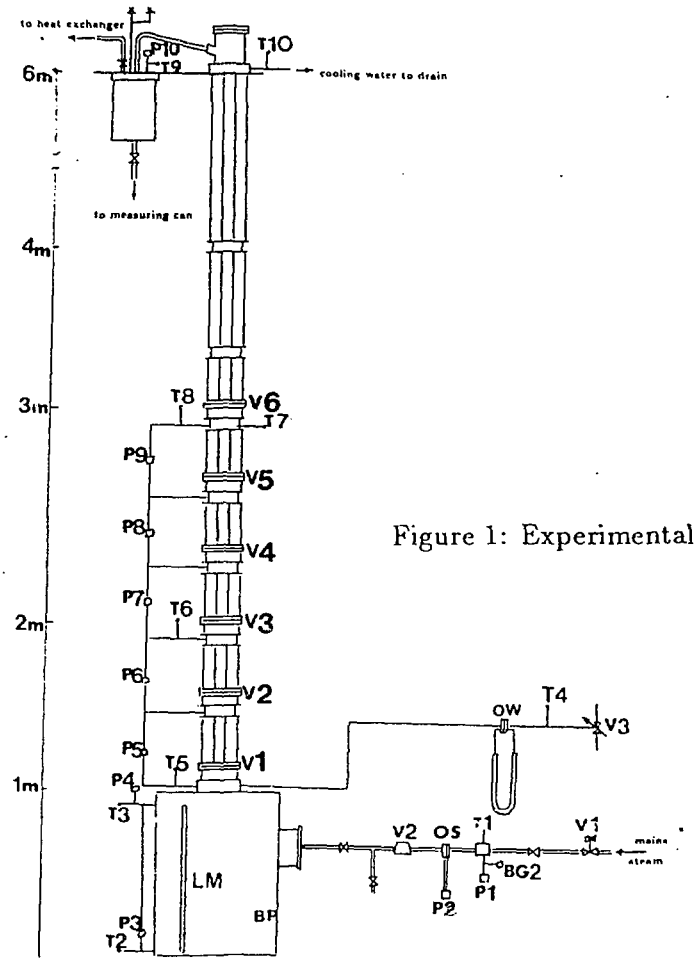

Figure 1: Experimental Set-up

desirable effects as removal of the single-phase liquid region by pushing the flooding limit to higher vapor and condensate flows, and induction of turbulence in the liquid film leading to an augumentation of the heat transfer to the cooling water.

2 EXPERIMENTAL PROCEDURE

The schematic of the experimental set-up is shown in fig.1. High pressure steam from the McMaster Power Plant is admitted via a pneumatic valve (V1), a steam orifice meter (OS), and a pulsing valve (V2), into the bottom plenum of the test section (BP). The pressurised steam from the bottom plenum then rises through the inner Pyrex-glass (od = 2.54 cm) tube of the vertical test column where part or all of it is condesed, and depending on the particular experimental conditions, the condensate and vapor may flow back in countercurrent fashion into the bottom plenum, or flow upwards into the top plenum (TP) which is open to the atmosphere. Any steam leaving the top plenum is condensed in a multi-tube heat exchanger (HT) from where the condensate is collected and measured. Any condensate that is ejected from the test section to the upper plenum is also collected and measured.

Cooling water is admitted via a mixing valve (V3) which is used to adjust its temper-

ature, a cooling water orifice meter (OW) equipped with a U-tube water manometer (M), into the outer jacket of the test section also made of Pyrex glass. The effluxing cooling water from the test section is piped to the drain.

Altogether the sensors in the loop consist of ten T-type thermocouples, ten highly accurate Valdyne linear-response pressure transducers, six void fraction meters, and a number of Bourdon gauges.

The signals from the pressure transducers P2 and P4 are recorded with an APPLE IIe computer installed with an Applescope data acquisition software. A driving program is written in Basic to interface the scope-driver program with the signals coming from the sensors. The Applescope samples at a constant rate of 28 KHz, which is fast enough to adequately record the true signals coming from the sensors in real time. Additionally the signals from P2 and P4 are also recorded wiht digital voltmeters and chart recorder in order to monitor the flow at any time during the experiments.

The signals from all other sensors in the loop are recorded with a 32-channel PHILLIPS data recorder. The levels of the manometer fluid, as well as the condensate level in the bottom plenum, are taken with graduated scales.

At the end of each experimental run any condensate from the heat exchanger connected to the top plenum is weighed in a high-accuracy balance scale.

3 RESULTS

3.1 Flow Regime Observations

3.1.1 Steady inlet steam flow

The phenomena observed in the test section as the steam flow is steadily increased are depicted in figure 2a.

At very low mass flow rates and system pressures a wavy condensate film was observed to flow downward countercurrent to the upward vapour flow. All injected steam was condensed in a very short length of tube. The mass flow rate and system pressure, as well as readings from all sensors are constant, and conditions are truly steady. This mode of operation is referred to as reflux condensation [8], and categorized as the first mode of operation.

As the inlet mass flow rate and the initial bottom plenum pressure are increased, a column of liquid condensate forms above the two-phase condensing region, corresponding to the onset of flooding at the tube inlet [7,8]. The flow regime in the two-phase region is churn-annular countercurrent flow of condensate and vapor. This pulsating column of single-phase liquid serves as a plug on the two-phase region, dramatically increasing the overall system pressure upstream of the plug. Under steady cooling water and inlet steam flows the length of the two-phase condensing region remains constant, while the colum of

Pulsed- and Steady-Inlet-Flow Reflux Condensation

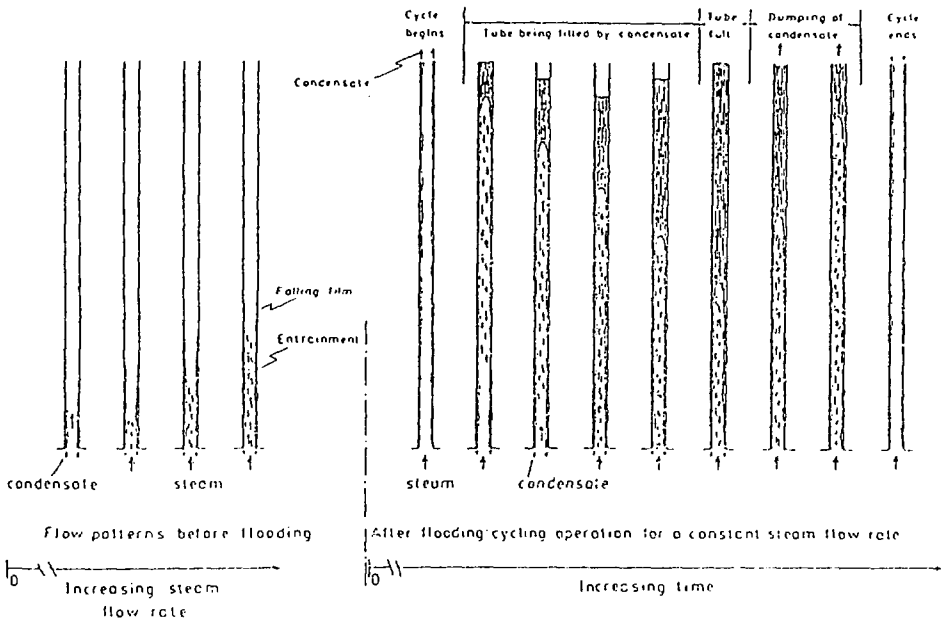

Figure 2: Schematics Flow Regimes observed under Steady Inlet Steam Flow

liquid grows monotonically, leading to a continuous increase in the system pressure drop.

As the system pressure increases to a certain treshold, the column of liquid above the the two-phase region could not be sustained any further, and it is subsequently ejected to the top plenum.

Following this carry-over the system pressure reduces dramatically, while the system undergoes two-phase thermosyphoning for a short while. As the bottom plenum pressure drops to the initial value, this thermosyphoning could not be sustained any further, and the system thus reverts back to reflux condensation, also for a very short while. Subsequently the water column is re-established, and the cycle repeats again. This cyclic mode of operation is referred to as the fill-and-dump mode [8]. It is categorized as the third mode of operation.

At still higher inlet steam mass flow rates the system undergoes two-phase thermosyphoning, with very little, if any reflux to the bottom plenum.

3.1.2 Pulsed Flow

Under a low constant pulsing frequency (0.14 Hz) the phenomena observed in the test section as the average inlet mass flow rate is steadily increased are as follows.

In the low inlet mass flow rate range, corresponding to low-amplitude system pressure pulses (fig.3a), the phenomena observed in the test section was intermittent film condensation of steam (fig.4a), but unlike in the unpulsed inlet mass flow case the maximum condensation length that could be attained without establishing a water column is consid-

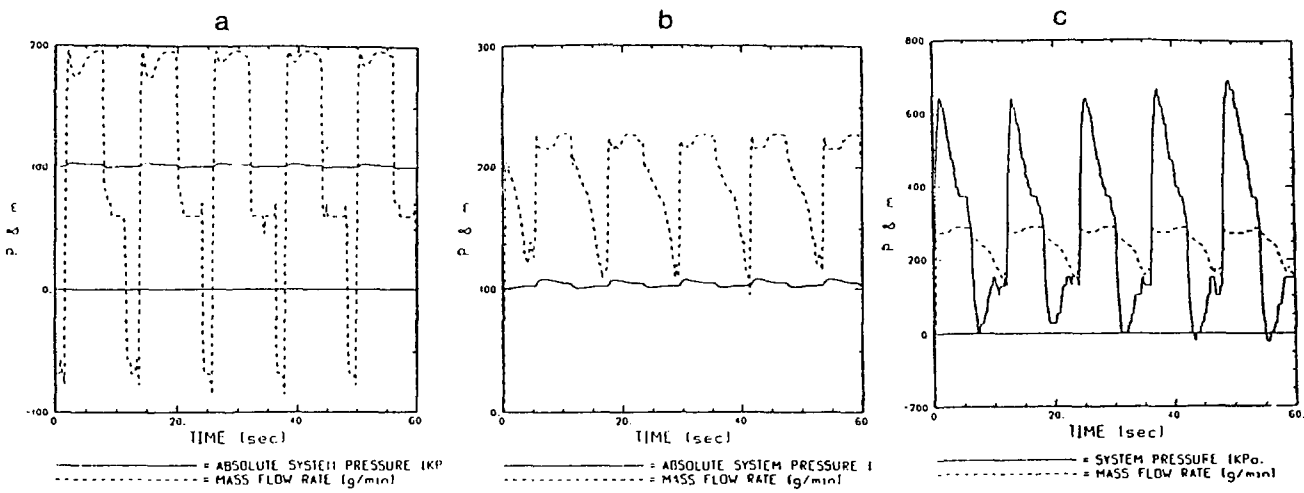

Figure 3: System Pressure and Mass Flow Rate Traces at Different Modes. (a) Reflux, (b) Complete Reflux, (c) Fill-and-Dump

erably higher. This is the first mode of operation, as in the steady flow case.

As the inlet mass flow rate increases, corresponding to relatively higher-amplitude variations in system pressure (fig.3b), a plug of single-phase condensate liquid is established above the refluxing condensate as the system pressure decreases (fig.4b). The length of this single-phase column increases as the pressure decreases, and is maximum at the lowest pressure level. Subsequently as the pressure level increases again this liquid plug is churned and accelerated upwards by the expanding steam jet, and is completely dispersed near the crest of the pressure wave. This mode of operation is categorised as complete reflux condensation, i.e. reflux condensation with water column [7,8].

As the inlet mass flow rate is increased further, corresponding to still higher-amplitude variations in the system pressure (fig.3c), the liquid column is considerably longer (fig.4c) and could not be completely dispersed by the expanding jet of steam. The liquid column thus builds up and is ejected to the upper plenum at periodic intervals. Like in the steady inlet flow case this mode of operation is categorised as fill-and-dump mode of operation.

At relatively higher inlet mass flow rates the system undergoes two-phase thermosyphoning (on the average).

At a lower frequency of pulsation (0.08 Hz), the four modes of operation described above are still observed, but the water column was ejected to the upper plenum in each pulse cycle during the fill-and-dump mode of operation.

At a higher pulsation frequency (0.25 Hz), the system undergoes transition directly from the first mode of operation to the third mode without undergoing complete reflux

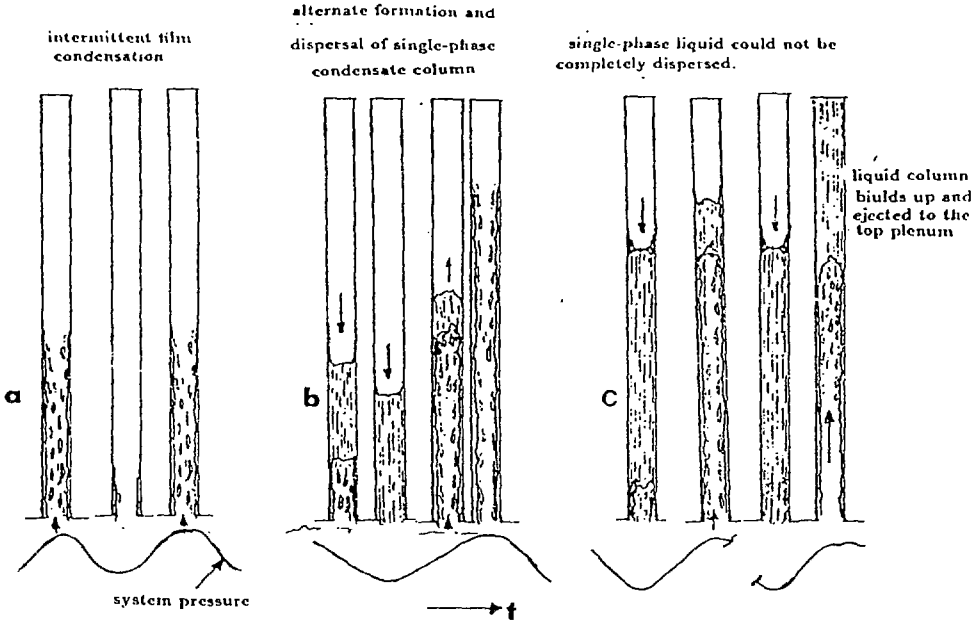

Figure 4: Schematics of the Flow Regimes observed under Pulsed Inlet Steam Flow. (a) Reflux, (b) Complete Reflux, (c) Fill-and-Dump

with water column , like in the unpulsed flow operation.

3.2 Experimental Results and Discussion

3.2.1 System Pressure and Inlet Steam Mass Flow Rate

The time averaged system pressure as a function of time-averaged inlet steam mass flow rate is shown in fig.(5). This characteristic curve is similar to the results obtained by Chang et al. [11] and Calia and Griffith [10] for both single and multiple tube arrangements.

The region A-B fig.(5b) correspond to the first mode of operation in which complete condensation of steam occurs without the formation of water column. Because there is no back pressure due to the absence of water column the overall system pressure is low and there is a linear variation of system pressure with inlet mass flow. The influence of the frequency of pulsation is also evident; while the system barely operates in this linear range for steady inlet steam flow, fig.(5a) shows that the system can operate in this range range up to relatively much higher inlet mass flow rates and furthermore, the maximum mass flow rates that could be attained in this range increases as the frequency of pulsations decreases, while the average system pressure decreases.

For the steady inlet-flow case the region B-C is the long-duration cyclic fill-and-dump mode of operation as witnessed by the sharp rise in the system pressure due to the formation of a water column above the two-phase condensing region. While the 0.25 Hz pulsed

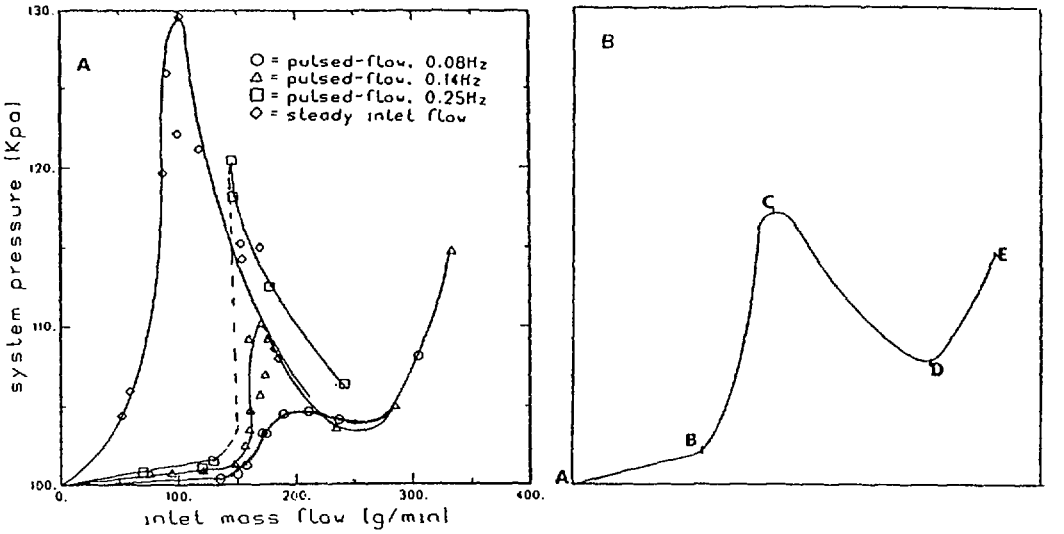

Figure 5: System Pressure vs. Average Inlet Mass Flow Rate. (a) Experiment, (b) Typical

flow experiment did not operate in region B-C at all, for the lower frequency 0.08 Hz and 0.14 Hz pulsed flow experiments this region is the second mode of operation (complete reflux condensation) where the water column is alternately formed and dispersed by the expanding steam.

For the steady inlet flow experiment the region C-D is also the cyclic fill- and-dump mode but with a shorter cycle duration, i.e. more frequent ejection of the water column to the upper plenum. This is also the case for pulsed flow experiments where the water column that could not be completely dispersed builds up and is ejected to the upper plenum, but at much shorter intervals than for steady inlet flow. Additionally the carry-over interval decreases with the frequency of pulsation and for the 0.08 Hz pulses carry-over occurs at each pulse cycle. This in turn results in a nearly constant system pressure in this region of oepration, as shown in Fig.(5a).

In the region D-E the system undergoes friction-dominated two-phase thermosyphoning for all experiment types, with co-current churn-annular flow of condensate and vapor to the upper plenum and little if any reflux to the bottom plenum. The average system pressure in this region is higher for pulsed flows than for steady flows because of formation of a small plug of liquid during the decreasing part of each pressure pulse.

3.2.2 Condensation Rate

The time-average condensation rates obtained for the various experiments are plotted against the time-averaged inlet mass flow rate in fig.(6a) and against the time-averaged

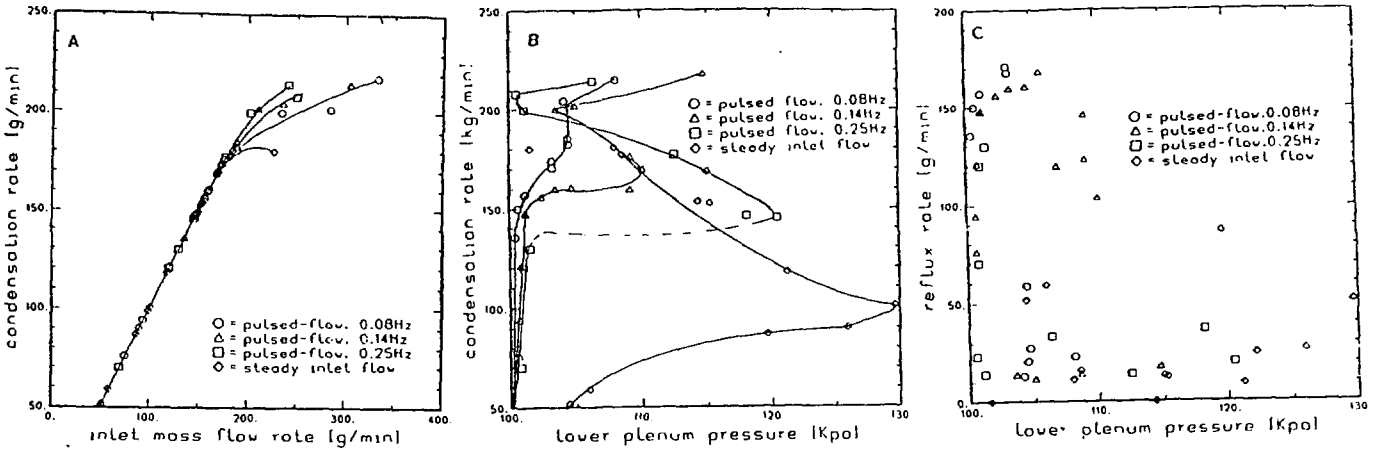

Figure 6: Time-Averaged Condensation Rates

system pressure drop in fig.(6b)

While all admitted steam is condensed in the reflux condensation mode for all cases, as fig.(6a) shows, the steady inlet flow reflux condensation tends to saturation at a lower steam flow rate than do the pulsed flow experiments due to the formation of a stable water column.

The plot of condensation rate vs. pressure drop in fig.(6b) closely follows the system pressure vs. inlet mass flow rate characteristics in fig.(5), since all admitted steam was condensed in the first three modes. As may also be seen from fig.(6b), the formation of a stable and growing water column in the steady inlet flow experiments leads to a much higher pressure drop across the tube for the same mass of steam condensed.

In a real loss-of-coolant-accident situation, the refluxing of condensate back to core is of primary importance to overall heat removal capability of the steam generator under the reflux condensation mode. The time-average condensate reflux rate to the bottom plenum are plotted as a function of the time-averaged system pressure in fig.(6c). It is evident from this plot that there is a remarkable improvement in the reflux rate achieved by pulsing the steam flow. Furthermore, the reflux rate is seen to increase as the frequency of pulsation increases.

3.2.3 Condensation Length, Steam Jetting and Heat Removal Rate.

The time-averaged heat removal rate obtained in the various experiments is plotted against the system pressure in fig.(7a). Again the remarkable improvement obtained by pulsation

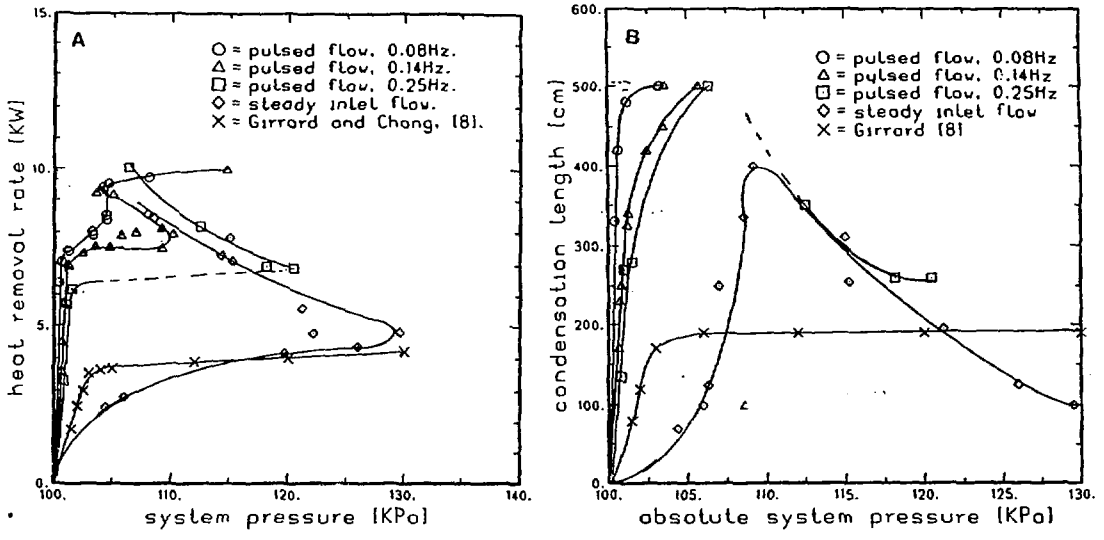

Figure 7: Time-Averaged Heat Removal Rate and Condensing Region Length

is evident. Furthermore, the heat removal rate is seen to increase as the pulsation frequecy decreases.

The formation of the single-phase water column above the condensing region limits the amount of tube surface area that is available for heat exchange between the condensing vapor and the cooling water flowing in the secondary side, since this liquid column is usually subcooled. The pronounced improvement in the improved heat removal capability of the system in pulsed flow experiments stems in part from the the larger surface area of the tubes that is made availabe for condensation when the steam flow is pulsed. This effect is illustrated in fig.(7b), where the average condensation length is plotted against the time-averaged sytem pressure. It is seen that pulsing the steam flow increases the condensing region length remarkably.

Local measurements taken in the various experiments indicate that the the upper parts of the condensate liquid column is subcooled and at a lower temperature than the cooling water temperature (which also indicate that there is an opposite heat flow from the the secondary side to the primary side at some point past the two-phase condensing region). A substantial part of the improvement on the heat removal capability by pulsation arise from direct contact heat transfer associated with the mixing of the steam and this liquid column as the later is churned and accelerated upwards by the expanding steam wavefront. This churning and mixing effect become more pronounced as the frequency of pulsation is decreased, as a result of the higher pressure amplitudes associated with lower frequency pulsations.

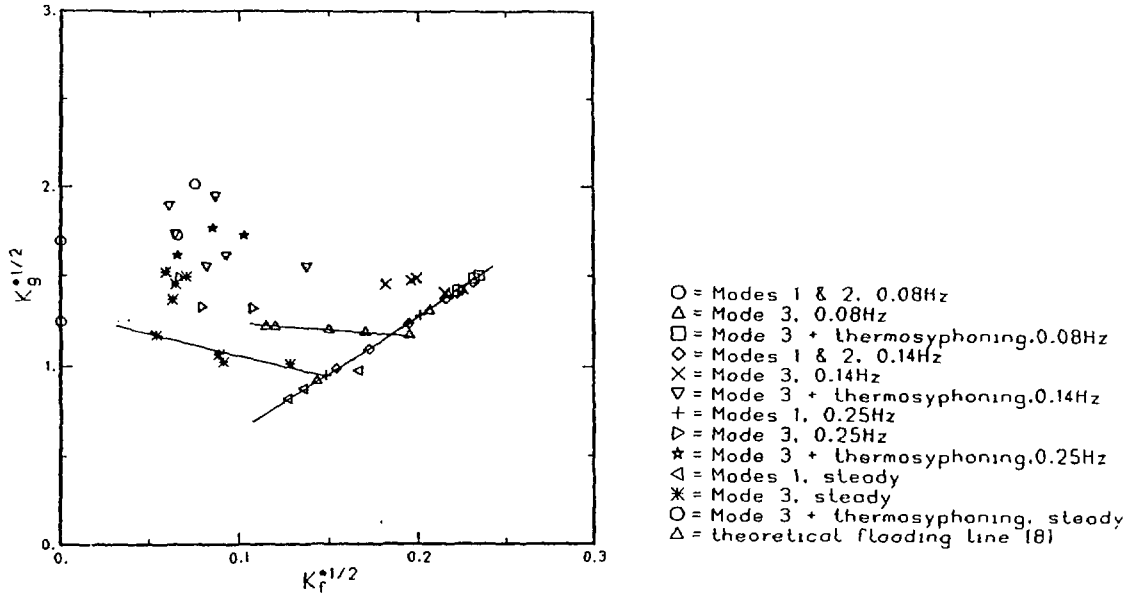

Figure 8: Dimensionless steam and Condensate Reflux Rates

4 Theoretical Considerations

It has been established [2,7-14] that the formation of a limiting single-phase water column in steady inlet flow reflux condensation is governed by flooding at the tube inlet. Fig.(8) shows a plot of the dimensionless steam and condensate reflux rates defined in terms of the Kutatiladze variables K_f and K_g, given by

$$K_i = \frac{\rho_i \cdot j_i}{\sqrt[4]{g.\sigma.(\rho_l - \rho_g)}}$$

While the role flooding in the steady inlet flow case is apparent, the scatter of pulsed-flow data suggests that the limiting process of pulsed-flow reflux condensation, i.e the formation of a quasi-stable liquid column (beginning of the third mode of operation) does not have a simple dependence on flooding at the tube inlet. Preliminary theoretical considerations as well as experimental results suggest a strong dependence on the frequency and amplitude of pulsation. Especially the penetration and condensation effects on the upward acceleration of the liquid column by the expanding steam jet, which undoubtedly governs the point at which the single-phase liquid column could not be completely dispersed any more, is being investigated.

Present results seem to suggest that heat removal enhancement increase as the frequency of pulsations is reduced. However the problems associated with pulsation of steam large-amplitude shock waves upstream of the pulsing device, and (audible) condensation

shock waves as the steam jet interacts with the subcooled liquid column, among others– seem to become more pronounced at lower frequencies– and higher amplitudes– of pulsation. These problems may become especially significant in the presence of noncondensible gases in the system, which is known increase the system pressure.

At present a theoretical model for pulsed steam flow reflux condensation is being formulated, bearing these factors in mind. It is hoped that results from these experimental and theoretical investigations will reveal an optimum combination of frequecy and amplitude of pulsation for which the thermalhydraulics of the whole system is optimized. Later still, the influence of noncondensible gases on the system will be experimentally investigated.

5 CONCLUSION

Experimental investigations have been conducted to study reflux condensation under conditions in which the inlet steam flow is pulsed. The results obtained from this investigation suggest the following conclusions:

- The dispersion of the liquid column above the condensing steam reduces the back pressure exerted by the former on the system. The resulting benefits are two fold: much higher steam flow rates could be utilised, and much lower pressure drops in the system.

- The sharp pressure pulses associated with the steam pulsations lead to rapid upward expansion of the steam in the tube, pushing any liquid column with it, and thereby making more surface area of the tube available for condensation.

- The churning and mixing of the steam and the subcooled single-phase condensate column as the later is accelerated upwards constitute direct contact heat transfer and lead to condensation of a substancial part of the admitted steam. In this regard the formation of a liquid during each pulse cycle becomes beneficial, as evidenced by the high increases in the heat transfer rate in the second and third modes of operation.

- The instabilities associated with steam pulsations induce higher turbulence in the liquid film, leading to the augmentation of film coefficients on the tube walls and greater heat transfer to the cooling water.

- The extent to which these enhancements can be achieved in a multiple tube arrangement should only be one of scale, since earlier investigations [10,11] have shown that the same characteristic phenomena occurs in the reflux condensation of steam in single as well as multiple tubes.

Acknowledgements

I wish to express my gratitude to all my colleagues who have contributed to make the publication of this paper a success. Especially I thank my two supervisors– Dr. G.F. Round (Mechanical Engineering Dept.) and Dr. J-S Chang (Engineering Physics Dept.) of Mcmaster University– without whose express support and advice the report would not have been possible. This work is supported by the Natural Sciences and Engineering Research of Canada.

References

[1] Burchill, W.E., Nuclear Safety, Vol. 23, No.5, 1982, pp. 525-536.

[2] Loomis, G.G., an Soda, K., NUREG/CR-2335, 1982.

[3] Mandl, R.M., and Weiss, P.A., Nuclear Safety, Vol. 23, No. 2, 1982, pp. 146-154.

[4] Weisshaupl, H. and Brand, B., ANS Specialists Meeting on Small Break Loss of Coolant Accident Analyses in LWRs Conference, Aug. 1981, Monterey California.

[5] Kiang, R.L., Jeuck, P.R., and Sursock, J-P., The Second International Topical Meeting on Nuclear Reactor Thermal-Hydraulic, Santa Barbara, California, USA, January 11-14, 1983, pp. 833-839.

[6] Adams, J.P., McCreery, G.E., Berta, V.T., The Second International Topical Meeting on Nuclear Reactor Thermal-Hydraulic, Santa Barbara, California, USA, January 11-14, 1983, pp. 825-832.

[7] Banerjee, S., Chang, J-S., Girard R., and Krishnan, V.S., Journal of Heat Transfer, Vol. 105, 1983, pp. 719-727.

[8] Girard, R.,and Chang, J-S, Advancement in Heeat Exchanger Technology, G.F. Hewitt ed., Hemishpere Pub. Co., 1982.

[9] Tien, T.L., Fukano, T., Hijikata, K., and Chen, S.J., EPRI Report No. NP-2648, November 1982.

REFERENCES

[10] Calia, D., and Griffith, P., HTD Vol. 15, ASME, New York, 1981.

[11] Chang, J-S., Donevsi, B., and Revenkar, S.T., Fundamental Aspects of Gas-liquid Flows, E.E. Michaelides Eds., ASME Press, FED-vol 29, 1985, pp. 91-96.

[12] Nguyen, Q.T., Banerjee, S., ANS Transactions, Vol. 43, 1982, pp. 788-789.

[13] G.F. Round, J. Pipelines, 1 (1981) 307-318.

[14] G.F. Round and E. El-Sayed, J. Pipelines, 5 (1985) 95-106.

[15] G.F. Round and E. El-Sayed, J. Pipelines, 6 (1987) 105-116.

The Manufacture and Analysis of a Reference Defect for High Frequency Ultrasonic Inspections of CANDU Pressure Tubes

Michael A. Graf
Department of Mechanical Engineering
University of Toronto

Introduction

Nature of the Problem:

Conventional ultrasonic inspection techniques have long been used to monitor the condition of CANDU reactor pressure tubes both during their manufacture and their service lifetimes. Defects which are typically encountered during these inspections include cracks, scratches, fret marks, or inclusions of foreign material in the tube wall. An effective inspection technique should therefore be able to (a) detect the presence of such defects and (b) give some indication as to the relative size or severity of the defects. Most of the current established inspection systems rely on monitoring the amplitude of ultrasonic signals reflected from a defect which may be present in the tube wall. The detection of any such signal indicates the presence of a defect of some sort. The amplitude of the reflected signal can then provide some information as to the size or nature of the defect. Larger defects will tend to give larger amplitude reflections while small defects yield only small reflections. In addition, cracks and void-like defects will give larger reflections than inclusions of metallurgically similar materials. An obvious limitation of this technique lies in the consideration of defects which are too small or inclusions which are too similar to provide any detectable reflection at all for the given incident ultrasonic waves. This limitation has recently become a significant one in that the standard 10 MHz inspection system has failed to detect inclusion-type defects in various reactor pressure tubes. Because these defects were only later discovered through the use of high frequency (100 MHz) techniques, the implementation of these higher frequency systems into standard practice is being considered.

In order for a new inspection technique to be implemented with some confidence, it is desirable for there to exist a calibration scheme by which the effectiveness and accuracy of the technique can be demonstrated and verified. A suitable calibration process could simply consist of a reference defect of known properties to which the inspection technique is then applied. It is the preparation of just such a reference defect with which this work is concerned. In that the development of

this new technique has been in response to an identified weakness (ie. the inability to detect small inclusions), it is reasonable to require a reference defect with clearly defined properties which resemble those expected during in-service inspections. To this end, a process has been postulated which may be able to manufacture defects of the required type. The ability of this process to meet the necessary requirements must therefore be evaluated.

Reference Defect Requirements:

The inclusions which were missed by the standard, low frequency inspection system lay in a geometric plane roughly parallel to the axial-circumferential plane of the tube. The dimensions and composition of the inclusions were such that the defects were essentially transparent to ultrasonic waves of frequencies on the order of 10 MHz. Therefore, a suitable reference defect should lie in the same geometric plane and either be made of a material with an acoustic impedance similar to that of its host or be small enough to escape low frequency detection. The host tube material should be the same Zr-2.5Nb which is found in ordinary pressure tubes so that all of the reference properties pertaining to ultrasonic wave propagation will be identical to what will be encountered during in-service inspections.

Reference Defect Manufacturing Process:

The process which was used to manufacture a reference defect involved the insertion of small metallic inclusions along the radial centre-line of the tube wall. To accomplish this, two equal length sections of tube were cut and machined so that the inner diameter of one was equal to the outer diameter of the other. Sample defects in the form of thin shims and wires could then be placed onto the outer surface of the smaller tube before the larger tube was fitted around it. In this way, the defects were effectively placed in an axial-circumferential plane within the fabricated tube wall. While the fit between the two tube sleeves was tight, it was not sufficient for any ultrasonic techniques to be used as there still existed air gaps between the sleeves which would prevent the transmission of wave energy from one sleeve to the other. It was therefore necessary to metallurgically bond the sleeves together to remove whatever gaps were present. The easiest way to accomplish this bonding was to Hot Isostatically Press (HIP) the tube assembly for a given period of time. Following electron beam welding of the ends of the sleeves to evacuate the gaps, the high temperature and pressure of the HIP'ing process would allow diffusion across the gaps between the sleeves to take place. This diffusion was

expected to remove all traces of the gaps entirely and provide some interdiffusion between the defect materials and the host material as well. A potential drawback of the process, however, lay in the fact that some permanent metallurgical changes in the host zirconium may occur as a result of the high temperatures involved. These changes may, in fact, be significant enough to compromise one of the central requirements of the reference defects (ie. that they be present in a host material which is ultrasonically similar to that of an ordinary pressure tube). Part of the analysis of the reference tube, therefore, must be a consideration of the metallurgical effects of the HIP'ing process as is relevant to the propagation of ultrasonic waves.

The single reference tube which was manufactured was HIP'ed at a temperature of 900°C and a pressure of 25000 psi for 4 hours. The defects which had been inserted included brass and steel shims of thickness .001", tungsten wires of diameters .001" and .002", and a platinum wire of diameter .0005". The suitability of these defect materials and geometries as well as that of the HIP'ing parameters was evaluated with respect to the defined reference tube requirements.

Analysis

Diffusion during HIP'ing:

The HIP'ing parameters which were selected for the manufacture of the reference tube were expected to allow some diffusion across the gap between the two tube sleeves to take place. A quantitative estimate of the amount of diffusion expected will give an indication of the suitability of the chosen parameters as well as a means of predicting more suitable parameters for future applications. The simple one-dimensional diffusion equation, along with the appropriate diffusion coefficients, was used to provide this quantitative estimate. It was discovered that significantly more diffusion was predicted than was actually found to occur. This, most likely, was a result of the fact that the initial gap between the sleeves provided some resistance for the diffusion process which the mathematical model did not account for. The actual geometries of some of the defects can be seen in the optical micrographs shown in Figures 1(a)-(d). It can be noticed that some trace of the original interface is still visible. Subsequent ultrasonic analysis, however, revealed that this trace provided no detectable reflection. Therefore, the tube sleeves were considered adequately bonded by the prescribed HIP'ing parameters.

Ultrasonic Wave Behavior:

Comparison of the attenuation of ultrasonic waves propagating through the HIP'ed tube material with that experienced in ordinary zirconium revealed that no significant differences existed. In this sense, therefore, the HIP'ed zirconium was considered to be metallurgically similar enough to its original conditions to establish the processing parameters as satisfactory.

With respect to the defects, classical wave theory is able to predict the frequency dependent reflection coefficient from a thin layer or from a thin cylindrical defect. Comparisons of this theory with actual measured results was carried using the ultrasonic hardware and digital signal processing software available. In measurements where large acoustic impedance differences were involved, measurements compared well with theory. Measurements carried out on the reference tube, however, demonstrated less conclusive results due to the more closely matched impedances which tended to reduce the signal to noise ratio, and to the non-ideal geometries of the defects which introduced effects not accounted for in the theory. Despite the limitations of the hardware and software with respect to the resolution of exact defect structure, however, it was nonetheless apparent that each of the proposed reference defects was clearly detectable even at frequencies as low as 10 MHz. The primary requirement of the reference defects, therefore, had not been fulfilled. Further analysis indicates that defect sizes up to one order of magnitude smaller should be used and that cylindrical defects tend to be preferable to layered geometries from the point of view of their transparency to lower frequency signals.

References:

L.M. Brekhovskikh, *Waves in Layered Media*, (Academic Press, 1980).

P.M. Morse, *Theoretical Acoustics*, (McGraw-Hill, 1968).

D.L. Douglass, *The Metallurgy of Zirconium*, (International Atomic Energy Agency, 1971).

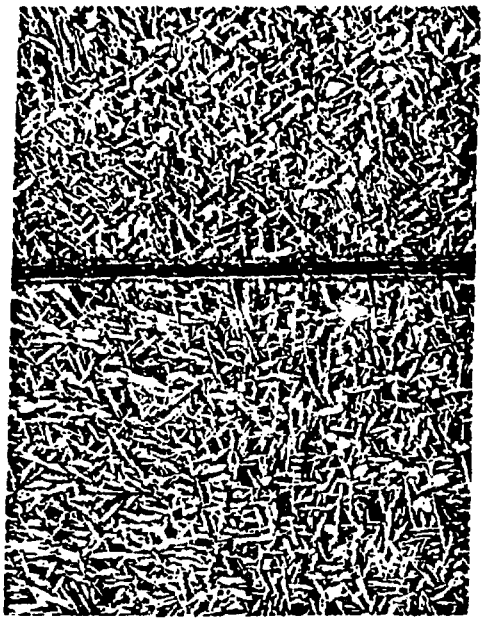

Figure 1(a)
.001" steel shim (200X)

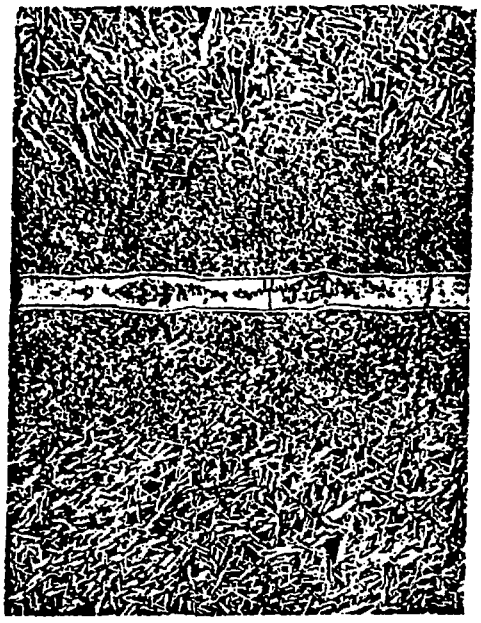

Figure 1(b)
.001" brass shim (200X)

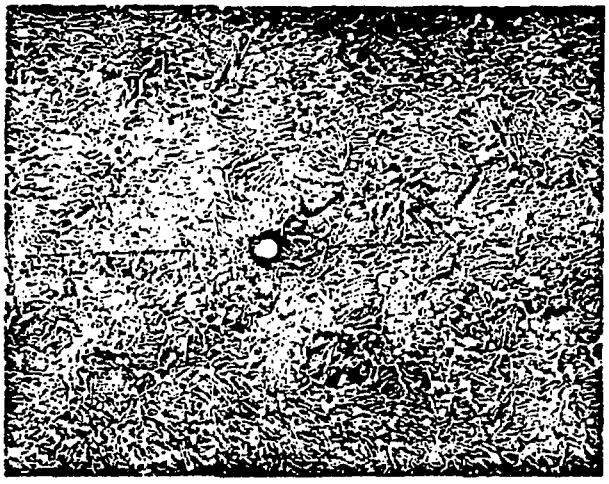

Figure 1(c)
.001" tungsten wire (200X)

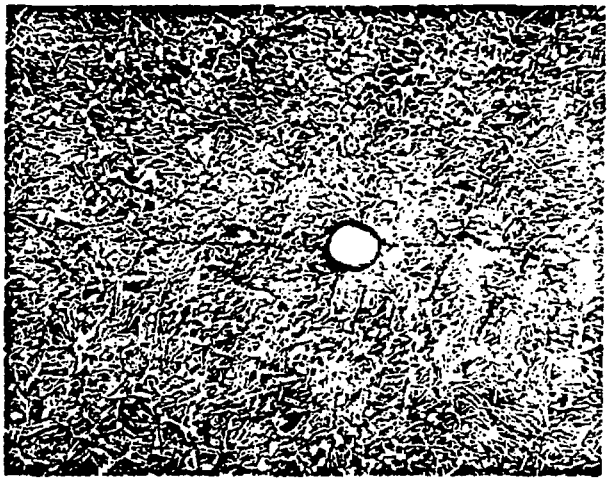

Figure 1(d)
.002" tungsten wire (200X)

Plasma Interaction with the

Refractory Materials

C.B. Kwok M.S. Mathur and J.S.C. McKee

Accelerator Centre
Department of Physics
University of Manitoba
Winnipeg (MB) R3T 2N2 Canada.

ABSTRACT

TiC wafers of high purity, and TiC coatings deposited by plasma spraying process were used to investigate the possibility of the formation of carbon-hydrogen and titanium-hydrogen complexes on the surface.

Introduction

H-H nuclear fusion required a compatible condition of the interior of the sun. Such seemingly formidable condition can be reduced greatly in D-T fusion (for example, D-T fusion in a plasma required a temperature in the order of $(10 - 20)\times10^7$ K). The D-T plasma can be confined by torroidal and poloidal fields, and energy confinement time is in the order of 1 sec., which for such a high temperature is a long time. Since there is no such thing as a perfect confinement, plasma particles unavoidably diffuse out of the plasma and impinge on the container wall and other components. Therefore, in the design of fusion reactors, the choice of material for the first wall, limiters and other components is rather critical. Energetic plasma ions can interact with these materials forming complexes, which, as impurities, degrade the plasma and lower its temperature. The surface of the exposed components will, of course, be altered in the process. As a result, materials chosen for the fusion reactor containment vessels and components should have: 1. high melting point, 2. resistance to thermal fatigue, physical and chemical sputterings. These desired characteristic make TiC or TiC coating desirable for first wall application. This study investigates molecular formations on pure TiC wafers (99.95 % purity) and TiC coatings (by plasma spraying (PS) procedure (1)). In this paper we are interested in the formation and absorption of carbon hydrogen and titanium hydrogen complexes formed during H ion bombardment of the TiC (wafer and PS). In a similar experiment involving D_2^+ implantation of C (graphite), Mathur et. al. were successful in observing the formation and absorption of various deuterated methanes on the surface (2). These observation involved the use of the unenhanced surface Raman facility at the University of Kentucky. Conventional techniques involving low energy electron beam (Auger, LEED etc.) cause desorption of these complexes and prove somewhat ineffective (the formed complexes are often lost before the measurements commence). One other technique, the TFMS (Time of Flight Mass Spectrometry), is currently under investigation.

Experimental Details

Samples

The TiC wafers of 0.0254 m diameter, and 0.003 m thickness are acquired from the Atomergic Chemical Corporation of New york. Thes wafers have 99.95% purity, and in order to

avoid contamination the wafers are kept under vacuum until the time of experiment. The TiC coatings of 300 to 400 μm thickness were prepared at the Institute de Genie des Materiaux (Bou Cheville, Canada) by plasma spraying onto Inconel 624 substrate (3). These coating samples were placed on the internal wall of the Tokamak fusion reactor and were subjected to repeated hydrogen plasma discharges. The samples were left inside the reactors for three month or $\approx$ 1500 discharges and were sealed in positive hydrogen pressure environment upon removal from the reacctor. H_2^+ ions of 60 keV were generated using the Narodny Linear Accelerator at the Universty of Manitoba Accelerator centre and bombarded the surface of the TiC wafers. The wafers were mounted in a specially designed sample holder, and the sample was surrounded by a LN_2 cold trap to keep pump oil vapours away from the sample surface. A beam of energetic H_2^+ passes through a deflection plate assembly, whereby the beam is deflected across the surface of the target thus scanning the surface under computer control. Beam diameter and beam current were measured and the wafer were exposed to the beam for a known time to achieve uniform implantation and desired fluence of particles, using

$$ions/cm^2 = 1.6 \times 10^{-19}\ (I/A)T.$$

Where I is current in Ampere, A area in cm^2 and T time in seconds. During the entire experiment, a vacuum of 10^{-7} Torr was maintained in the system and after implantation, the TiC wafer was transferred immediatelly to a holder where it was kept under positive H_2^+ pressure. The sample was removed from this hydrogen environment prior to surface analysis.

Analysis

The Kratos surface analysis system at the University of Kentucky was used to perform XPS (X-ray photoelectron spectroscopy) and characterization of the surface of TiC (PS) and TiC wafers also employed the use of surface Raman facility at the same university.

Results and Discussion

The XPS data from the surface of the TiC(PS) coating from the Tokamak reactor is given in Figures 1 and 2. The kinetic energy (eV) vs. intensity (counts/sec) data of Figure 1 reveals a titanium $^2P_{3/2}$ line at 794 (eV). Theoretically this line should be much stronger and should have a value of 799 (eV). Because of chemical and charge shifts the 799 line however

is shifted down to 794. The 798 line is probably an Auger line or an artifact associated with XPS (shake-up-line). The binding energ (eV) vs. intensity (counts/sce.) data of Figure 2 has a strong line at 458 (eV). This is the 455 line shifted up in terms of binding energy due to chemical and charge shifts. The 457 line probably associated with XPS (shake up line). This data confirms the presence of free Ti on the surface of the TiC(PS) coatings which have been subjected to plasma ion bombardment. The argument as to whether this is due to carbon deficicency in the coating (for coatings are somewhat porus and are carbon deficient, $(C/Ti = 0.74 - 0.84)$ depending on spraying conditions and this fact can play a role in the hydride formation and blistering), or to the dissociation of TiC molecules subjected to ions from the plasma still need to be resolved. If there were free Ti atoms available to the impinging hydrogen ions, titanium hydride could be formed. Since the implanted coating is showing the presence of free Ti atoms, the likelihood of TiC molecule dissociation when subjected to H ions is very real. The dissociated carbon atoms can combine with hydrogen to form carbon hydrogen complexes and some titanium hydrogen complex formation is also expected. For this to be verified, the coating surface was analysed by the surface Raman scattering technique the observations are and compared with those of H_2^+ implanted TiC wafer. The Inelastic light scattering data of TiC wafers is shown in Figure 3, and Figure 4 shows the data for TiC (PS) for comparison. The Raman scattered signal of Figure 3 is accumulated over a period of 6 hours from the TiC wafer bombarded with 60 keV H_2^+ to a fluence of 10^{17} $ions/cm^2$. A doublet with component Raman bands at 3270 and 3372 cm^{-1} is observed in the Raman spectrum. Gaseous methane (CH_4) has been studied (4,5) extensively and the Raman spectrum is known to contain two active fundementals at 2914.2 and 3022.0 cm^{-1} respectively. Dension (6) also calculated the first order frequencies from the observed fundamentals. He obtained for CH_4 (in cm^{-1}) $w_1 = 3029.8$ *and* $w_3 = 3156.9$ respectively. The Raman bands observed by us have slightly higher shifts than the Raman bands of pure CH_4 gas. It is likely that in our situation some impedence is offered to the CH_4 moleccules in their vibration, and this in turn can result in dampening of the vibrational frequencies.

For the TiC(PS) shown in Figure 4. Raman active bands at 783, 1642, 2330, 2640.8, 2752, 2818, 2863, 3199.8, 3310.8 and 3399.6 cm^{-1} have been observed. Molecules containing C-H bond have normal frequencies of about 3300 and 700 cm^{-1}, for example in

C_2H_2 molecules these fundamentals have been reported at 3377 cm^{-1} (Raman) and 729 cm^{-1} (infrared) respectively (7). The 3399.6 cm^{-1} Raman band in our observation can thus be attributed to the C-H stretching vibration of C_2H_2 molecule. The 3199.8 and 3310.8 cm^{-1} band are the ccorresponding bands in Raman spectrum of the wafer. This comparation indicates that the bombardment of the TiC coated surface with energetic H ions from the fusion plasma results in the decomposition of TiC molecules into Ti and C atoms. The free carbon combines with available impinging hdrogen ions and results in the formation of methane and acetylene (CH_4 and C_2H_2). The formed gas get abosrbed on the TiC surfacce. The C=C and C-C stretching vibrations for the hydrogen and carbon complexes occcur at = 1600 and 2300 cm^{-1} respectively (8). The weak 1643 and 2330 cm^{-1} Raman band in our study can be attributed to such vibrations. The presence of these bands in the observed Raman spectrum of the implanted TiC(PS) coating surface suggests the formation and absorption of carbon and hdrogen complexes. The Ti from the decomposed TiC molecule must be present on the surface of TiC(PS) coating and its presence is confirmed b the XPS data as discussed earlier. However, some of the free Ti atoms on the surface can combine with impinging hydrogen ions to form hydrides.

The 783 cm^{-1} broad Raman band can be understood in terms of titanium hydrogen stretching (9). The broad and weak 2641 cm^{-1} band in our observation can be interpreted in similar fashion in terms of linear Ti-H stretcching (9,10). The 2752, 2818 and the 2863 cm^{-1} bands in our observation can be attributed to the various CH stretchings of the C_2H_6 molecule, which for pure C_2H_6 gas appear at 2744, 2778, 2839.5 and 2963 cm^{-1}.

Conclusion

The Raman data as obtained from the H_2^+ bombarded surface of a TiC wafer have been successfully utilized to conform CH activity and methane formation and adsorption on TiC (PS) surface. On the other hand, the titanium hydride formation for energies other than the 60 keV of the H_2^+ used is not detected. The effect of the energy vs. fluence of the hydrogen ions on the formation of carbon-hydrogen and titanium-hydrogen complexes is currently under investigation. The presence of carbon-hydrogen and titanium-hydrogen complexes on the surface of irradiated TiC(PS) coatings suggests the formation and absorption of various complexes of carbon-hydrogen and titanium-hydrogen. The out-diffusion of these

complexes may be the reason for the amorphicity as observed by Fournier et al (11). They suggest that the amorphization starts when induced diffusion makes H concentrate around small grain boundaries and initiates the ionization process. We are suggesting that the concentration of hydrogen ions (from the plasma), in and their build up on the surface, together with induced diffusion can result in the formation of molecular complexes which can then be absorbed on the TiC surface. The out diffusion of these complexes can poison the plasma as well as create low mobility vacancies and interstitials. This could result in inertial amorphization of the TiC surface.

References

1. C. Brunet, S. Dallaire and R.G. Saint-Jacques, J. Vac. Sci. Technol. A3, 2503 (1985).
2. M.S. Mathur, V.P. Derenchuk and J.S.C. McKee v62 N3 (1984).
3. Y. Gomay, K. Kawahata, N. Noda, and S. Tanahashi, J. Nucl. Mater. 111/112, 323 (1982).
4. R.G. Dickenson, R.T. Dillon and F. Rasetti, Phys. Rev. 34 (1929) 582.
5. G.E. MacWood and H.C. Uuey, J. Chem. Phys. 4 (1936) 402.
6. D.M. Dennison, Rev. Mod. Phys. 12 (1940) 175.
7. G. Glockfer and C.E. Morrell, J. Chem. Phys. 4, 15 (1936).
8. G. Herzberg, Infrared and Raman Spectra, D. Van Nostrand Co. (1968).
9. H. Kaesz and Saillant, Chem. Rev. 72, 231 (1972).
10. W. Ho, N.J. DiNardo and E.W. Plummer, J.Vac. Sci. Technol. 17, 134 (1980).
11. D. Fournier, M.O. Ruault and R.G. Saint-Jacques,
Nucl. Inst. and Methods in Phys. Research B19/20, 559 (1987).

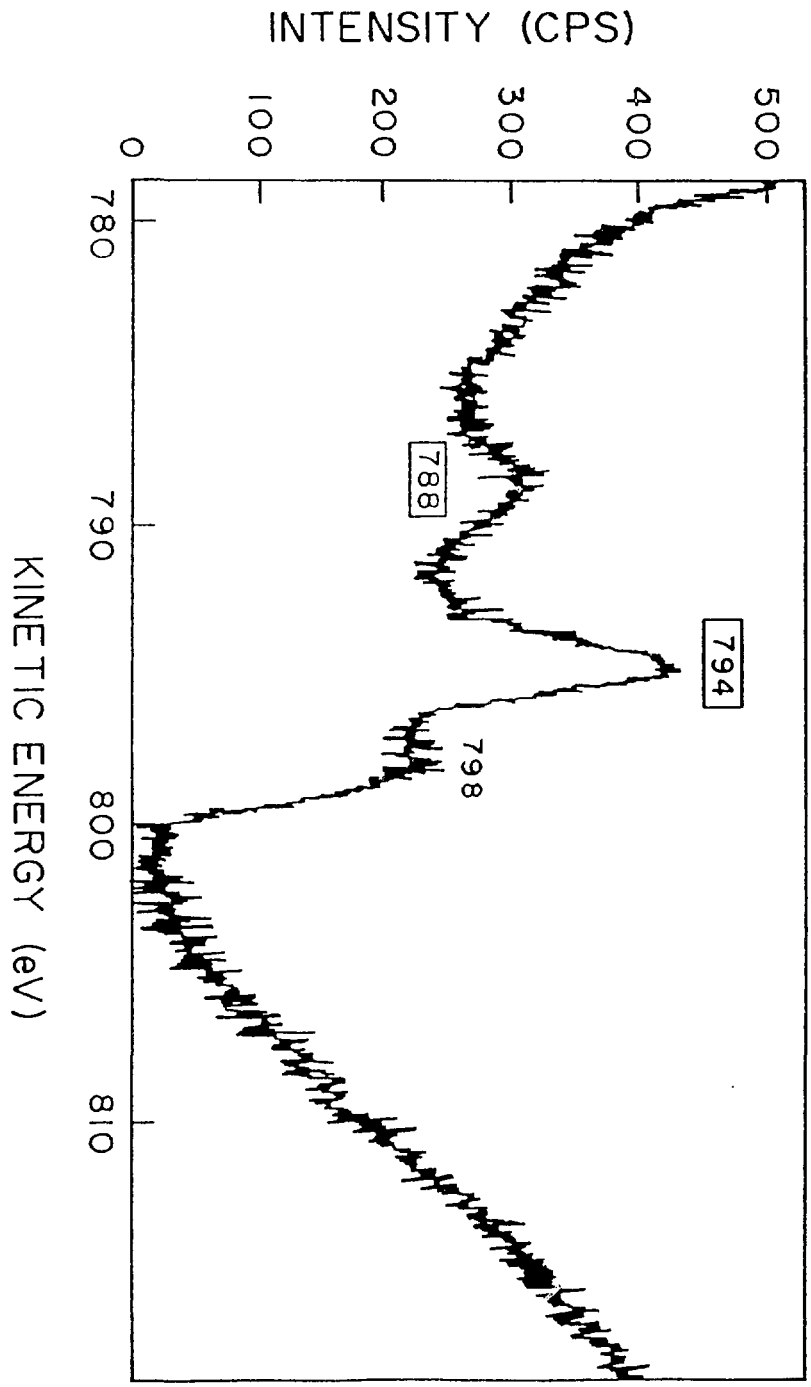
INTENSITY (CPS)
0
100
200
300
400
500
780
790
800
810
KINETIC ENERGY (eV)
788
794
798

Fig. 1

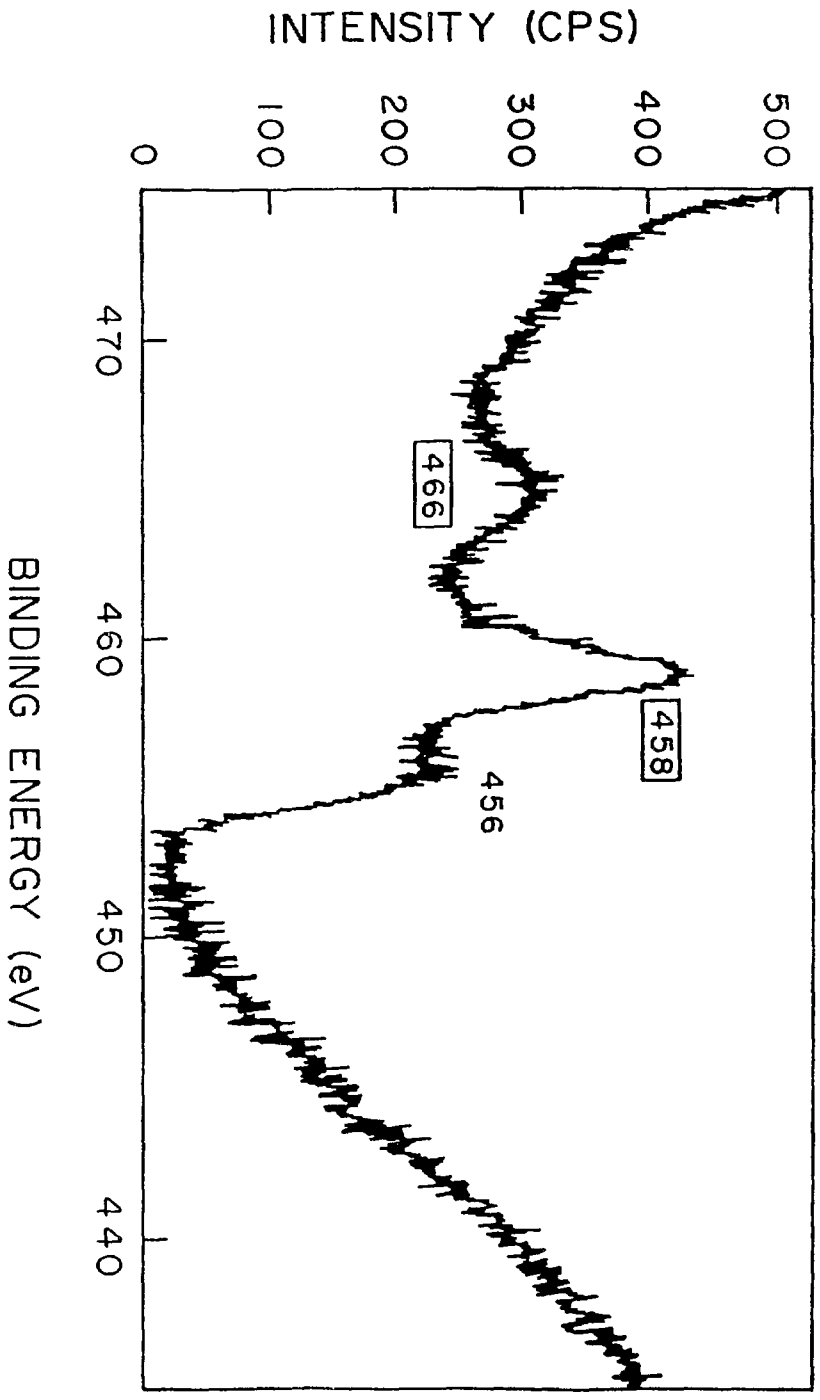
INTENSITY (CPS)
0
100
200
300
400
500
470
460
450
440
BINDING ENERGY (eV)
466
458
456

Fig. 2

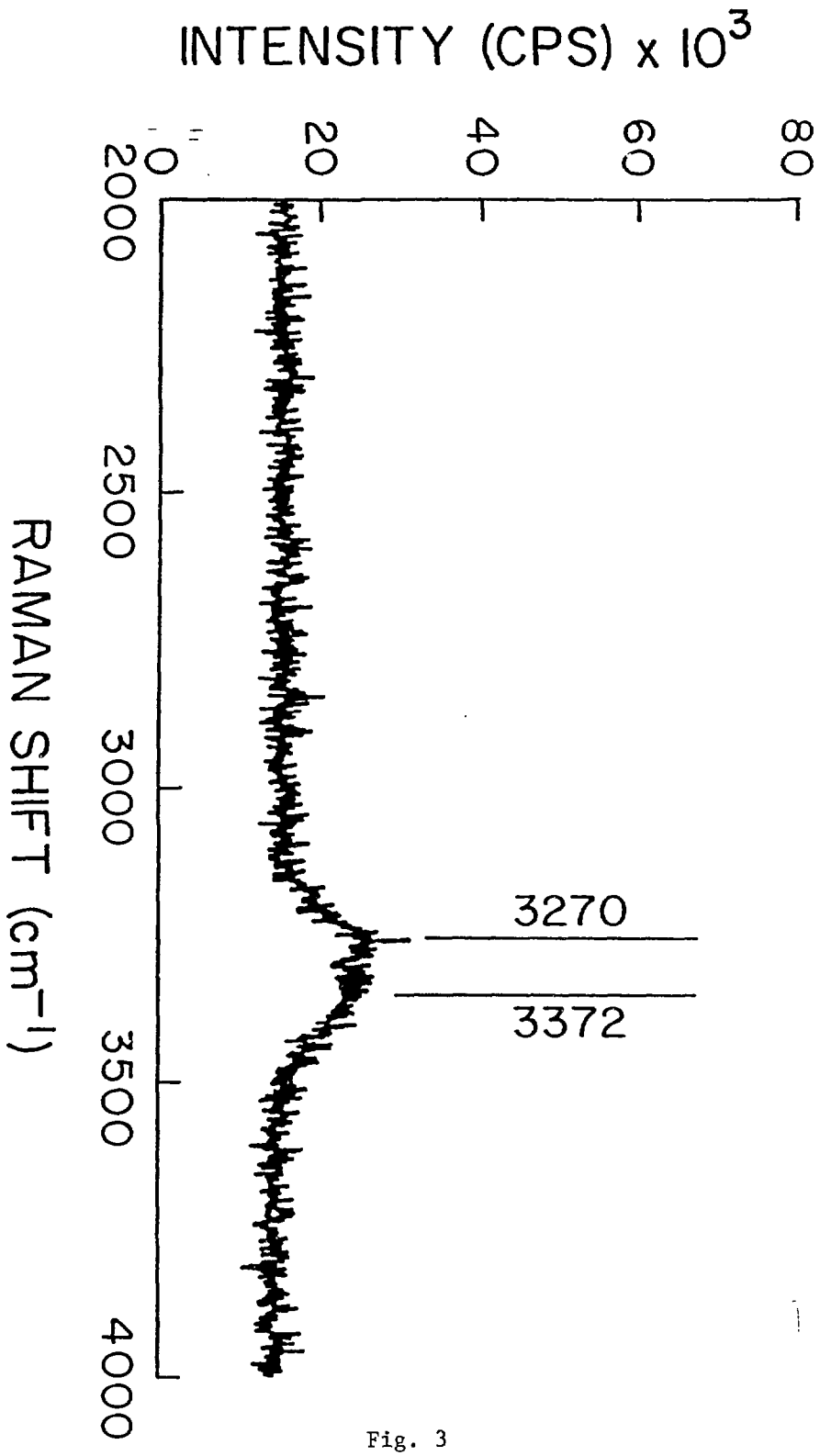
INTENSITY (CPS) x 10^3
0
20
40
60
80
2000
2500
3000
3500
4000
RAMAN SHIFT (cm⁻¹)
3270
3372

Fig. 3

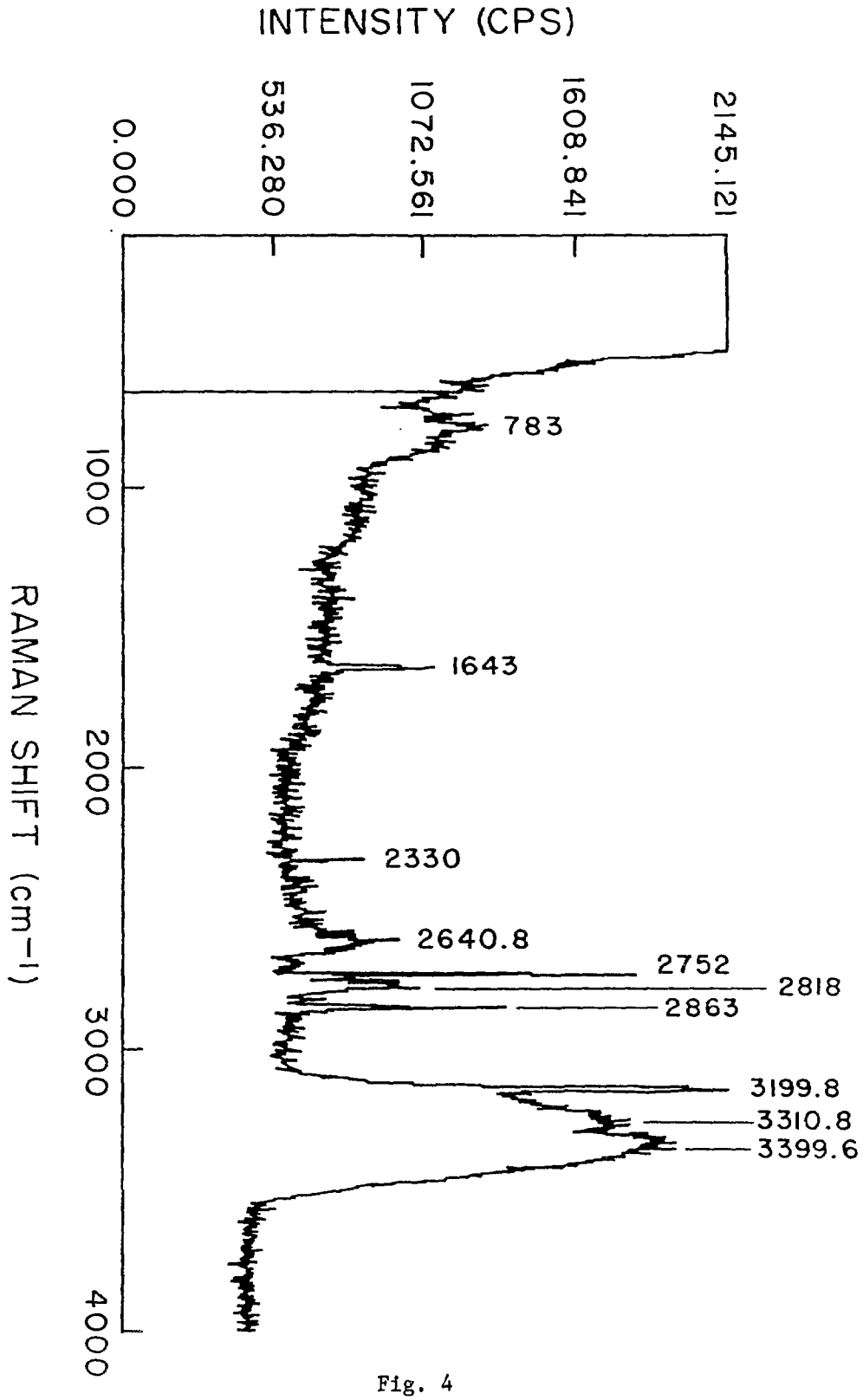
INTENSITY (CPS)
0.000
536.280
1072.561
1608.841
2145.121
RAMAN SHIFT (cm⁻¹)
1000
2000
3000
4000
783
1643
2330
2640.8
2752
2818
2863
3199.8
3310.8
3399.6

Fig. 4

FIGURE CAPTIONS

Figure 1

XPS spectra of TiC(PS) coating subjected to $\approx$ 1500 plasma discharges inside the Tokamak fusion reactor. Intensity (CPS) vs. Kinetic Energy (ev)

Figure 2

XPS spectra of TiC(PS) coating subjected to $\approx$ 1500 plasma discharges inside the Tokamak fusion reactor. Intensity (CPS) vs. Binding Energy (ev)

Figure 3

Raman spectrum of the 60 KeV H_2^+ bombarded surface of TiC. Laser power 500 mw. Entrance slit-80 μ. Exit slit-80 μ. Total data acquisition time – 6 hours. (multiple scans with 2 s/step.)

Figure 4

Raman spectra of the TiC(PS) coating surface subjected to $\approx$ 1500 plasma discharges inside the Tokamak fusion reactor. Raman shift (cm^{-1}) vs. Intensity (CPS)

Trace Analysis of Emissions from Hospital Incinerators

Matthew M. C. Ko

Department of Chemical Engineering and Applied Chemistry
University of Toronto
Toronto, Ontario
M5S 1A4

Introduction

Particularly in industrialized countries, the proliferation of solid wastes and decisions about how to dispose of them are increasingly of concern. While many solid wastes are deposited in dry landfill basins, some are incinerated as a means of mass and volume reductions so that only ash residue needs to be disposed. However, waste incinerators emit fumes and particles which may cause air pollution problems (1,2).

The present project is to assess the impact of hospital incinerators and other mixed industrial emissions in urban airsheds by radioanalytical and receptor modelling techniques. It has been estimated that about 85 % of a hospital's waste is general refuse while the remaining 15 % is contaminated with infectious agents (1). A previous study on a Toronto hospital incinerator has revealed that its potential emissions contained considerable amounts of toxic elements including As, Ba, Sb, Cd and Se (3). The elevated levels of these toxic metals are partly attributable to the inorganic metal oxide pigments contained in hospital-used plastics. Since hospital waste can contain 20 % by weight (approximatey four times the amount found in municipal soild waste)(1), the toxic metal contents of the waste and ultimately the emissions are expected to be significantly more than other types of incinerators.

Air particulate concentrration data obtained by aerosol sampling near hospital incinerators together with statistical techniques can result in accurate source apportionment, hence an evaluation of the incinerator's impact to the atmospheric environment.

Experimental Aspects

(i) Aerosol and Incinerator Ash sampling

Thirty three aerosol samples were collected at an elevated receptor site close to the Toronto Western Hospital incinerator stack between August to November 1989. The downwind distance from the stack (about 300 ft) was estimated to be short enough to avoid too much dilution of the emittants by dispersion but long enough to allow the emitted hot gases to form aerosols by condensation. The relative locations of the hospital incinerators and sampling site are shown in Fig. 1. A dichotomous sampler, which consisted of a General Motor Hi-Vol sampler and two of the six-stage Sierra impactors, was used along with Whatman 41 filters to collect a fine particulate deposit (aerodynamic diameter of particles < 2μm) and a coarse particulate deposit (2 μm < diameter < 10 μm). Since the site was close to the source, it was believed that adequate size-sorting of aerosols could be achieved by such Hi-vol and 2-stage sampling arrangement.

Whatman 41 cellulose filters were chosen because of their low trace elemental 'blank' content, ease of handling and suitability for use in INAA. Air flow rate of 0.3 m^3/min was monitored automatically by a sensor. At the end of the twelve hours sampling periods, the exposed filters were transported back to the laboratory, inside polyethylene bags, for instrumental analysis.

Incinerator flyash samples were collected at the Toronto Western Hospital incinerator, they were air dried, homogenized before being bottled for subsequent analysis.

(ii) Analysis of Aerosol and Ash Samples

Instrumental neutron activation analysis (INAA) is considered to be an ideal analytical technique for air particulate study because of its instrumental, multielemental, sensitive and non-destructive nature. INAA was carried out at SLOWPOKE-2 nuclear reactor at the University of Toronto. Typically, one half of the impaction substrates and about 100 mg of ash samples were packed into 7 cm^3 acid prewashed plastic capsules and were subjected to INAA using a neutron flux ranging from 1 to $5x10^{11}$ n/cm^2 s for a

period of 5 min. to determine short-lived nuclide concentrations. Subsequently, irradiation at a flux of 2.5×10^{11} n/cm^{2}s for a period of sixteen hours was carried out to determine medium and long-lived nuclide concentrations, after an initial one to two weeks decay period.

Two multielemental reference standard of known accuracy with respect to trace elemnt content, viz. SRM 1632b sub-bituminous coal and SRM 1645 river sediment provided by U.S. National Bureau of Standards were used to determine the sample compositions by the 'comparator' method.

After nuclear irradiation, gamma photons emitted from the radionuclides were counted using solid state semiconductor detectors. A Canberra 8081 spectroscopy system and an Aptec MCA computer system were used to count the short and long-lived radionuclides respectively.

Scanning electron microscopy was used to study the particle-size distributions between the fine and coarse filters. The SEM photographs showed that the fine deposit consisted of particulates with mean diameters less than 2 μm, whereas the coarse deposit contained the remaining particles with sizes larger than 2 μm (See Fig 2a & 2b).

Results and Discussion

In Table 1 are the aerosol concentrations (i) downwind from a large Toronto hospital incinerator, (ii) in an urban airshed, (iii) industrial airshed and (iv) suburban airshed, shown as mean concentrations (ng/m^3) of samples over several months. Those elemnts marked (*) may be considered as potential 'hospital incinerator marker elements' both because of their enrichment in air particulates sampled near stack and also in the incinerator fly ash (Table 2). Particularly significant are the high concentrations of Ag, As, Cd, Cl, Co, Sb and Zn in the aerosols, a group which is considered to be hazardous to human health. This group also includes those elements found in incinerator flyash with elevated amounts. In addition, it was observed that crustal elements such as Ca, K, La, Mn, Na, Ti were relatively lower in

concentrations found on the aerosols downwind of the hospital incinerator than in their urban and suburban counterparts. This was attributed to the high sampling location of the incinerator aerosols, a site which was far away from ground level and hence relatively free from wind-entrained road dust and soil. The copper contents of the aerosols were unusually high; and this observation was recognized as a commom Hi-vol sampler problem : the contamination by the copper brushes in the motor. More definitive identification of incinerator 'marker elements' will be obtained in the near future when multivariate statistical factor analysis is completed on the aerosol concentration data set, thus yeilding the incinerator 'chemical factor'.

As an input into aerosol receptor modelling calculations it was of interest to obtain typical concentration patterns of incinerator emissions. Since trace element profiles were the main interest, incinerator ash was studied rather than stack samples. In Table 2 are the source elemental 'profile' for Toronto hospital incinerator. Of course this list of elements is not complete, missing in important marker elements for other pollution sources including Pb and Ni. These elements do not possess sufficiently large neutron cross sections and are not detectable by INAA. As a result, the aerosol and source samples will be subjected to instrumental photon activation analysis (IPAA) both to increase the scope of the analyzed elements (hence quality of the data set) and to check the accuracy of INAA.

The E.F. (enrichment factor) values for elements As, Cd, Cl, Co, Cr, Sb, Ti, Zn found in the ash samples are more significant than their absolute concentrations (4) and the E.F's range from values of about 5 to 10 for As, Fe, Ti to values >500-1500 for Se, Sb, Cd.

In Table 3 are the average elemental particle-size distributions for elements in the aerosols collected by a Sierra 2-stage Hi-vol impactor sampler at the hospital incinerator site. It was observed that elements including Al, Fe, Ca, K, Mn, Ti were present predominantly on large particles, as shown by the ratio of concentrations in fine to coarse portions (F/C in Table 3). These

elements are assumed to be associated with soil and crustal dust or particles produced by mechanical processes such as grinding and crushing (4).

Elements such as Br, Cl, Sb, Se were observed to be associated with ambient particulates exhibiting predominantly less than two micron particle-size distributions. These elements were considered to be associated with industrial combustion processes which produced fine particulates in the local atmosphere.

Of particular interest from the solid waste disposal point of view are the marked enrichments of As, Cd, Cl, Cr, Sb and Zn in the hospital incinerator ash, several of which might be attributable to disposal hospital plastic ware and medical items. In Table 4 are listed some recent results for plastics, a material commonly incinerated and which has recently been reported by De Bruin (5) to produce high inorganic contamination of incinerator ash. Orange and yellow plastics seem especially high in some metals, including Cd and Sb. In Table 5 are the prominent elements found in typical inorganic metal oxide pigments as provided by a manufacturer.

Conclusions and Future Research

The environmental impact of hospital incinerator emissions to the atmosphere in terms of toxic metal pollution is assessed to be significant, as it is evident from the enriched toxic metal particulate loadings of the ambient air downwind from such source. A quantitative source apportionment of the airborne particulate matter is to be carried out using statistical techniques such as factor analysis and chemical mass balance. Substances emitted from the stack are likely to undergo processes such as volatization, condensation and chemical transformation which will yield chemical composition patterns of the particulates different from those measured at the source. Therefore, it will be of interest to extract the source 'profile' from the large data set using a multivariate technique viz. absolute principal component score (APCS) method. Furthermore, the estimated contributions of the sources by APCS will be compared to those obtained by chemical mass balance as a means to characterize the merits and weaknesses of

such statistical techniques applied in the Toronto urban airshed.

Acknowlegement

The assistance from the SLOWPOKE-2 and SEM facilities at the University of Toronto, and the staff of the Toronto Western Hospital is gratefully acknowledged. Financial assistance is provided by OME ans NSERC.

References

1. R.J. Allen, et al, "Air Pollution Emissions from the incineration of Hospital Waste", JAPCA, vol 36, no.7, p. 829 (1986)

2. T.G. Pringle and R.E. Jervis, "A Particle-Size Specific Elemental Mass Balance For Apportionment of Ambient Aerosols", J. Radioanal. Nucl. Chem., 112 243 (1987)

3. Casolino, B.A.Sc thesis, University of Toronto (1988)

4. A.C. Chan, "Assessment of Ambient Particulates by Multi-elemental Radioanalytical and Receptor Modelling Techniques", M.A.Sc. Thesis, University of Toronto (1989).

5. P. Bode, M. De Bruin, et al., "Plastics from Household Waste As A Source of Heavy Metal Pollution: An Inventory Study Using INAA As An Analytical Technique", NIST/IAEA Conf.: Nuclear Techniques in the Life Sciences (1989); J. Radioanal. Nucl. Chem., (in press)

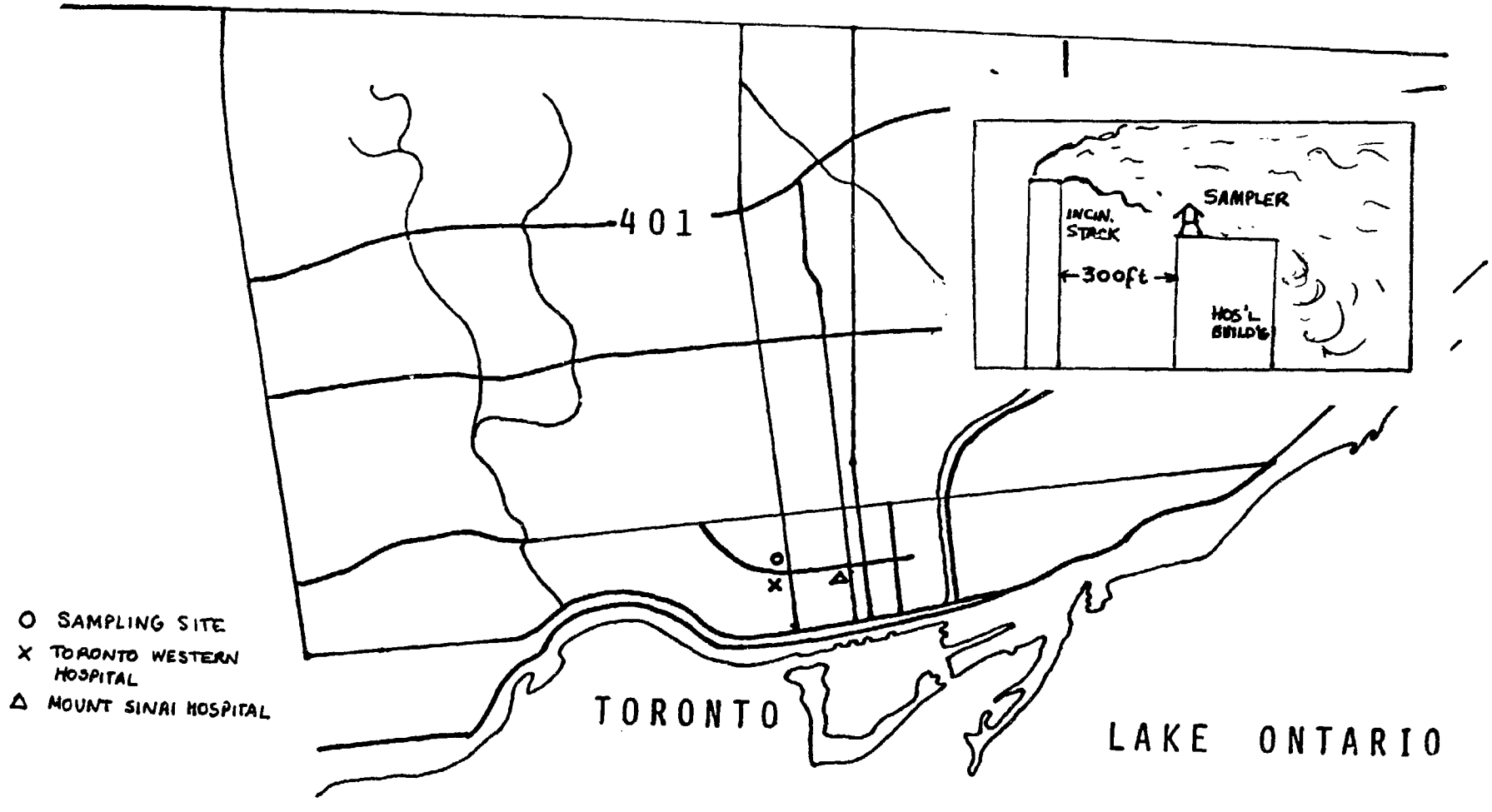

Figure 1 Ambient Particulates Sampling Site in Toronto

FIG 2 A SEM OF AEROSOLS COLLECTED ON 'FINE' FILTER, MEAN DIA. < 2 μm

FIG 2 B SEM OF AEROSOLS COLLECTED ON 'COARSE' FILTER, MEAN DIA. > 2 μm

Table 1

Aerosol Concentrations at Hospital Site and Other Toronto Areas (ng/m³)

Element		Hospital (1989)	Urban (1987)	Ind. (1988)	Suburban (1985)
Ag	*	6.3	2.3	>0.7	0.56
Al		1560	1450	3400	600
As		4.4	1.5	2.5	5.3
Br		27	28	18	70
Ca		3905	5700	9600	2150
Cd	*	1.05	---	>2.3	---
Cl	*	3000	1600	860	2340
Co		1.12	0.57	2.2	0.45
Cr	*	12.0	7.3	22	7.5
Cu		1360	1300	130	740
Fe	*	1640	1400	4300	640
I		1.4	1.5	0.73	3.2
K		550	480	1100	---
La		1.6	0.8	2.5	1.5
Mg		755	580	1099	---
Mn	*	115	63	110	34
Na		625	610	950	1520
Sb	*	4.3	1.7	2.6	1.4
Se		2.27	1.4	2.7	3.3
Ti		150	170	290	64
V		16.8	5.7	8.2	5.9
W		0.75	>0.36	960	---
Zn	*	334	100	270	108

* (hospital incinerator marker elements)

Note : Hospital --- Toronto Western Hospital, this work
Ind. --- Commissioners St. Site, Chan
Urban --- Queen's Park Site, Chan
Suburban --- Port Credit, Pringle

Table 2

Concentrations in Fly ash from Hospital Incinerator (ppm)

	Element	Concentration
*	Ag	60 ± 2.8
	Al	15200 ± 280
	As	98 ± 65
	Br	180 ± 0.7
	Ca	25500 ± 320
*	Cd	380 ± 10
*	Cl	29000 ± 98
	Co	18 ± 1.2
*	Cr	422 ± 15
	Cu	2.2 ± 0.06
*	Fe	96000 ± 1900
	I	6.8 ± 2.3
	K	42000 ± 3100
	La	13 ± 0.68
	Mg	2460 ± 98
*	Mn	1260 ± 22
	Na	18200 ± 130
*	Sb	860 ± 2.8
	Se	66 ± 1.8
	Ti	21000 ± 690
	V	15.4 ± 23
	W	12.4 ± 2.3
*	Zn	31000 ± 890

* (incinerator marker elements)

Table 3

Aerosol Concentration Distribution of Fine and Coarse Filters at Toronto Hospital Site (ng/m^3)

Element	Fine	Coarse	F/C
Ag	4.6	1.75	2.6
Al	215	1344	0.16
As	2.82	1.57	1.8
Br	19.5	7.5	2.6
Ca	418	3486	0.12
Cd	0.72	<0.3	>2.5
Cl	2375	625	3.8
Co	0.61	0.51	1.2
Cr	6.54	5.44	1.1
Cu	1112	247	4.5
Fe	397	1242	0.32
I	0.73	0.67	1.1
K	221	327	0.68
Mg	333	421	0.79
Mn	32	40	0.54
Na	252	372	0.68
Sb	3.19	1.12	2.9
Se	1.83	0.44	4.2
Ti	38	112	0.34
V	8.8	8.01	1.1
W	0.30	0.45	0.67
Zn	189	145	1.3

Note: 'Fine'--- mean diameter < 2 μm
'Coarse' --- mean diameter > 2 μm

Table 4

Concentrations of Impurities in Commercial Plastics (ppm)

Element	Colourless	Yellow	(De Bruin Dutch Plastics)
Al	316 ± 2.89	571 ± 3.91	
Ca	97 ± 4.85	94 ± 3.6	
Cd	---	3.2 ± 0.67	
Cl	17 ± 0.34	22.9 ± 1.0	2.0
Cu	---	---	
I	0.104 ± 0.001	0.45 ± 0.004	2.4
Mg	9.04 ± 0.72	20.8 ± 1.2	
Mn	0.16 ± 0.001	0.22 ± 0.001	
Na	57.6 ± 0.52	62.5 ± 0.63	
Ti	1.69 ± 0.51	84.8 ± 22.1	
V	0.02 ± 0.008	0.84 ± 0.09	
Zn			10.5

Note: Yellow sample with elevated Cd, V, Ti, Al.

Table 5

Prominent Elements in Typical Inorganic Metal Oxide Pigments

Colour	Elements
Yellow	Ni, Sb, Cd, Ba, Ti, Nb
Orange	Cr, Sb, Ni, Ti
Brown	Fe, Zn, Sb, Ti, Mn, Cr, Si
Blue	Co, Al, Si, Zn, Mo, Li
Green	Ti, Ni, Zn, Co, Mg
Black	Cr, Cu, Mn, Mo

FIG 2 A SEM OF AEROSOLS COLLECTED ON 'FINE' FILTER, MEAN DIA. < 2 μm

FIG 2 B SEM OF AEROSOLS COLLECTED ON 'COARSE' FILTER, MEAN DIA. > 2 μm

Compartmental Modeling of HMPAO and Calculation of Regional Cerebral Blood Flow

M. Mirzai, R. Palser
Dept. of Medical Physics,
University of Manitoba,
Winnipeg, Manitoba,
Canada

Abstract

A radiopharmaceutical, Tc-99m- labeled hexamethylpropyleneamine oxime (HM-PAO), has been reported to cross the blood brain barrier and to distribute in brain tissue in proportion to regional cerebral blood flow (rCBF). Although nuclear medicine images demonstrate a rapid uptake and prolonged retention of activity in cerebral structure, the pharmacokinetics of the radiopharmaceutical is poorly understood. Due to this lack of knowledge, only qualitative inference of rCBF rather than quantitative estimation can be made from the accumulation of radioactive information in the different regions of the brain. Although qualitative information on rCBF is useful, when serial intra-patient studies and inter-patient studies are compared, it is often impossible to determine whether rCBF has increased or not.

Over the past few years compartmental models have been formulated to describe the clearance of HM-PAO from blood to brain tissue and the efflux back to the blood.

This paper describes the computer simulation of the measurement of rCBF using Tc-99m-HMPAO. The compartmental model together with typical rate constants, are used to generate blood and tissue tracer activity curves. Gaussian noise and the use of non-linear regression analysis will allow the determination of mean and standard deviation of the computed rCBF. By varying the amount of added noise, and the number of data points fitted, the accuracy of the computed rCBF will be evaluated.

Introduction

Tomographic measurements of regional cerebral blood flow (TrCBF), refers to the measurement of regional cerebral blood flow (rCBF) by computed tomography in a series of adjacent brain slices. TrCBF measurements in clinical situations can be achieved by different methods such as positron emission tomography (PET) with ^{15}O labeled water (Herscovitch et al., 1983); single photon dynamic computer assisted tomography (DCAT) with radioactive ^{133}Xe (Stokely et al., 1980); and stable xenon enhanced computed tomography (XeCT) (Yonas et al., 1984). In practice all these modalities suffer from the disadvantage that measurements may be made on only a few slices through the brain. In addition PET and DCAT require specialized and expensive equipment available only in very few clinical centers.

The proposed method of quantitative TrCBF measurement makes use of a single photon emission computed tomography (SPECT) system (a rotating gamma camera) and has the following advantages over the other methods already discussed above: Firstly, since a SPECT camera produces cross sectional slices of the brain in one rotation around the head, rCBF measurements can be made throughout the brain volume, not just in a few slices. Secondly, no capital expenditure on equipment is required since SPECT systems are rapidly becoming standard clinical tools in the larger nuclear medicine departments. However, a major disadvantage of these systems is the length of time necessary for a complete rotation around the head. For a gamma camera this is about 20 to 30 minutes.

The main requirements for rCBF evaluation with SPECT are that radiopharmaceutical cross the intact blood-brain-barrier (BBB) and distributes proportional to blood flow. The tracer should retain a fixed regional distribution in the brain for a period sufficient to permit image acquisition.

Besides ^{99m}Tc-HMPAO, other radiopharmaceuticals that exhibit the same property include ^{123}I labeled N,N,N'-trimethyl-N'-[2-hydrooxy-3-methyl-5-iodobenzyl]-1,3-propanediamine (HIPDM) (Leonard et al., 1986)and N-isopropyl-p-iodoamphetamine (IMP) (Hill et al., 1982. Kuhl et al., 1982). However, compared to ^{99m}Tc-HMPAO, these latter compounds have several disadvantages. Firstly ^{123}I is costly to produce free from radionuclide contaminants and since it is cyclotron produced availability is limited. In comparison, ^{99m}Tc is readily available and infact is the most frequently used radionuclide in Nuclear Medicine Departments. Secondly, radiation dose considerations prevent administration of optimal quantities of ^{123}I radioactivity for estimation of regional radionuclide concentration from SPECT images. Typically 200MBq of ^{123}I-IMP or HIPDM is injected into the patient compared to 750MBq in the case of ^{99m}Tc-HMPAO. The smaller injected dose of IMP and HIPDM leads to higher uncertainty in quantitative SPECT imaging. Also ^{99m}TC-HMPAO is retained in the brain for a longer period of time compared to IMP and HIPDM.

Theory

The basic idea behind compartmental analysis centers on the concept of the compartment. Here a compartment is an amount of material which is homogeneous, well-mixed, and distinct from other material in the system. Ideally, a tracer introduced into a compartment is instantaneuosly uniformly distributed throughout the compartment, so that the concentration or specific activity in the out-flow from the compartment is equal to that within the compartment at that instant of time. in practice this ideal can only be approximated, and the deviation from the ideal becomes a limiting factor in the interpretation of the results. The system itself is then regarded as a finite number of compartments. Material can flow into and/or out of a given compartment and exchange between the compartments. A compartment in this sense is not usually a physical volume or physiological space.

We have made use of a four compartmental model to describe the transportof ^{99m}Tc-HMPAO to the brain tissue,which was first introduced by Neirinckx (1986). HMPAO is assumed to distribute itself in the four pools or compartments (Fig.1).

In this model, the first compartment is the arterial blood and the second compartment is the lipophilic diffusible tracer inside the brain tissue. The third compartment is the hydrophilic non diffusible tracer trapped in the brain tissue and the fourth compartment is the non diffusible tracer that is trapped in the blood. The rate constants, L's, define the transport of the tracer between compartments. Assuming that this trapping is irreversible, i.e., L(2,3)=L(1,4)=0, and that there is no passage of the non diffusible form of the tracer across the blood-brain-barrier, the following differential equations are given among the compartments. With UF(1) and UF(4) being the input functions (Lee et al., 1988).

```
dq(1)/dt=-L(2,1)*q(1)+L(1,2)*q(2)+UF(1)-L(4,1)*q(1)-L(0.1)*q(1)
dq(2)/dt=L(2,1)*q(1)-L(1,2)*q(2)-L(3,2)*q(2)
dq(3)/dt=L(3,2)*q(2)
dq(4)/dt=UF(4)+L(4,1)*q(1)-L(0,4)*q(4)
```

L(2,1) and L(1,2) describe the transport of HMPAO between the tissue and blood.
The clearance of lipophilic material from blood to tissue is given by:

$$L(2,1) = F*E \qquad (1)$$

where F is the flow and E is the extraction efficiency, which is given by Crone's equation as:

$$E = 1 - EXP(-PS/F) \qquad (2)$$

with PS being the permeability - surface area product.
L(1,2) describes the washout of lipophilic complex from tissue to blood.

For a freely diffusible complex such as Tc-99m labeled HMPAO,

$$L(1,2) = p*L(2,1) = p*F*E \qquad (3)$$

where p is the density of the tissue.
For the lipophilic Tc-99m-HMPAO complex, the rate of trapping is described by L(3,2) and can be calculated through the following:
The fraction of agent trapped, (R), is defined by:

$$R = L(3,2)/[L(3,2) + L(1,2)] \qquad (4)$$

The retained fraction in human brain has been determined by Andersen as reported in Ceretec, using a technique involving intra-carotid injection of Tc-99m-HMPAO and analysis of the washout curves in the first pass. The value obtained for R is 0.6. The same approach could be used to calculate L(4,1).

Analysis

Having the four compartmental model and with the use of the SAAM (Simulation, Analysis, and Modeling), (Berman, 1978) program, one is able to get the value of the rate constants, blood flow, and the time-activity curves for different compartments. Figure 2 shows the time-activity curve for compartment 5, which is the total activity of the system. From the graph, one can see that, the maximum activity is at about 1.5 to 2.0 minutes after administration of the tracer and then at about 5.0 minutes after administration it goes to equilibrium.

Having too many parameters, it is logical to want to reduce this many parameters and treat them as a constant as much as we can. To do this, we have to see what kind of effect would changing each rate constant have on the time-activity curves. Each rate constant was varied between the ranges of -75% to +75% of its original value while keeping the other three at their initial value. The results of this is summerized in figure 3.
It was found that changing L(2,1) had the most effect on the time-activity curves, furthermore, there was a linear relationship between the two. The least change was for L(4,1), in other words, a change of +/-75% in L(4,1), only led to change of about 3% in the activity level. Thus, L(4,1) can be considered as a fixed parameter rather than a variable.

To simulate the change in flow, magnitude of noise and the number of data points chosen is to be considered. Ten points out of the 20 were chosen over the interval of ten minutes, and in increments of 1.0 minutes.The activity curves therefore were modified by the addition of random noise, and the use of regression analysis algorithem to recalculate the rate constants and rCBF. By varing the amount of added noise, and the number of data points fitted, the accuracy and precission of the measured rCBF will be evaluated. Figure 4 shows a graph of flow for different noise inputs.

Conclusion

From our results the values for the rate constants were found to be 0.65, 0.63, 0.97, and 0.95 [1/(min)] for L(1,2), L(2,1), L(3,2), and L(4,1) respectively. The mean value for the flow using the selected points on the activity curve and the standard error given to it was found to be 0.80 +/- 10% variation. This comes about from the fact that in our work, a standard error of about 0.5 corresponds to an error of around +/- 13% on the equilibrium level of the total time-activity curve.

References

Berman M, Weiss MF: SAAM Manual, U.S. Department of Health, Education, and Welfare, Publication No.(NIH) 78-180,1978.

Ell PJ, Costa DC et al: The clinical application of rCBF imaging by SPECT.(Ceretec). 1987.

Herscovitch p, Markham J et al: Brain blood flow measured with intravenous $H_2{}^{15}O$. I. Theory and Error Analysis. J Nucl MED 24: 782-789, 1983.

Hill TC, Holman L et al: Initial experience with SPECT of the brain using N-isopropyl I-123 p-iodomphetamine: concise communication. J Nucl Med 23: 191-195, 1982.

Kuhl DE, Barrio JR et al: Quantifying local cerebral blood flow by N-isopropyl-p-[^{123}I] iodoamphetamine (IMP) tomography. J Nucl Med 23: 196-203, 1982.

Lee TY et al: A Quantitative Theory for the Measurement of Cerebral blood flow with ^{99m}TC-HMPAO and SPECT. Phys. Med. Biol. 33, supp.1, 114, 1988.

Neirinckx RD: Clinical experience with Ceretec, the first widely available Tc-99m agent for rCBF measurement. RAD, 131,18, 1986.

Stokely EM et al: Asingle photon dynamic computer assisted tomography (DCAT) for imaging brain function in multiple cross- sections. J Comput Assist Tomogr 4: 230-240, 1980.

Yonas H, Wolfson SK et al: Clinical experience with the use of xenon enhanced CT blood flow mapping in cerebral vascular disease. Stroke 15: 443-450, 1984.

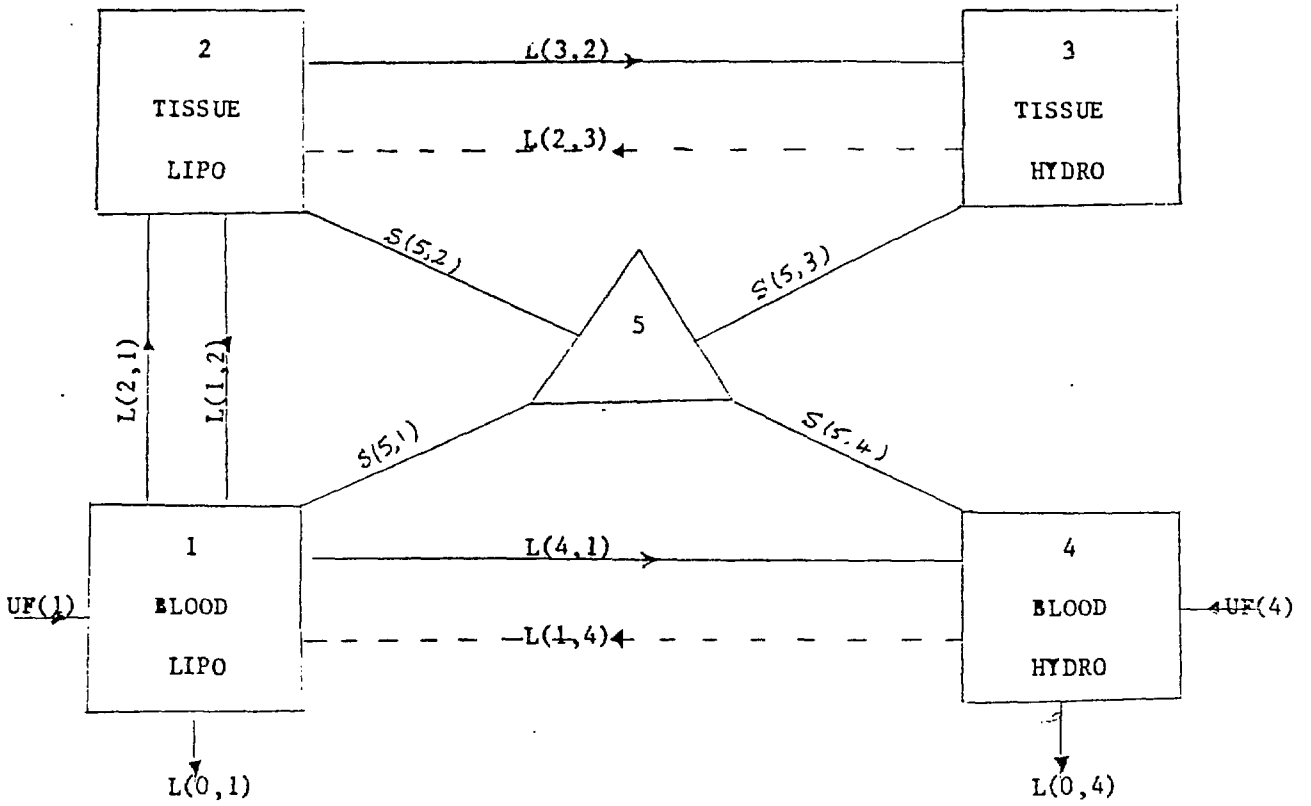

FIG. 1. A Four Compartmental Model of the Brain.

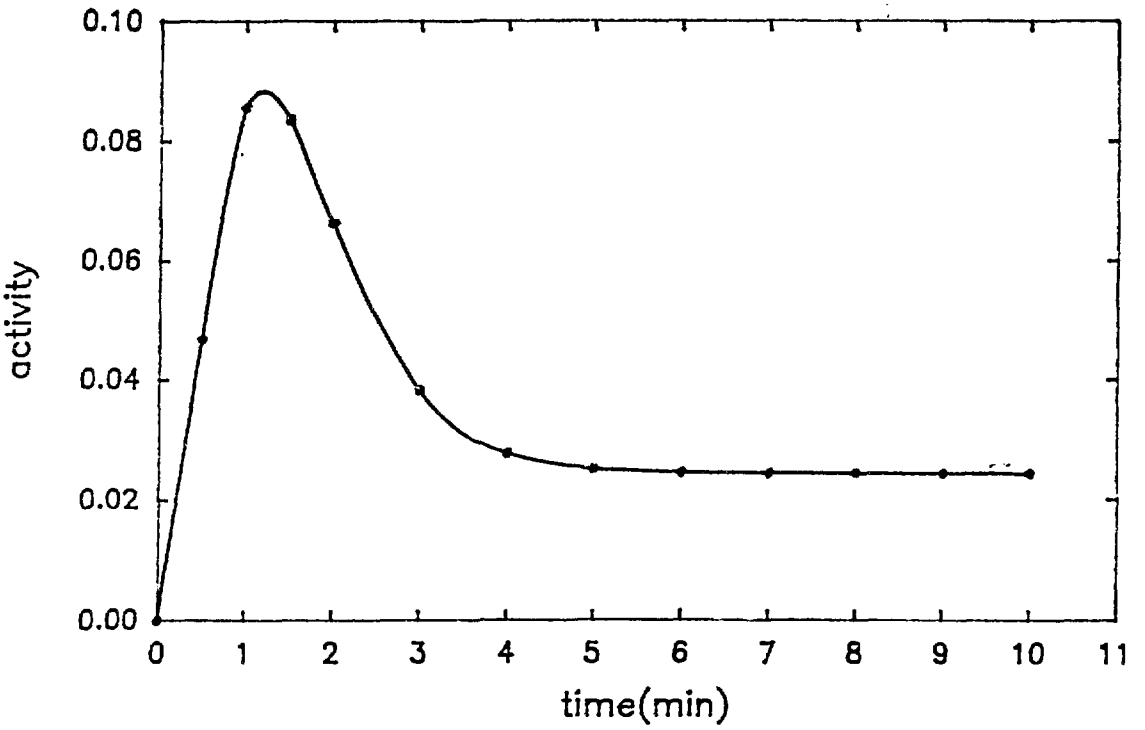

Fig.2. Total activity of the four compartments vs time.

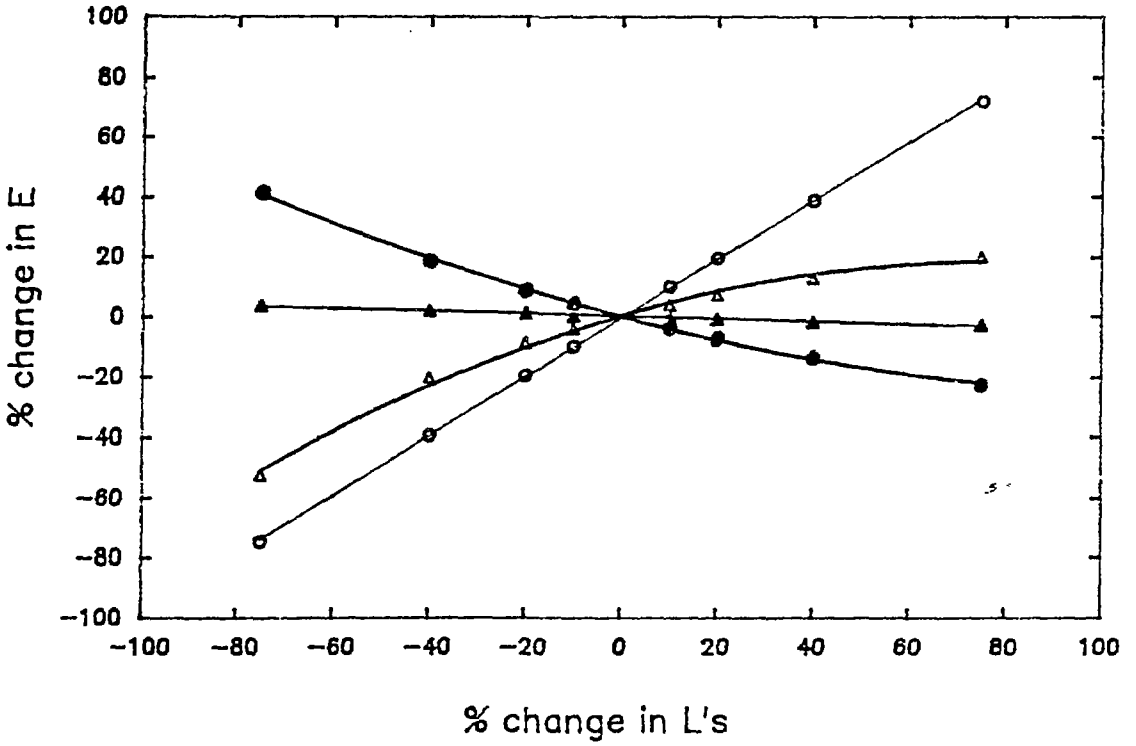

Fig.3. Relation between and the rate constants.
(E represents the equilibrium level of activity).

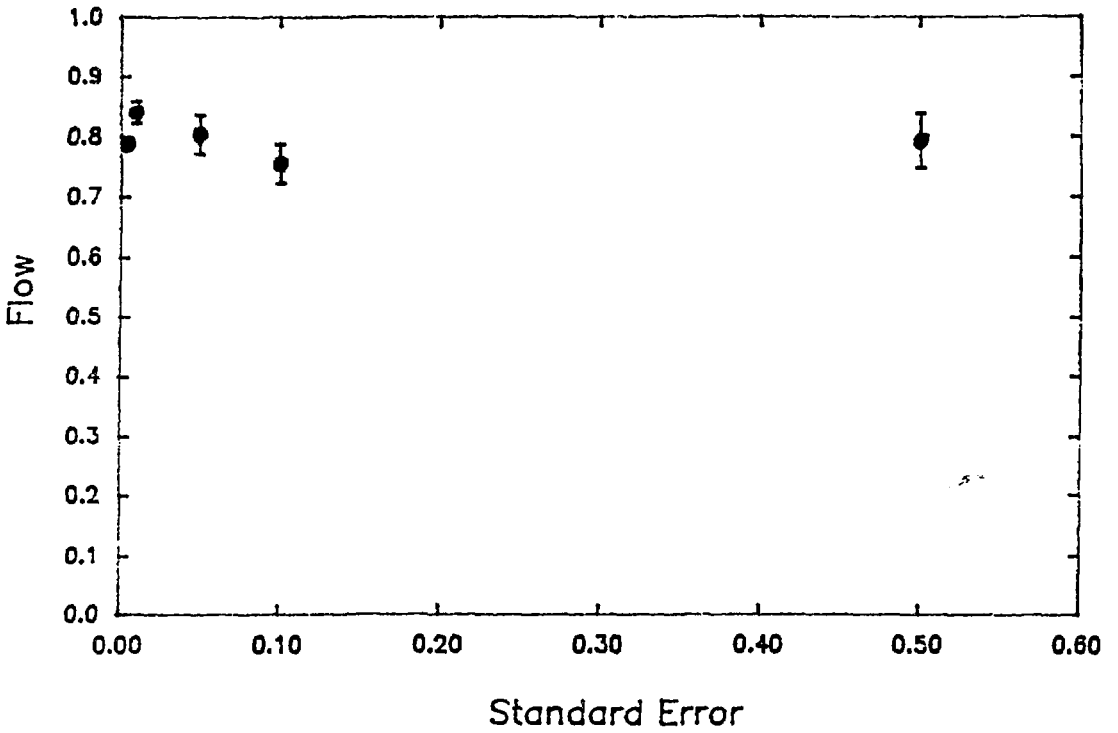

Fig.4. Graph of flow vs standard error.

Instrumentation of a High Energy Proton Detector and the Photon Tagger at SAL

Ken Garrow , Dept. of Physics ,
Queens/Trent University

1.0 Abstract

A $^{12}C(\gamma, p_0 + p_1)^{11}B$ differential cross-section at 40° with a photon energy of 60 to 100 MeV in the lab system was preformed at SAL (Saskatchewan Accelerator Laboratory). The results of the absolute differential cross-section compared to the results of Matthews[1] will verify the operation of the tagger and the proton detector are correct. The results will also yeild a value for the energy resolution of the proton detector.

2.0 The Photon Tagger

The photon source produced by the tagger is of bremsstrahlung origin. That is the "breaking radiation" emitted by the deflection of a charged particle (electron) in the coulomb field of the nucleus.

The fraction of the bremsstrahlung scattered electrons in the focal plane of the tagger spectrometer (see figure 1) determines the efficiency of the tagging system. The tagging efficiency is defined as:

$$\text{eff} = \frac{\text{number of } e^- \text{ in the focal plane in coincidence with the photons detected in a lead glass detector placed in the beam}}{\text{number of } e^- \text{ detected in the focal plane}}$$

It is obvious that the angular distribution of the bremsstrahlung photons and scattered electrons (both of which are forward peaked) must be known. This has been calculated by the Bethe-Heitler bremsstrahlung differential cross-section in both photon energy and scattered electron angle. Using this relationship in conjuction with the magnetic - spectromer the electron of known energy E_0 incident on the radiator produces a photon of energy k , such that the scattered electron has energy $E = E_0 - k$. The scattered electron energy is determined by the spectrometer focal plane detector system and therefore the energy of the tagged photon produced is known.

The focal plane detector consists of an array of overlapping Ne102A scintillators coupled to light guides and then to photomultiplier tubes. As shown in figure 2 , the width the focal plane detector spans of the momentum range of the bremsstrahlung electrons determines both the energy range and the energy resolution of the emitted photon. The focal plane detector built at Trent and SAL is about 1 / 3 the size of the one currently in use at SAL. This will yeild a photon with an energy resolution three times better than the one in use at the moment.

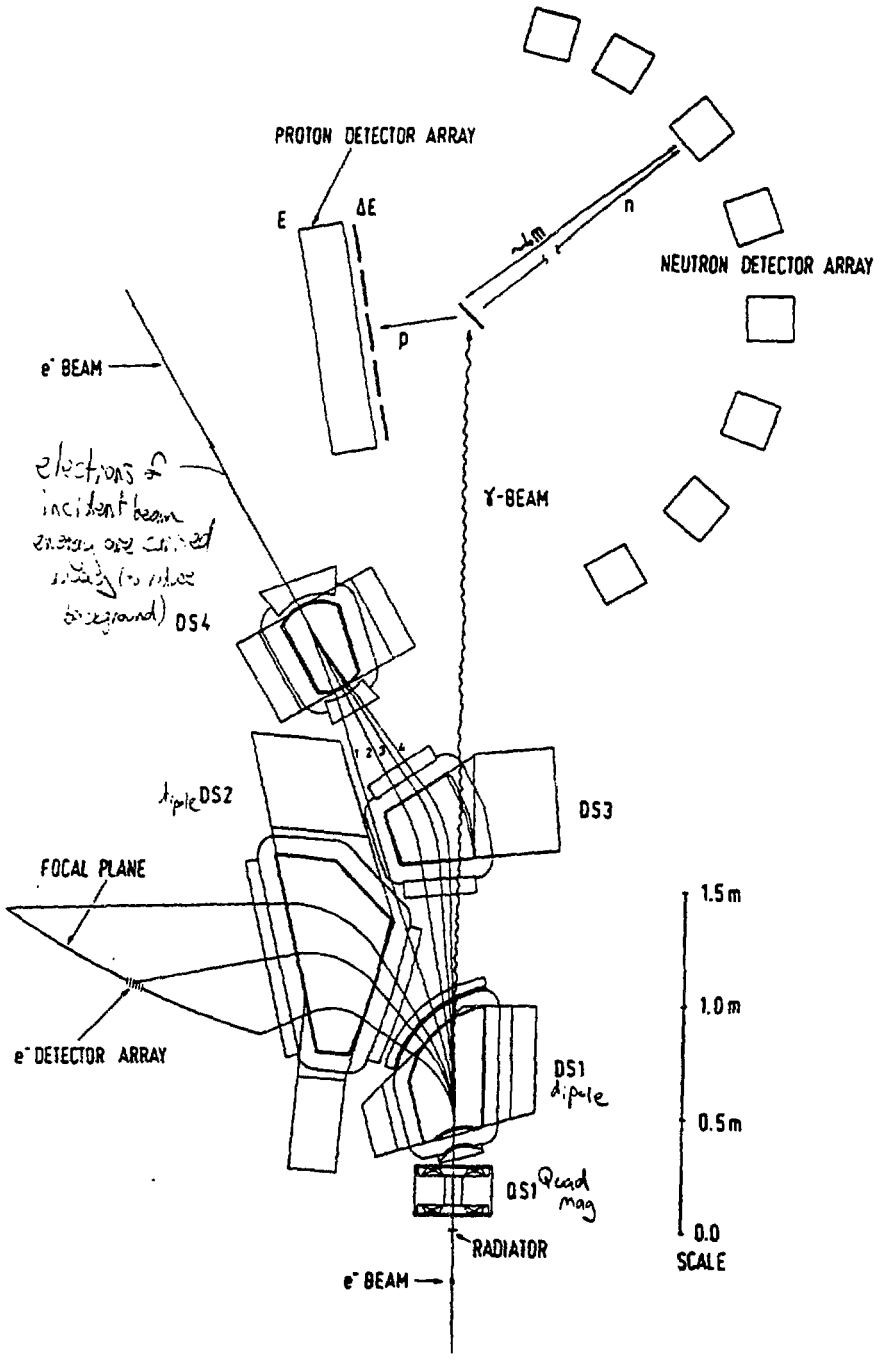

Fig.1. Tagged photon spectrometer, showing focal position and typical experimental set-up (2)

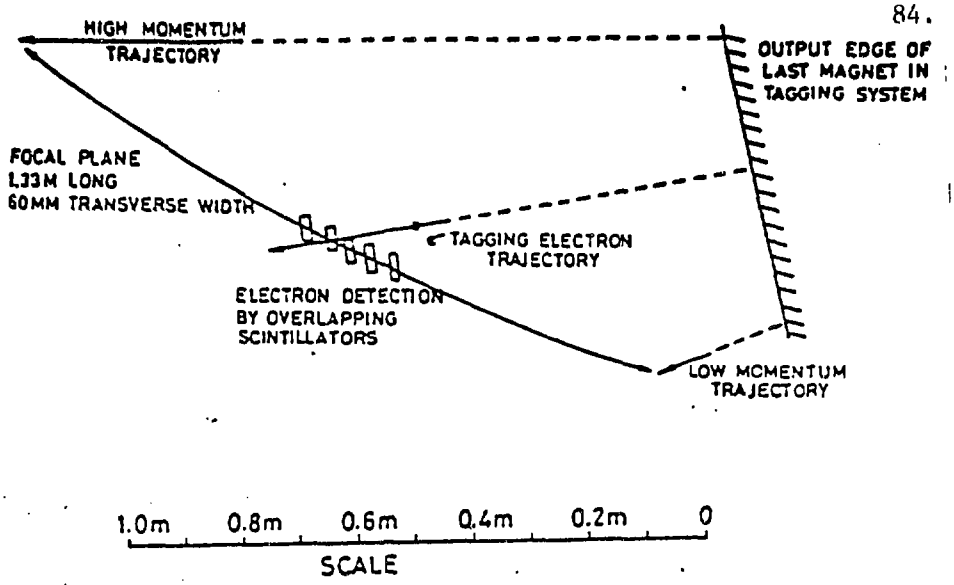

Fig. 2 Spectrometer focal plane geometry showing the central and low and high momentum trajectories.(2)

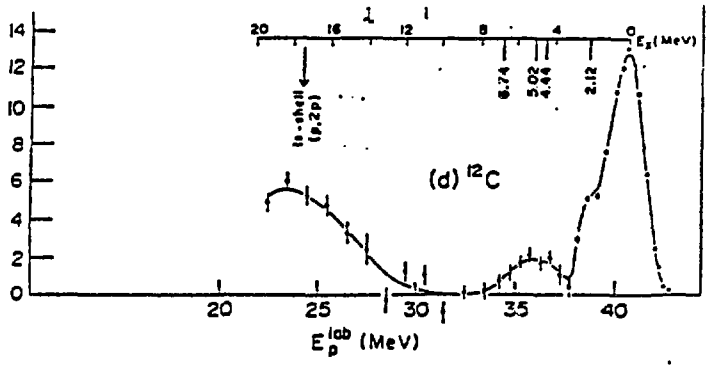

Fig. 3 Photoproton spectra for $E_\gamma = 60 \pm 1$ MeV, $\theta = 45°$ derived as described in the text from data such as those shown in fig. 7: (a) $^6Li(\gamma, p)^5He$; (b) $^7Li(\gamma, p)^6He$; (c) $^9Be(\gamma, p)^8Li$; (d) $^{12}C(\gamma, p)^{11}B$. The scale above each spectrum gives the excitation energy in the residual nucleus, with lines indicating the positions of known excited states. The location of the 1s shell peak observed in the (p, 2p) reaction is also marked.(1)

3.0 The Delta-e-Delta-e-E Detector

This detector actually consists of two seperate detectors.The delta-e-delta-e part of the detector was constructed at Trent University and the E part was constructed at the University of Melbourne , Australia and SAL. The delta-e-delta-e detector consists of a 1mm amd a 10mm piece of Ne102A scintillators. These scintillators are contained in light tight box whose inside consists of a light reflecting material. The two scintillators are optically separated in the box with two Phillips XP2012B photomultiplier tubes viewing the 1mm scintillator for increased voltage output and one tube viewing the 10mm scintillator. The scintillators have an effective detection area of 144 sq. cm (that is 12cm x 12cm).

Since this design (a reflecting box detector) is unique to the more common but less versitile optically coupled "paddle" type detectors , some uniformity tests were performed at SAL to give an understanding of the detectors operation and limitations.

In a procedure similar to the one imposed by Matthews[3] on thier delta-e detector , the pulse hieght uniformity , mean response channel number of the ADC and the count uniformity were measured at various points across the surface of the scintillator. A .1 mCi ^{106}Ru beta source was used as this was the only sufficiently "strong" particle source available. The mean response channel number of the ADC is given as:

$$(\text{mean response channel}) = \sum_{\text{channels}}[(\text{channel \#}) \times \text{counts}] \; / \; \sum_{\text{channels}}(\text{counts})$$

The pulse height deviation over the scintillator surface of the mean response channel number was found to vary by about 10%, while the standard deviation in the mean response channel number over all runs gave an error in the mean response channel number of about .5%. This later value gives an indication of the reproducability of the measurements and is defined as:

$$(\text{error}) = \sqrt{\sum_{\text{runs}}[(\text{mean response channel}) - (\text{ave. mean response channel})]^2}$$

Finally the count uniformity was determined to fluctuate by about 10% across the surface of the detector. These results were compared to those of an optically coupled detector and the reflector box detector was found to be of comparable uniformity.

The E detector is a 16.5 cm x 16.5 cm x 36.0 cm block of Ne102A scintillator coupled directly to a 5 inch Phillips XP2010B photomultiplier tube in a light tight box.

4.0 Operation of Delta-e-Delta-e-E Detector

The equation expressing the average energy loss of a proton per unit distance travelled through a medium (in MeV per cm)[2] is:

$$-\frac{dE}{dx} = \left(\frac{e^2}{4\pi\varepsilon_o}\right)^2 \frac{4\pi n Z^2}{mc^2\beta^2}\left[2\ln\left(\frac{p}{Mc}\right) + \ln\left(\frac{2mc^2}{I^2}\right) + \ln\left(\frac{2mc^2\beta^2}{1-\beta^2}\right) - 2\beta^2 - \delta - U\right]$$

where:

M = mass of incident particle
m = mass of electron
n = number of atomic electrons per m^3 ($N_{Av}z\rho/A$)
β = v/c
p = the momentum of incident particle
Z= atomic number of incident particle
I = mean ionization potential
δ = the density effect term
U = the shell effect term

From this equation it should be noted that the faster the particle travels the less energy it loses per cm while at the same time the heavier the particle the more energy it loses in the medium per cm. This gives a particle separation according to the mass of the particle with a dependence on the kinetic energy of the partilce as it passes through the different thicknesses of scintillator. The particle separation of the delta-e-delta-e-E is shown in figure (4). The scatter plot shows separation between proton, pion and electron events is distinct as it should be.

5.0 The Differential Cross-section Calculation

The absolute differential cross-section for a particular photon energy and proton angle is given as[5]:

$$\frac{d\sigma}{d\Omega_p} = \frac{\text{proton yeild}}{N_c\, d\Omega\, N\gamma}$$

where:
N_c = nuclei of ^{12}C per cm^2 in the target
$d\Omega$ = solid angle factor (determined by delta-e detector)
$N\gamma$ = number of photons incident on target which is calculated from the product of the tagging efficiency with the number of electron counts for a particular focal plane channel number

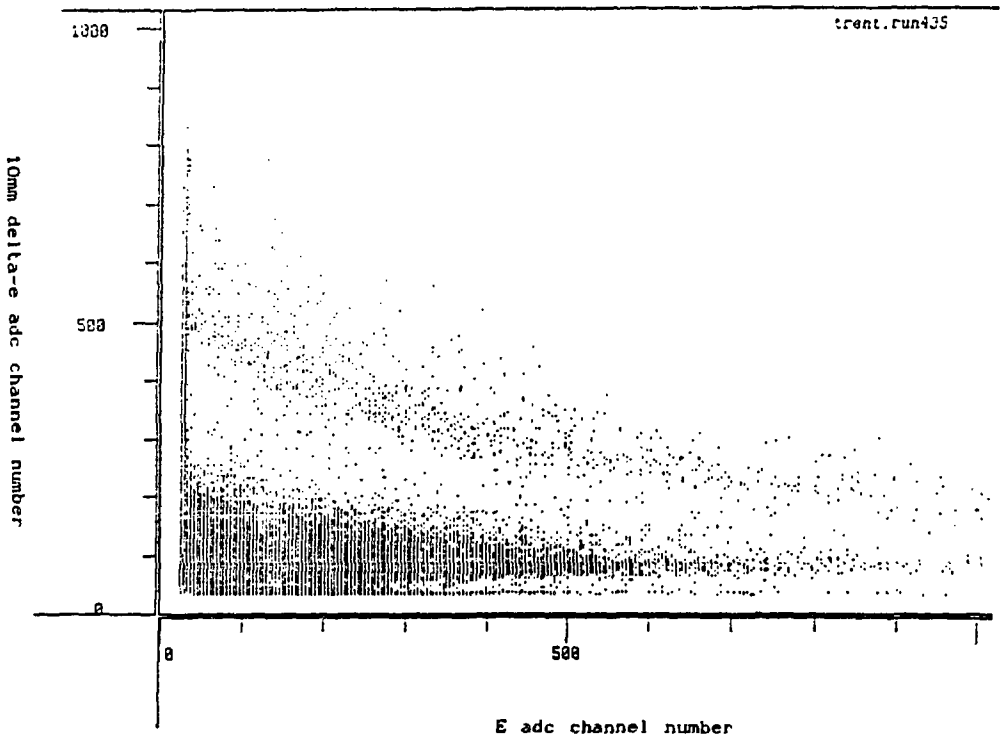

Fig.4. Skatter plot of delta-edelta-e-E detector with the 10 mm delta-e scintillator adc channel number as ordinate and the E scintillator as abcissa. The separation between electrons,pion and proton events is evident.

A graph of counts verses proton energy for a particular photon energy and proton angle (or similarly $d^2\sigma/d\Omega\ dE_p$) will give an approximate value of the energy resolution of the detector (see figure 3).

The large peak in ^{11}B at the high proton energies are transitions to the ground state with a small deformation of the bump near the base on the low energy side corresponding to transitions to the first excited state which is 2.1 MeV above the ground state. The next bump corresponds to the second and third excited state transitions which are at 4.4 and 5.1 MeV above the ground state.

Therefore , from such a graph of counts versus proton energy will yeild a value of the energy resolution of the delta-e-delta-e-E detector. Finally the correct operation of the tagger and proton detector will be indicative of the absolute differential cross-section at proton angle of 40° and photon energy in the range 60 to 100 MeV as compared to previously published values such as Matthews[1].

References:

1) Matthews, J.L. Nuclear Physics A267 (1976) 51.
2) Kellie, J.D. Nuclear Instruments and Methods in Physics Reaserch A247 (1985) 153.
3) Matthews, J.L. Nuclear Physics A112 (1968) 654.
4) Paul J.M. Nuclear Instruments and Methods 96 (1971) 51
5) Harty, P.D. Physical Review C 37 (1988) 13.

NEUTRON DOSIMETRY USING BUBBLE DETECTORS AND AN ANTHROPOMORPHIC PHANTOM

GUY DESNOYERS
DEPARTMENT OF CHEMISTRY AND CHEMICAL ENGINEERING
ROYAL MILITARY COLLEGE OF CANADA
KINGSTON, ONTARIO, CANADA
MARCH 1990

Neutron transport in air and energy deposition on and in an anthropomorphic phantom, arising from irradiation with a Californium-252 neutron source, were investigated using superheated drop Bubble Detectors as dosimeters and spectrometers. The intent of these experiments was to determine the ideal location for the wearing of a dosimeter,and the effect of body orientation with respect to the source of radiation on dosimeter reading.

1. INTRODUCTION

In 1987 the Canadian Armed Forces Navy was directed by the Government to proceed with a proposal for the eventual acquisition of Nuclear Submarines.

Land based nuclear reactors have very thick radiological shielding and the neutrons released from fission penetrating the shielding are progressively absorbed, with the energy released in the form of gamma-ray (γ) radiation. The radiation escaping the radiobiological shield thus consists primarily of gamma-rays and the biological effects of these are better known than for the case of neutrons.

On board nuclear submarines a greater fraction of the escaping dose is from neutrons, due to the smaller biological shield necessitated by weight and volume restrictions.

Regular passage in close proximity to the nuclear reactor is required as the only access to the machinery spaces while underway is through the nuclear boiler compartment. Unofficial talks with personnel involved in the Submarine acquisition program identified health problems with personnel working in such close proximity to a nuclear reactor as in the Nuclear Submarine environment.

New radiobiological results from low doses experiments suggest the possibility of a greater biological effect from neutron radiation than had previously been provided for in international recommendation and national laws and guidelines on radiation protection (1,2). The fluence to dose conversion factors are under review and suitable data conforming to the definitions propounded by the International Commission on Radiological Protection (ICRP) and the International Commission on Radiation Units and Measurements (ICRU) is being assessed (3). Thus the need for accurate neutron dosimetry on board a submarine is obvious.

2. Neutron Irradiation of an Anthropomorphic Phantom

Factors significantly affecting the biological effects of radiation are the type of radiation, the angular and spatial distribution of the incident radiation, and the energy spectrum. The biological effects therefore may not be the same if the person is irradiated from the front, the back or the side, nor will they be the same for different parts of the body. Of course the body orientation greatly effects the dosimeter reading, wherever it is worn.

Anthropomorphic phantoms have been developed to accurately represent the human body. The phantom used in this work was a Humanoid RT-200 which is comprised of a 50th percentile male skeleton encased in tissue equivalent plastic and which has detailed contours. The Hydrogen content, which is especially important for neutron

dosimetry, is identified by the ICRU as around 10% for the reference man (4), this compares well with the experimentally determined RT-200 phantom which has 9.6 % hydrogen for body plastic and 7.1 % for the lung plastic (5). Irradiation of the phantom close to a ^{252}Cf source is a good representation of the submarine scenario.

3. Bubble Detectors

A new type of passive detector based on the theory of the Bubble Chamber and appropriately called the "Bubble Detector" (6-10) appears to fulfill all the desired qualities required of a personal detector, including limited live information. Other more fundamental characteristics of the Bubble Detector are its variable sensitivity (from environmental to criticality levels) its relatively flat flux-energy response from 100 keV up and its total gamma-ray insensitivity. The Bubble Detectors were used here on and in the phantom to measure the neutron kerma.

The theory of the bubble detector lies in the fact that neutrons may interact with the superheated liquid (enclosed in a polymer gel) to initiate bubble nucleation, due to locally deposited energy. The bubble grows, but is held at the interaction site. Simply counting the bubbles gives a measure of fluence or dose, as shown in figure 1.

By selecting different detector liquids and varying the degree of superheat of the detector liquid, Bubble Detectors can also be prepared which possess neutron energy thresholds at approximately 10 keV, 100 keV, 600 keV, 1500 keV, 2500 keV, and 10,000 keV (11). Thus by combining these, a crude spectrometer nay be formed which is small and requires no power, allowing insertion in a phantom, or other locations which are inaccessible to more conventional spectrometers.

4. Mid Line Free in Air Kerma

The Mid Line Free In Air Kerma (MLFIAK) was determined at various stages of the experiments. This was done to verify the accuracy and consistency of the detectors. The Defence Research Establishment Ottawa (DREO) ^{252}Cf source had a strength ranging from $1.22 \times 10^{7} \pm 8\%\ ns^{-1}$ down to $1.17 \pm 8\% \times 10^{7}\ ns^{-1}$ over the course of the experimental work. The bubbles can easily be counted visually and the results are directly proportional to a dose equivalent. Conversion to kerma used a Q value of 0.1075 rad/rem (12). Table 1 summarizes the results.

Table 1. Tabulated Averaging of the Mid Line Free in Air Kerma Response at 170 cm from the Source

MID LINE FREE IN AIR KERMA RATE in mrad/hr								
run #	10	11	12	15	21	25	26	27
kerma rate	0.53	0.54	0.57	0.65	0.65	0.57	0.54	0.56
Experimental Average = 0.58 ± 0.06 mrad/hr								
Theoretical + Scatter = 0.56 ± 0.06 mrad/hr								

5. Scattering Contribution

The scattering contribution was determined by placing a shadow bar of mild steel mid way in the line of sight between the source and the standard position of the Mid Line Free in Air Kerma, 170 centimeters from the source, and irradiating three detectors. The measured neutron scattering contribution was 0.13 ± 0.02 mrad/hr. The measured values and theoretical plus scatter values compare extremely well.

6. Phantom Irradiation

The Humanoid RT-200 anthropomorphic phantom was irradiated facing, left side to, and back to the

Californium-252 neutron source and the dose rates at different external and internal locations (fig. 2) were measured using BD-100R reusable neutron detector. Thus the effect of the dosimeter location on recorded dose was examined.

The phantom was suspended in the standing position from an overhead beam with a harness. The suspension point of the phantom was such that, regardless of the orientation, the Mid Gut Bubble Detector was always a distance of 170 cm from the Californium source. The results in table 2 are expressed as transmission factors which are simply the determined kerma at the detector location divided by the average value of the MLFIAK of 0.58 mrad/hr.

Table 2. Transmission Factor of different detector location with respect to the phantom orientation

SOURCE: Californium-252		STRENGTH: $(1.20 \pm 0.11) \times 10^7$ n/s	
TARGET: Humanoid RT-200			
DETECTOR: Bubble Detector Model BD-100R			
Transmission Factor			
Location	Phantom Orientation		AVERAGE
	Front	Left Side	Back	
Front Gut	1.42	0.85	0.14	0.80 ± 0.64
Middle Gut	0.38	0.09	0.36	0.28 ± 0.16
Back Gut	0.09	1.08	1.49	0.89 ± 0.72
Left Wrist	1.15	1.41	1.15	1.24 ± 0.15
Right Wrist	1.15	0.12	1.15	0.81 ± 0.59
Chest	1.23	1.01	0.16	0.80 ± 0.57

Table 3. Variation of the Transmission Factor with respect to the phantom orientation.

LOCATION	FG	MG	BG	LW	RW	CH
VARIATION	10.1	4.2	16.6	1.2	9.6	7.7

Table 4. Averaging of the Transmission Factor for two detectors with respect to the phantom orientation.

Detectors	FACING	LHS	BACK	AVERAGE
(FG+BG)/2	0.76	0.97	0.82	0.85 ± 0.11
(CH+BG)/2	0.66	1.05	0.83	0.85 ± 0.20
(LW+RW)/2	1.15	0.77	1.15	1.02 ± 0.22

7. Bubble Detector Spectrometer Unfolding Technique

Spectral unfolding was done by the spectral stripping method which has the advantage of being able to be manually calculated, but unfortunately suffers greatly from error accumulation. As the stripping progresses the errors at lower energies grow to unacceptable proportions and negative fluences are obtained unless data statistics are extremely good

The detectors are threshold detectors and accordingly any measured data is ideally from a neutron energy at or above the detector threshold The detector responses are shown in figure 3. Average cross-sections (σ_{ij}) of the BDS were determined for different energy intervals, resulting in an upper triangular matrix. The measured data of the six threshold detectors results in a tridiagonal matrix problem as shown below in equation 1.

$$\begin{pmatrix} R_1 \\ R_2 \\ R_3 \\ R_4 \\ R_5 \\ R_6 \end{pmatrix} = \begin{pmatrix} \sigma_{11} & \sigma_{12} & \sigma_{13} & \sigma_{14} & \sigma_{15} & \sigma_{16} \\ 0 & \sigma_{22} & \sigma_{23} & \sigma_{24} & \sigma_{25} & \sigma_{26} \\ 0 & 0 & \sigma_{33} & \sigma_{34} & \sigma_{35} & \sigma_{36} \\ 0 & 0 & 0 & \sigma_{44} & \sigma_{45} & \sigma_{46} \\ 0 & 0 & 0 & 0 & \sigma_{55} & \sigma_{56} \\ 0 & 0 & 0 & 0 & 0 & \sigma_{66} \end{pmatrix} \begin{pmatrix} N_1 \\ N_2 \\ N_3 \\ N_4 \\ N_5 \\ N_6 \end{pmatrix} \quad (1)$$

where R is the response of the detectors (# of bubbles), the upper diagonal matrix is the response matrix averaged from experiments, and N is the number of the neutrons, the unknown desired. To find the value of N_6 the following calculations are done:

$$R_6 = \sigma_{66} N_6 \quad (2)$$

and

$$N_6 = \text{neutron fluence} = R_6 / \sigma_{66} \quad (3)$$

Similarly the number of neutron in the energy region of 2,500 to 10,000 keV is N_5 which is found by solving

$$N_5 = (R_5 - \sigma_{56} N_6) / \sigma_{55} \text{ , etc.} \quad (4)$$

This method was used to determine the energy spectra (which are discussed below) in figures 7-10.

8. Discussion

The mean BD-100R Reusable Neutron Detector Free in Air Kerma result is within 4 % of the expected value and within 16 percent of the worst case experimental value. Considering that the source strength of $(1.22 \pm 0.11) \times 10^7$ neutron per second has only an 8 % accuracy, and that the average counting statistical error was around 15 %, the results of the BD-100R are excellent. Figure 6 shows the experimental trend (FIA), the theoretically calculated kerma, and the theoretical plus scatter contribution.

For and ideal dosimeter the transmission factors would be 1.0 regardless of orientation as exposure limits are generally calculated as a function of the Free in Air Kerma. The problem is to know the orientation of the person with respect to the source at the time of irradiation. The variation in the Transmission Factor in figures 4 and 5 (from table 3) shows the spread in the confidence of an accurate measurement. In table 4 the average of two possible dosimeters is presented for the 3 orientations.

Figures 7 to 10 show the unfolded spectral results. Figure 7 is a plot of the two FIA irradiation runs compared to the theoretical Watt spectrum. Although the general trend is adequate and low energy scatter is evident, the repeatability of the measurements were not very good and some negative fluence occur. In figure 8 the high an low values (± statistical error) of the FIA are plotted to determine the repeatability of measurements. For the BDS-100 and 2,500 the readings are not within tolerance. Figure 9 is a plot of the detector raw counts normalized for different location on the body. The total kerma was calculated from the BDS raw counts and found to correspond very well with the BD-100R kerma (table 5).

Table 5. BD-100R and BDS kerma rate comparison

	KERMA RATE (mrad/hr)					
LOCATION	FIA	FG	MG	BG	WRISTS	CH
BD-100R	0.58	0.82	0.22	0.05	0.49	0.71
BDS	0.65	0.79	0.19	0.06	0.45	0.74
% DIFFERENCE	12	4	16	20	9	4

Figure 10 is a plot of the spectra energy for three gut detector locations. Again the general trend is positive but it is very evident that the detector responses are not what they should be as negative fluence occur due to a combination of error propagation (poor statistics) and varying detector sensitivity.

10. Conclusions and Recommendations

The BD-100R reusable neutron detector is a reliable neutron detector. Considering that the neutron risk assessment appears underrated, a 10 fold error in the measurement of the kerma is unacceptable. A minimum of two detectors should be worn, preferably one at the front gut and one at the back gut position as they represent some of the most vital areas of the body. The two wrists are also a very good location. Common sense would prevail in the selection of the location depending on the work involved. The BD-100R is recommended as a personal dosimeter as it not only provides real time information, but it is has a good energy response from 100 keV up.

The Bubble Detector Spectrometer set data provided limited useful information. The total kerma contribution evaluated from the detectors was comparable to that from the BD-100R detectors but the error accumulation in the spectral unfolding voided the data. The detectors did not have repeatability over the course of time. The detectors are considered to be still in the development stage, however have enough advantages that further research is warranted.

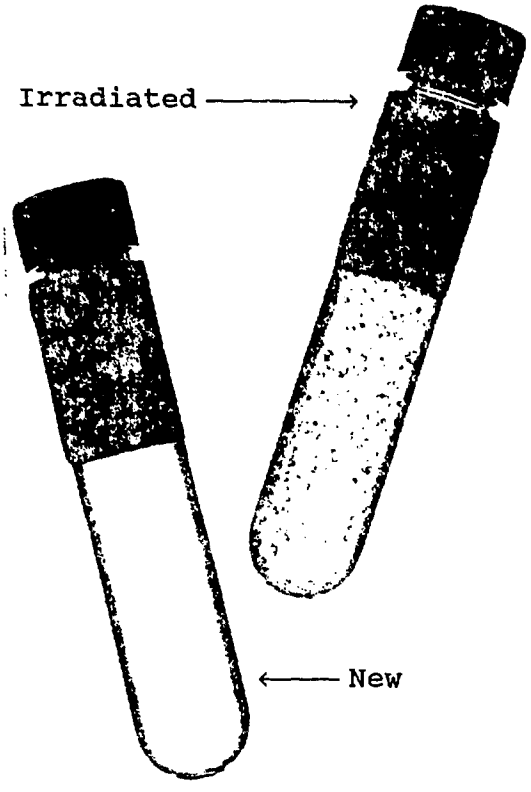

Figure 1. BD-100R reusable neutron detector

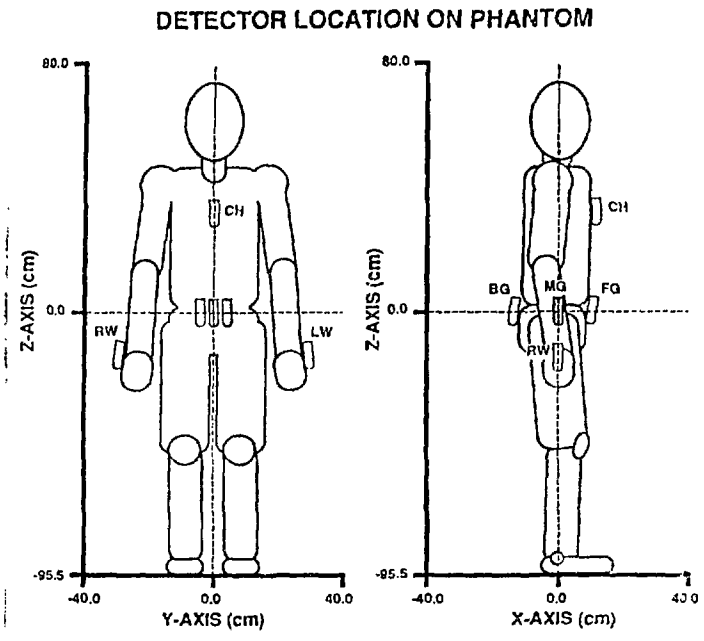

Figure 2. Detector location

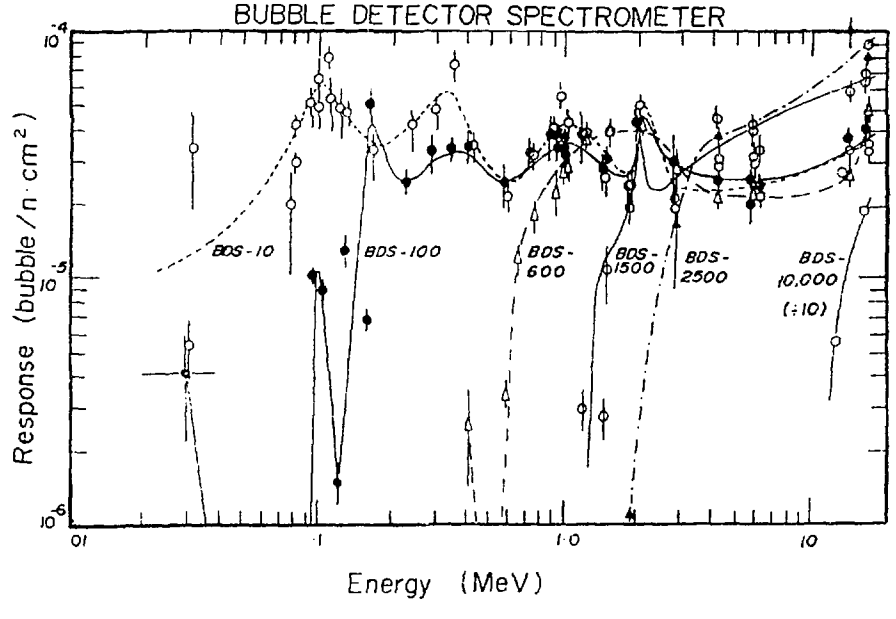

Figure 3. Spectroscopic energy response of Bubble Detector Spectrometer set (courtesy of Bubble Technology Inc.)

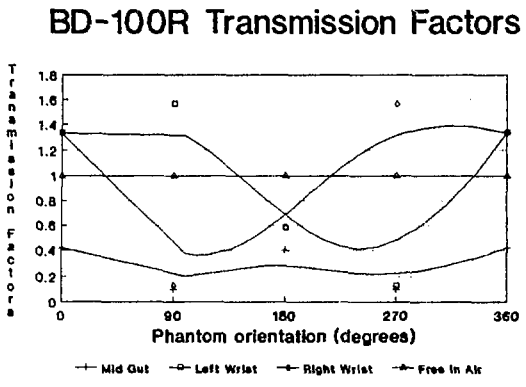

Figure 4. Wrists transmission factors

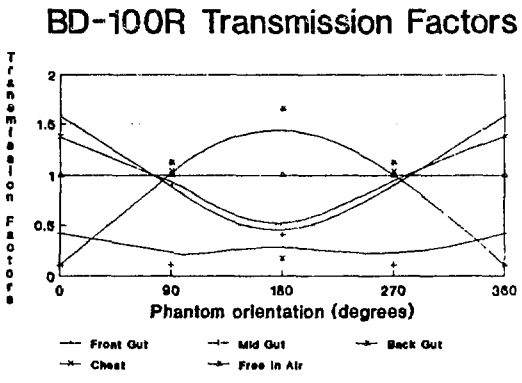

Figure 5. Gut transmission factors

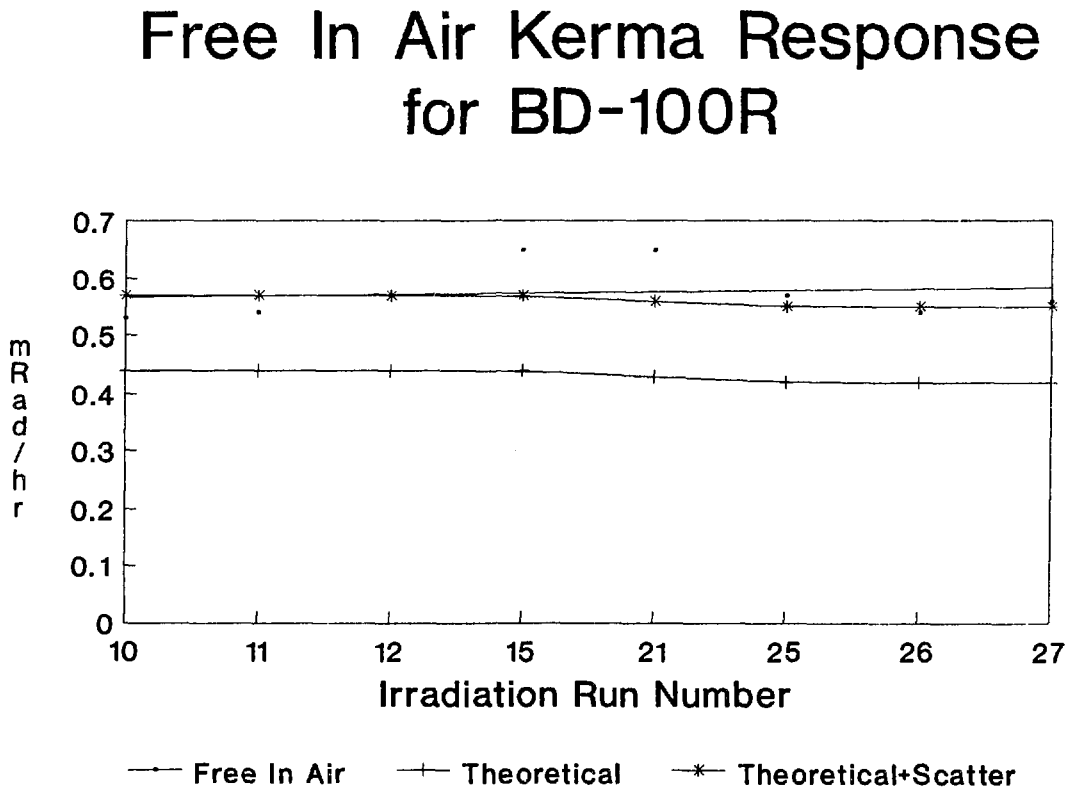

Figure 6. Mid Line Free In Air Kerma

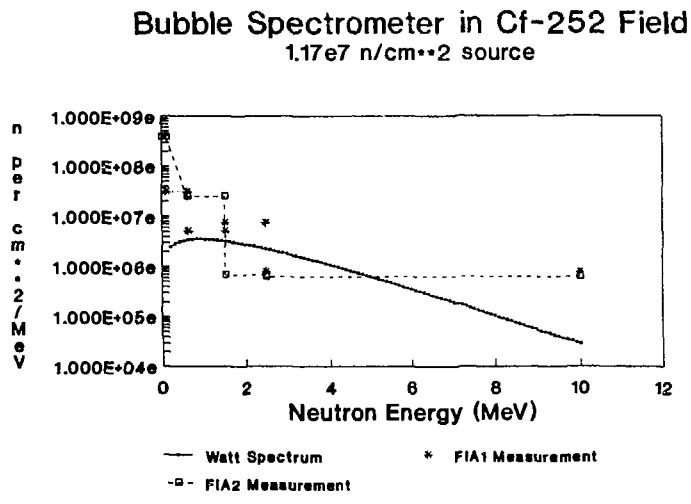

Figure 7. BDS Free In Air kerma

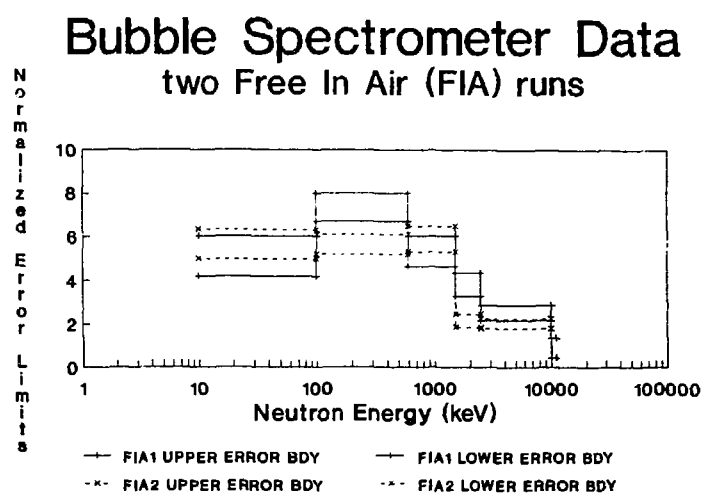

Figure 8. FIA error boundaries

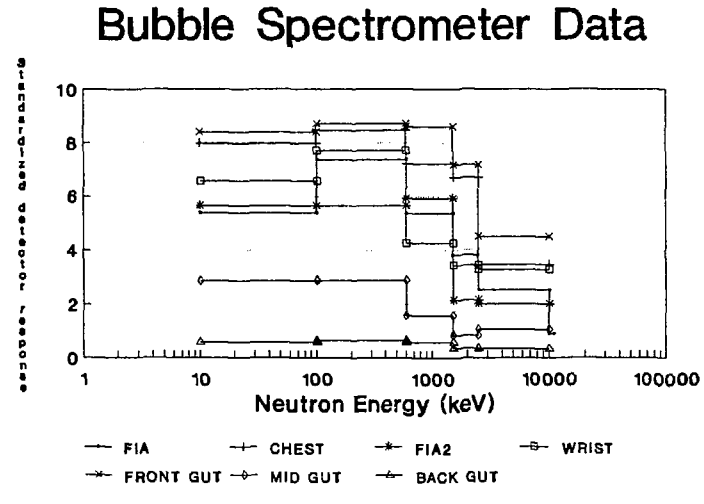

Figure 9. BDS spectrometer data

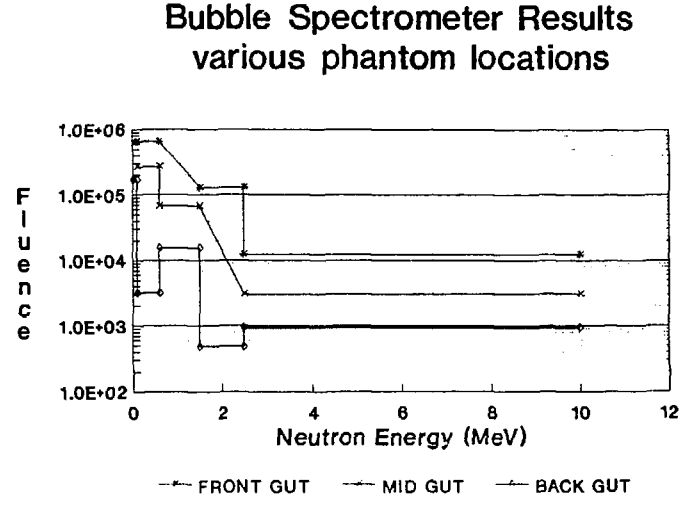

Figure 10. Phantom gut location

9. LITERATURE CITATION

1. National Defence Headquarters Letter 1150-2 (DNRS) dated 22 Dec 1988

2. Commission of the European Communities: Fourth Symposium on Neutron Dosimetry. Munich-Neuherberg (1981)

3. Kaul, D.C.: External Dosimetry, Phantoms, and Dose Equivalence. Radiation Protection and Shielding. (1988)

4. Brodsky, A.. ed.: CRC Handbook of Radiation Measurement and Protection (Vol. 1). CRC Press (1985)

5. Kaul, D., Egbert, S., Roberts, J. and Badham, V.: Radiation Disimetry in and on Anthropomorphic Phantoms, a Comparison of Calculations and Measurements. Science Applications International Corporation, San Diego Cal. (1987)

6. Apfel, R.E.: The Superheat Drop Detector in Neutron Dosimetry. Seventh International Congress of Radiation Research. Amsterdam (1983)

7. Ing, H. and Birnboim H.C.: A Bubble Damage Polymer Detector for Neutrons. Nuclear Tracks and Radiation (Vol. 8, p. 285) (1984)

8. Ing, H.: Bubble Damage Polymer Detectors for Neutron Dosimetry. Fifth Symposium on Neutron Dosimetry. Neuherberg, Germany (1984)

9. Ing, H.: Bubble Detector - An Update on its Development. NATO RSG5 meeting, Norwegian Defence Research Establishment, Kseller, Norway (1988)

10. Ing, H., and Piesch, E.: Status of Neutron Dosimetry. Radiation Protection Dosimetry (1985)

11. Ing. H., and Tremblay, K.: To Develop a Set of Variable Lower-Energy Threshold Bubble Neutron Detectors for Use as a Spectrometer. DREO contract W7714-7-5263/01-SV (1988)

12. Attix, F., and Roesch, W., ed.: Radiation Dosimetry (2nd ed., Vol. 1). Academic Press, New York (1966)

A Real-Time Simulator for the SLOWPOKE-2

Lieutenant-Commander G.P. Cottingham
Department of Chemistry and Chemical Engineering
Royal Military College of Canada

An interactive real-time simulator of the SLOWPOKE-2 was developed for training and teaching use. The simulator accurately models the behaviour of the reactor during normal operation and transients.

Introduction

The SLOWPOKE-2 LEU Fuelled Reactor

SLOWPOKE is an acronym for Safe, LOW POwer c(K)ritical Experiment. It is a 20 kW(thermal) pool-type research reactor characterized by total inherent safety due to a negative temperature coefficient of reactivity and a restricted excess reactivity. The reactor at RMC is fuelled with low enriched uranium (LEU) oxide fuel (20% ^{235}U). The main uses in research, teaching and training are neutron activation analysis and neutron irradiation studies, and a facility for neutron radiography is currently under construction.

The reactor consists of a cylindrical aluminium reactor container suspended in a six metre deep pool of water (Figure 1). At the bottom of the container is the core, composed of 198 fuel pins, in the form of uranium dioxide pellets sheathed in zirconium alloy, assembled in a cage (Figure 2). Cooling within the reactor container and in the pool is entirely by natural circulation.

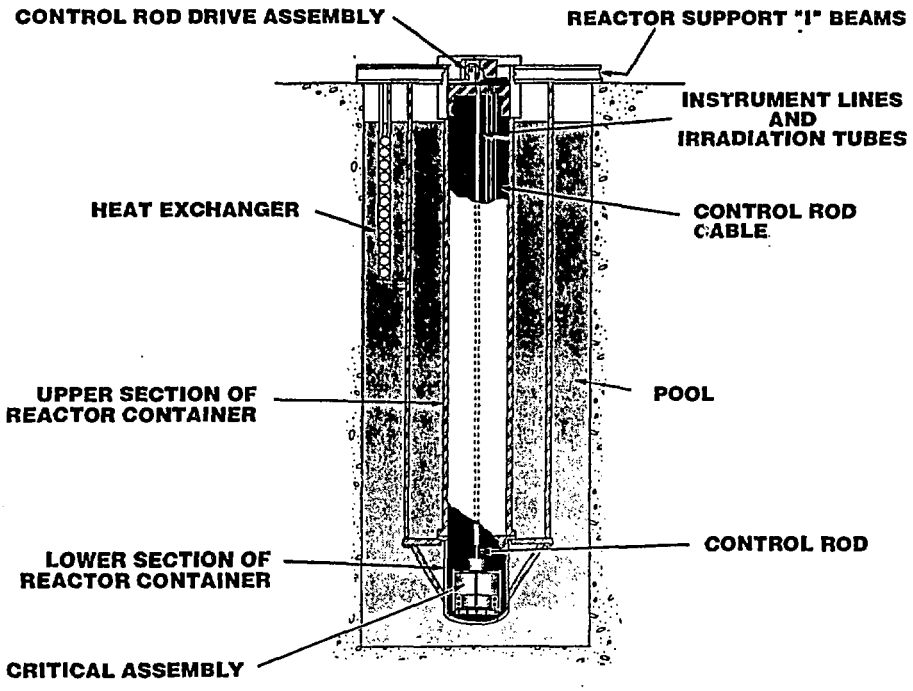

Figure 1. View Through Reactor Pool

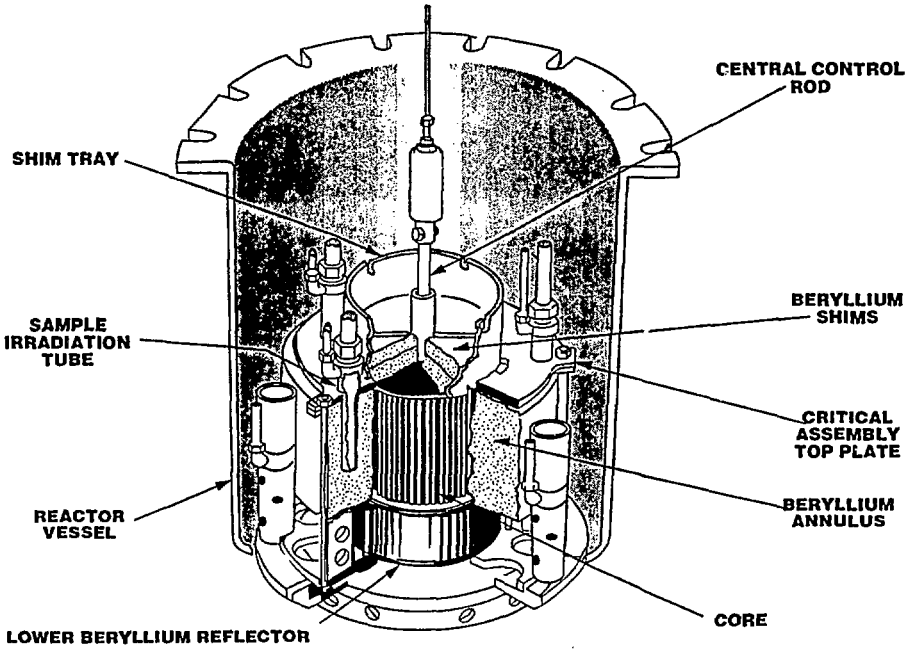

Figure 2. Reactor Vessel and Critical Assembly

Reactor power is controlled using a cadmium-filled control rod suspended in the centre of the core. The position of the rod is varied by means of an electric stepping motor driven through a simple proportional control circuit.

The Simulator

The simulation was undertaken on a Macintosh IIx microcomputer using LabVIEW® software. The control panel and output information are displayed on a 19" colour monitor (Figure 3). LabVIEW® is a data-acquisition application which uses a graphical programming language "G". It has built-in facilities to produce the front panel controls and graphics used in the simulation, thus reducing the programming required. The simulation runs in real time and is interactive; that is, the "trainee" has control of the reactor at all times and can initiate power changes at will. Operator input consists of "pushing buttons" or

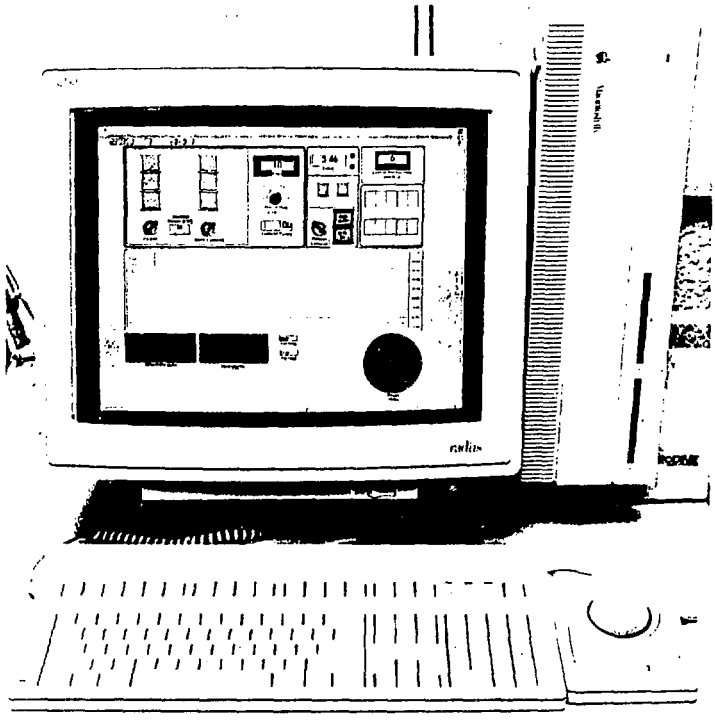

Figure 3. Simulator Showing Control Panel

"turning keys" on the front panel by clicking them with the mouse. The panel displayed includes all the reactor controls and the strip chart monitoring the core inlet and outlet temperatures. To increase "trainee" understanding, extra displays on the simulator are included-- a power meter, a flow meter, a reactivity meter and a digital display of the fuel surface temperature.

Method

Reactor Kinetic Equations

The reactor was modelled as a point source with the delayed neutrons represented as a one-group model. The relevant kinetic data were obtained from AECL (2). The governing equations for the neutron kinetics are the coupled equations describing the time-dependent concentration of neutrons and precursors. (*Note: All symbols and terminology used are defined in Appendix 1.*)

$$\begin{aligned} \frac{dN}{dt} &= \frac{\beta - \rho}{l^*} N(t) + \bar{\lambda} C(t) \\ \frac{dC}{dt} &= \frac{\beta}{l^*} N(t) - \bar{\lambda} C(t) \end{aligned} \qquad (1)$$

These equations were solved using a state variable method with a time step of 0.211 seconds. The time step was chosen to result in a simulation running in real time. This was accomplished with 10 minutes of simulator time taking 9 minutes and 58 seconds of real time.

Temperature-Reactivity Effects

The reactivity is strongly dependent on the temperatures of the coolant and the fuel. An increase in coolant temperature causes a decrease in density with consequent decrease in moderation. A greater leakage of neutrons from the core thus occurs leading to a drop in reactivity.

Heat Transfer

The natural circulation cooling in the core results in flow and heat transfer being interdependent. An increase in power causes the core fuel elements to increase in temperature. Heat is then transferred to the water in the core which decreases in density and rises, thus inducing flow. Heat is lost through the container walls to the water in the pool. Heat is lost from the pool to a heat exchanger, to the ground through the pool walls , and to the air above the pool.

The reactor heat transfer was modelled in three zones: the core, the reactor container and the pool. A heat balance was conducted to determine temperatures throughout the circulation path.

The water in the core was represented as:

$$m_c\, c \frac{dT_c}{dt} = Q_c - \dot{m}\, c\,(T_o - T_i) \qquad (2)$$

The change in the heat energy in the water flowing through the core is equal to the heat produced by the fuel minus the heat energy required to warm the water. The water in the reactor container was represented as:

$$m_a\, c \frac{dT_a}{dt} = \dot{m}\, c\,(T_o - T_a) - UA\,(T_c - T_p)$$

and the inlet temperature to the core was assumed to be the temperature in the reactor container, so the equation can be re-written:

$$m_a\, c \frac{dT_i}{dt} = \dot{m}\, c\,(T_o - T_i) - UA\,(T_c - T_p) \qquad (3)$$

where the loss of heat to the pool is introduced. Because the heat transfer coefficient and area are changing constantly with conditions, they are left "lumped" as the UA term.

In the pool:

$$m_p\, c \frac{dT_p}{dt} = UA\,(T_c - T_p) - Q_p \qquad (4)$$

The core temperature was considered to be:

$$T_c = \frac{T_o - T_i}{2} \qquad (5)$$

Equations (2), (3) and (4) were solved using a first order Euler method with a time step of 0.211 seconds.

Natural Circulation Flow

An empirical relation for the flow in the reactor as a function of the density difference between the outlet temperature and the inlet temperature was developed based on measurements done on a full scale model.

$$\dot{m} = 29.716 - 29.677 \left(\frac{d_{outlet}}{d_{inlet}}\right) \qquad (6)$$

Fuel Temperature

The surface fuel temperature was calculated using a linear fit obtained from AECL data (1).

$$T_f = 18.181 + 47.968\, log\,(Q_c) \qquad (7)$$

Temperature-Reactivity Effects

Preliminary predictions of the correlations relating temperature and reactivity for the LEU fuelled reactor by AECL are not identical to that measured for the reactor at RMC (3) and subsequent investigations have failed to yield conclusive correlations (5). This situation led to the adoption of empirical linear re-

lationships to describe the relationship between reactivity and core temperature and fuel surface temperature.

$$\Delta\rho_c = 1.7225 + 9.741 \times 10^{-2} T_c - 1.4494 \times 10^{-3} T_c^2 \qquad (8)$$

$$\Delta\rho_f = 0.15406 - 8.8302 \times 10^{-3} T_f \qquad (9)$$

These relationships have been modified in an attempt to reproduce measured data. Difficulty in separating the interacting effects is considered to be the greatest potential source of error in the model. Further research is required to quantify these relationships.

Control System

The control system drives the rod in or out of the core at a speed of 10.6 mm/s based on the error between set and measured flux. The rod movement was easily modelled and the worth of the rod was obtained from the control rod calibration curve for the reactor (3). A fifth order polynomial representing this curve, with R being the distance in inches the rod is withdrawn from the core, is:

$$\rho_{rod} = 3.4869 \times 10^{-3} + 0.95119\, R + 4.9074 \times 10^{-2} R^2 - 8.3251 \times 10^{-3} R^3 - 1.6732 \times 10^{-3} R^4 + 1.7416 \times 10^{-4} R^5 \qquad (10)$$

Total System Algorithm

A block diagram showing the overall simulation scheme is shown in Figure 4.

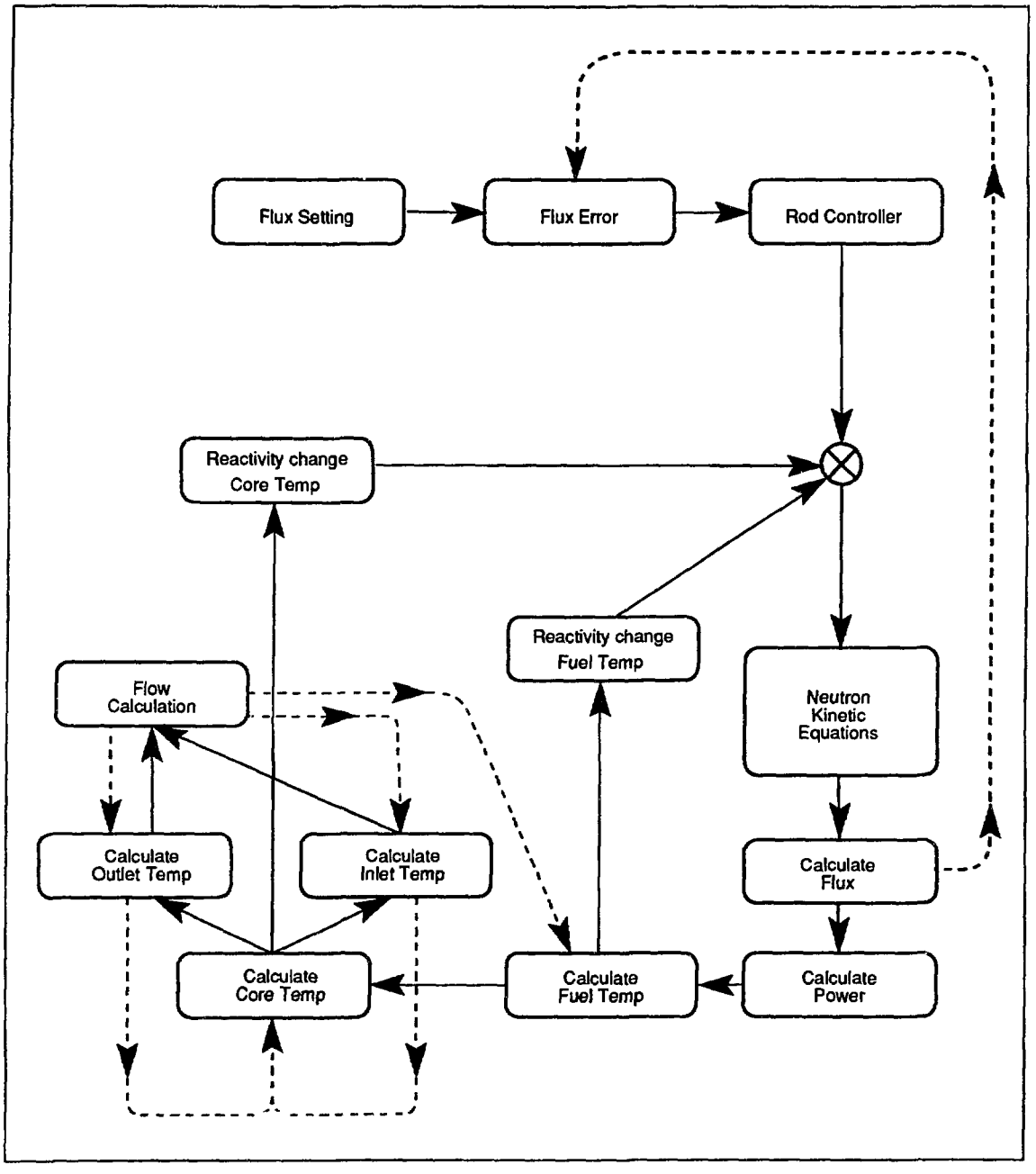

Figure 4. Total System Algorithm

Results

Routine Operation

The simulator accurately reproduces the measured performance of the reactor during normal operation for periods of up to one hour. No consideration has yet been made for fission product poisoning which will affect longer duration simulations.

Transient Simulations

The two most extreme conditions which have been experienced by the SLOWPOKE-2 reactor at RMC were the 3 mk and 4 mk transients performed during commissioning as normal tests. In these tests, an initial fixed reactivity

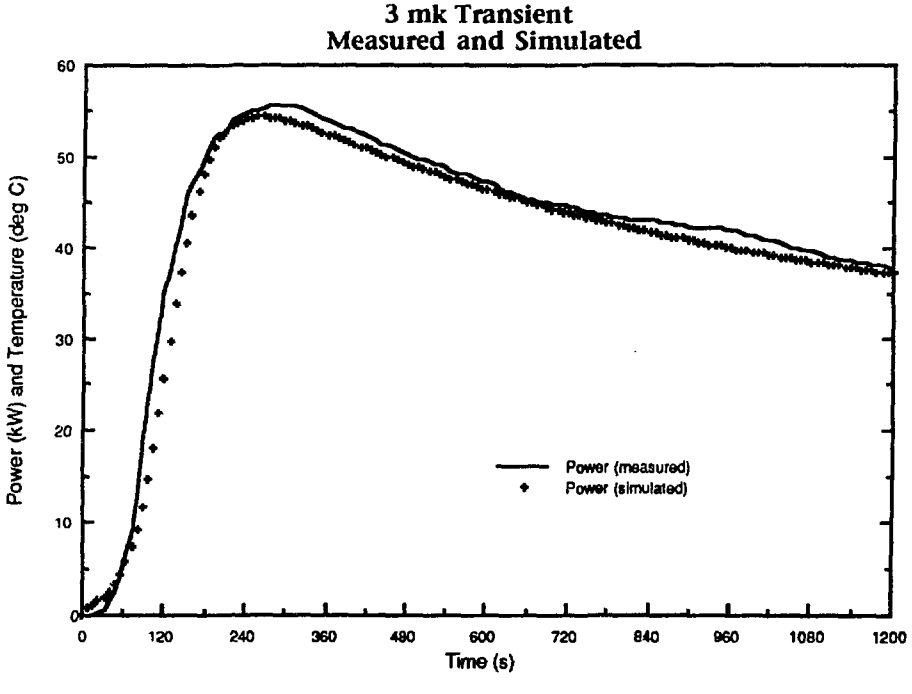

Figure 5. 3 mk Transient

was established and the reactor was allowed to proceed without any external control actions. These conditions have been simulated and a comparison between the measured and simulated results for a 3 mk transient is shown in Figure 5. . Further comparisons are planned for 1 mk and 2 mk transients. Predictive trials will then be done for 5 and 6 mk transients.

Conclusions

A successful simulator has been constructed which can model normal operating conditions and transients accurately. The operator is permitted to perform control operations while observing the results in real time. As a result, the simulator has proven to be a valid training and teaching tool.

Recommendations

1. The model should be developed further to introduce "supervisor initiated" malfunctions to increase the training value.

2. Fission product poisoning should be considered and an algorithm for Xenon generation should be introduced.

3. An interface board should be added which would permit the simulator to interact with the reactor directly. Consequently, the extra instruments generated with the LabVIEW® software would be able to act on live data from the reactor sensors and display additional, useful information to the operator.

References

1. Wise, M.E. , Kay, R.E. 1983 : Description and Safety Analysis for the SLOWPOKE-2 Reactor CPR-26 Rev 1 , Atomic Energy of Canada Limited Radiochemical Company.

2. Smith, A.D., Townes B.M. 1985 : Description and Safety Analysis for the SLOWPOKE-2 Reactor with LEU Oxide Fuel CPR-77 , Atomic Energy of Canada Limited, Radiochemical Company.

3. Burbidge, G.A., Jones, R.T., Townes, B.M. 1986 : Commissioning of the SLOWPOKE-2 (RMC) Reactor , Atomic Energy of Canada Limited, Radiochemical Company.

4. Kay, R.E., Hilborn, J.W., Poulsen, N.B. 1976 : The Self-Limiting Power Excursion Behaviour of the SLOWPOKE Reactor - Results of Experiments and Qualitative Explanation , Atomic Energy of Canada Limited, Radiochemical Company.

5. Lt(N) de Wit, R.T. 1989 : Reactivity Calculations for the Low Enrichment Uranium Fuelled SLOWPOKE-2 Reactor at the Royal Military College of Canada . MEng Thesis, Deptartment of Chemistry and Chemical Engineering, Royal Military College of Canada.

6. Lt(N) Duchesne, J.C.D 1990 : Determination of Thermal Output From the SLOWPOKE-2 Reactor at RMC Draft MEng Thesis, Deptartment of Chemistry and Chemical Engineering, Royal Military College of Canada.

Appendix 1

Symbols and Terminology Used

The following symbols and abbreviations were used in the paper:

$N(t)$	Concentration of thermal neutrons at time t.
$C(t)$	Concentration of precursor elements at time t.
β	percentage of neutrons which are delayed (1 group model)
ρ	"reactivity" usually expressed in "milli-k", defined as $\frac{k-1}{k}$ where k is the effective multiplication factor
l^*	the prompt neutron lifetime (s)
$\bar{\lambda}$	the average precursor decay constant (s^{-1})
m_c	the mass of water in the core (kg)
m_a	the mass of water in the reactor container (kg)
m_p	the mass of water in the pool (kg)
c	the specific heat of water $\left(\frac{J}{kg \bullet K}\right)$
T_c	the temperature of water in the core $(°C)$
T_i	the temperature of water entering the core $(°C)$
T_o	the temperature of water leaving the core $(°C)$
Q_c	the heat generated in the core (W)
Q_p	the total heat losses from the pool (W)
$\dot{m}$	the flow rate in the core $\left(\frac{kg}{s}\right)$
U	the overall heat transfer coefficient $\left(\frac{W}{m^2 \bullet K}\right)$

A	the area of heat transfer surface $\left(m^2\right)$
d_{outlet}	the density of the outlet stream $\left(\frac{kg}{m^3}\right)$
d_{inlet}	the density of the inlet stream $\left(\frac{kg}{m^3}\right)$
R	the distance control rod withdrawn from the core (in)

MODELLING OF SINGLE PHASE NATURAL CIRCULATION FOR THE MAPLE - MNR REACTOR

Glenn Harvel
Dept. Eng. Physics, McMaster University
Hamilton, Ontario, Canada L8S 4M1

Preliminary thermalhydraulic studies have been performed to suggest the feasability of using the McMaster Nuclear Reactor's (MNR) existing primary heat transport loop with a MAPLE type core. The present study evaluates the single phase natural circulation behaviour of the MAPLE - MNR with an analytical model. The developed code (NATCIR) was used to evaluate the performance of a check valve in the flow bypass loop. The results show that the check valve does not seem to provide any influence on the single phase natural circulation cooling mode of the reactor core. NATCIR also successfully determined a natural circulation mass flow rate as a function of decay heat level of the reactor core.

Introduction

The proposal for upgrading the MNR reactor with a MAPLE core allows for higher neutron fluxes and better neutron economy. As a result, the MAPLE core also has a relatively high heat flux. An important consideration for the MAPLE - MNR upgrade, is whether the existing primary heat transport system is capable of cooling the new MAPLE core. Preliminary thermalhydraulic studies suggest the existing cooling system is adequate for normal operating conditions.[1,2,3]

However, no comprehensive study has been conducted for natural circulation cooling mode to remove decay heat from the MAPLE - MNR core.[2,3] In this study, a one dimensional analytical model denoted NATCIR is developed to model the natural circulation of the MAPLE - MNR reactor under loss of pump power conditions.

MAPLE - MNR

The MNR reactor is a 5 MW pool type reactor. The upgrade from the MNR to the MAPLE reactor could be easily accomplished by replacing the MNR core with a MAPLE core with few modifications to the primary heat transport loop. The thermalhydraulics flow loop is shown in figures 1(a) and 1(b).

Figure 1(a) represents the existing MNR thermalhydraulics loop.[1,2,3] Only the core and piping in and out of the pool will need to be changed. Figure 1(b) depicts the proposed MAPLE

core.[1,2,3] A fundamental difference between the MAPLE and MNR cores is the direction of flow through the core itself. The MAPLE core is vertically up flow as opposed to the MNR. To suppress short lived radioisotopes from the core reaching the pool surface and yet still allow for online maintenance and refuelling of the core, a special chimney arrangement has been used. The core jet flow is pumped from the sides of the chimney to the heat exchangers and a 10% bypass flow is used to circulate the pool and suppress the core jet in the chimney.

Figure 1.

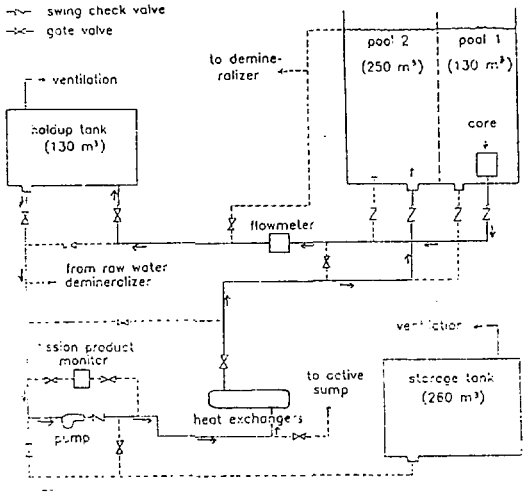

(a)
MNR Thermalhydraulics Loop
[3]

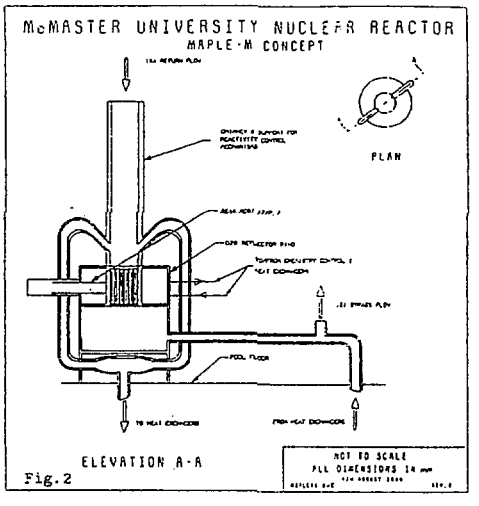

(b)
MAPLE-MNR Thermalhydraulics Loop
[3]

The MAPLE core design is shown in figure 2. The core has an array of hexagonal flow channels with three shutdown and three control sites. The fuel is primarily a hexagonal bundle of Uranium - Silicon - Aluminium mixture with cooling fins for each fuel pin. The complex structure of the MAPLE core channel leads to a complex pressure drop across the core.

When determining the flow path for natural circulation, the flow path is assumed to remain in the pool as the head loss to the pump and heat exchangers is much larger in the proposed MAPLE - MNR design. This suggests the bypass channel and the check valve are very important for the natural circulation model. Figure 3 illustrates the location of the bypass channel and check valve in the pool.[1,2]

Figure 2.

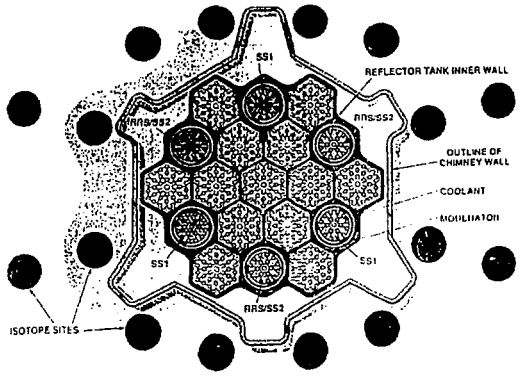

Top View of MAPLE-MNR Core [3]

Figure 3.

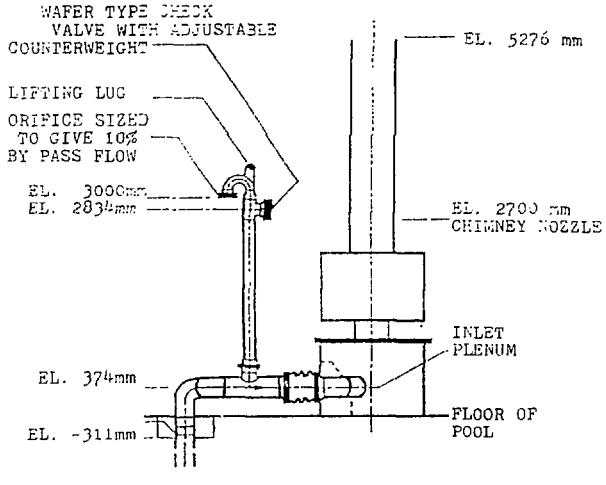

Primary Coolant Inlet Piping [3]

NATCIR assumes the fluid remains in the single phase and models the steady state condition after a pump trip. NATCIR does determine whether the flow is laminar or turbulent and adjusts the friction losses accordingly.

Development of NATCIR model

Natural circulation in the MAPLE - MNR reactor can be modelled by examining the steady state momentum equation as has

been conducted for other nuclear power plants[4] as shown below;

$$\frac{\partial P}{\partial s} = -\rho g \cdot \hat{e}_s - F_s \qquad (1.1)$$

,where P is the pressure, ρ the fluid density, g the acceleration due to gravity, $\hat{e}_s$ is the unit vector in the direction of flow and F_s are the friction forces.

By integrating around the flow loop, the pressure term must vanish as it is a closed loop. By applying the continuity equation in terms of the mass flow rate W, equation 1.1 becomes;

$$\hat{e}_s \cdot g \oint \rho \, dz = \frac{W^2}{2} \int \frac{f \, ds}{D(s)\rho(s)A^2(s)} \qquad (1.2)$$

,where the left hand side of the equation represents the thermal bouyancy term and the right hand side the frictional loss terms.

The flow path for the MAPLE - MNR reactor is shown in figure 4 with the assumptions that the head loss to the holding tank and the pump are much greater than all other frictional losses. As such, both the thermal bouyancy and frictional loss terms can be segmented into the various pool and reactor components.

Figure 4

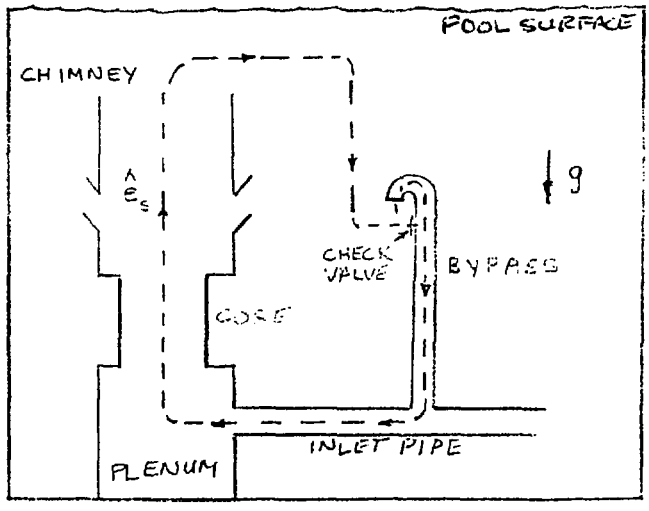

Flow Path of Natural Circulation
in the MAPLE - MNR Reactor

THE THERMAL BOUYANCY TERM

The fluid density is assumed to be a linear dependence upon temperature and the Boussinesq approximation [4] is used.

$$\rho = \rho_c \{ 1 - B (T - T_c) \} \quad (1.3)$$

,where ρ_c and T_c are the cool fluid density and temperature respectively.

The temperature profile for the loop is assumed to increase across the core and heat is lost along the chimney. Any fluid reaching the pool is assumed to be quenched to the cool fluid temperature. Thus the pool, plenum and bypass piping temperature is T_c and the fluid density is thus $_c$.

In examining the core, the energy equation becomes,

$$Cp\ W \frac{\partial T}{\partial s} = q \quad (1.4)$$

,where the heat flux to the fluid is assumed to behave in a cosine manner.[5]

$$q = Q \cos (G (z - L_c/2)) \quad (1.5)$$

Hence, the temperature profile becomes,

$$T - T_c = \frac{Q}{CpWG} [\sin (G (z - L_c/2)) + 1] \quad (1.6)$$

,where $\Delta T_{core} = T_h - T_c = 2Q/CpWG$ (1.6b)

The chimney is assumed to provide convective heat cooling of the fluid. Similarly, the energy equation is as follows:

$$Cp\ W \frac{\partial T}{\partial s} = - h\ PI\ D_{ch} (T - T_c) \quad (1.7)$$

Integrating along the chimney, the temperature profile becomes,

$$T - T_c = T_{core} \exp [- s/DC] \quad (1.8)$$

,where $DC = Cp\ W / h\ PI\ D_{ch}$

Placing the temperature profiles into the gravity terms for each section yields the following net gravity term.

$$\hat{e}_s \cdot \int g\rho\, ds = g\rho_c B\Delta T_{core} [L_c/2 - DC \exp[-L_c/DC] [\exp[-L_{ch}/DC - 1] \quad (1.9)$$

FRICTIONAL LOSS TERMS

The frictional loss terms can be seperated into major and minor loss components, as in equation 1.10.

$$\frac{W^2}{2}\int \frac{f\ ds}{D(s)\rho(s)A^2(s)} = \frac{W^2}{2}\left(\frac{fL}{A^2 d 2\rho_c} + \frac{k}{A^2\rho_c}\right) \qquad (1.10)$$

The friction factor depends upon whether the flow is laminar or turbulent. In the laminar region, the friction factor is assumed to depend upon the Reynolds number according to equation 1.11. In turbulent flow, we assumed that the friction factor can be approximated by the Blassius correlation of equation 1.12.[6]

$$f = 16/Re \qquad (1.11)$$

$$f = 0.0791/Re^{1/4} \qquad (1.12)$$

Ten minor losses were identified in the MAPLE - MNR natural circulation flow loop. All of the minor loss coefficients are presented in table 1.1.

Table 1.1 Minor Losses in the MAPLE - MNR Natural Circulation Flow Loop

Minor Loss	k Factor	Area (m^2)
Chimney Exit	1.0	0.154
Plenum Entrance	0.5	2.138
45° Pipe Bend	0.147	5.566E-02
Tee of Pipe	0.196	3.581E-02
180° Bypass	0.591	3.581E-02
Bypass Exit	0.490	3.581E-02
Check Valve	0.7	3.581E-02
Core Entrance	0.42	2.769E-03
Core Exit	0.87	2.769E-03
Tee of Check Valve	0.84	3.581E-02

By equating equations 1.9 and 1.10, we can solve for the decay heat level of the core T_{core}.

$$\Delta T_{core} = \frac{[W^2/2(\ fL/A^2 d 2\rho_c + k/A^2\rho_c\ )]}{g\rho_c\ B[L_c/2 + DC\ \exp[-L_c/DC][\exp[-L_{ch}/DC-1]]]} \qquad (1.13)$$

Equation 1.13 isolates the need to use any iterative model or even consider the dependence upon the power generation in the core. To relate the power generation to the decay heat level, equation 1.6b can be rearranged as follows.

$$Q = Cp\ G\ W\ T_{core} / 2 \qquad (1.14)$$

With equations 1.13 and 1.14 we can model the natural circulation of the MAPLE - MNR based upon the decay heat level or the power generation of the core.

Numerical Results

Figure 5 represents the mass flow rate dependence upon the decay heat level for the case with and without a check valve on the flow bypass loop. From first glance, there is no discernable influence of the check valve upon flow conditions. This may suggests that the check valve is not required in the MAPLE - MNR design. The sudden shift in the profile is a laminar to turbulent transition of the core. NATCIR presently does not have a smooth correlation for the friction factor as the flow passes from laminar to turbulent.

Figure 5.

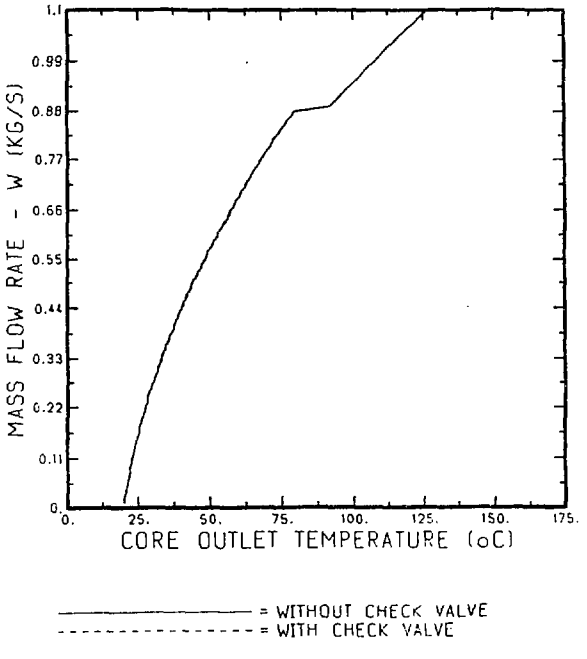

NATURAL CIRCULATION FLOW RATE
FOR THE MAPLE-MNR REACTOR WITH
AND WITHOUT CHECK VALVE

In this case, the cool fluid temperature is set to 20.0°C. From figure 5, we can see the laminar turbulent transition of the core occurs at a mass flow rate of 0.88 kg/s and approximately 75°C. The onset of nucleate boiling (ONB) occurs in the MAPLE-MNR design at approximately 121°C.[8]

Figure 6 represents the effect of inclusion of the minor losses in NATCIR. Obviously, the decay heat level needed for a given flow rate to occur is drastically reduced. This is a reasonable behaviour as the flow resistance is reduced when the minor losses are neglected. From the magnitude of the difference, the minor losses cannot be ignored for natural

circulation modelling.

Figure 6.

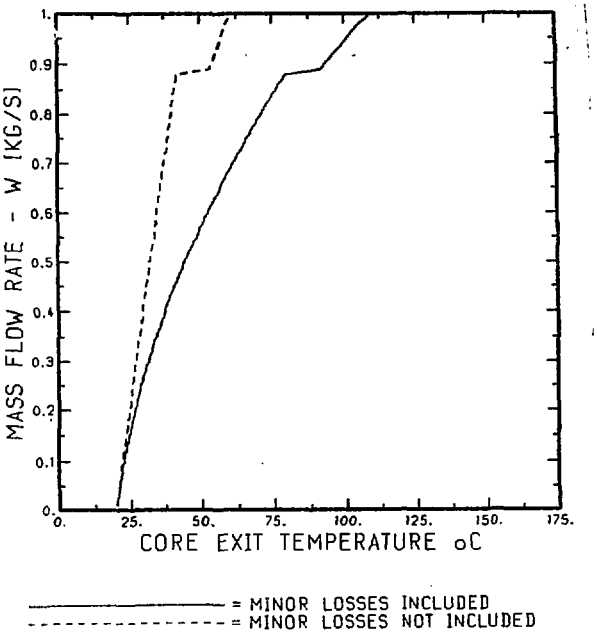

EFFECT OF THE MINOR LOSSES UPON THE NATURAL CIRCULATION OF THE MAPLE - MNR REACTOR

Figure 7.

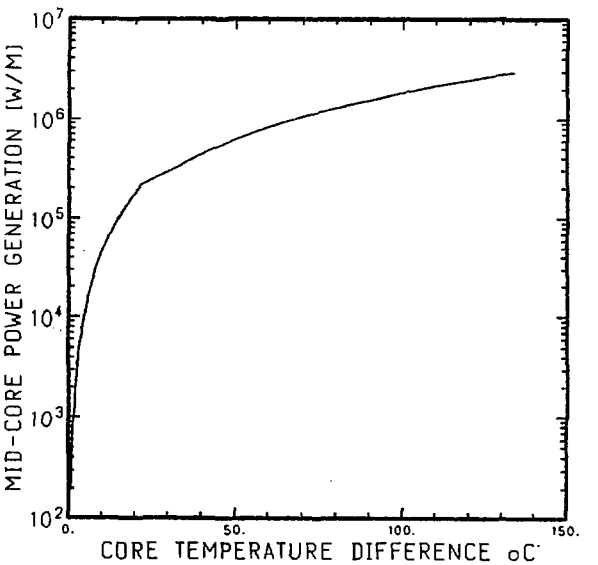

RELATION OF CORE TEMPERATURE DIFFERENCE TO POWER GENERATION IN THE MAPLE-MNR REACTOR

The relationship between the decay heat level and the peak power generation is depicted in figure 7. Knowing that 100% power relates to 1.20E08 W/m[8], we can determine that a decay

heat level of 100°C is at 1.3% of full power.

Concluding Remarks

NATCIR is capable of modelling the MAPLE - MNR reactor for single phase natural circulation cooling mode. As such, four main conclusions were developed from this study.

1.- The check valve has no influence on the single phase natural circulation of the core and may not required in the MAPLE-MNR design.

2. - The minor losses must be included in the design to ensure accurate modelling of the frictional losses.

3. - NATCIR requires a smoother correlation for the transition from laminar to turbulent flow in the core.

4. - A two phase model needs to be developed to model the transition from forced to natural convection of the MAPLE-MNR reactor.

Acknowledgements

The author wishes to acknowledge the support of J.S. Chang for his comments and suggestions. This work is supported by the Natural Sciences and Engineering Research Council of Canada.

Nomenclature

P - Pressure [Pa]
ρ - Fluid density at temperature T [Kg/m^3]
ρ_c - Cool fluid density [Kg/m^3]
g - Acceleration due to gravity [m/s^2]
e_s - Unit vector along flow path
s - Distance along flow path [m]
F_s - Friction forces
W - Mass flow rate [Kg/s]
f - Friction factor
D - Diameter of flow channel [m]
A - Cross sectional area of flow channel [m^2]
B - Volumetric coefficient of expansion [$°C^{-1}$]
T - Temperature of fluid at location s [°C]
T_c - Cool fluid temperature [°C]
Cp - Specific Heat Capacity of Water [J/Kg-°C]
q - Linear heat generation [W/m]
Q - Maximum linear heat generation [W/m]
G - Constant defining heat flux profile [m^{-1}]
L_c - Length of Core [m]
L_{ch} - Length of chimney [m]
h - Heat transfer coefficient in chimney [W/m^2-°C]
PI - 3.1415

k - Minor Loss Coefficient
Re - Reynolds Number

References

1. M.F.Collins, J.S. Chang, M. Shoukri, W.J. Garland, P.C. Ernst, R.J.Wilson, and M. Kiela,"MAPLE NUCLEAR REACTOR Engineering Feasability Study", McMaster University,1988.

2. J.S. Chang and H.E. Rummens,"Engineering Feasability Studies of the McMaster - MAPLE Reactor: Recommendations for Thermalhydraulic Safety Studies",McMaster university,1988.

3. J.S. Chang, P.C. Ernst, W.J. Garland, H.E. Rummens, M. Shoukri, R.J. Wilson, D.K. Baxter, G.E. Gillespie, P.J. Mills and S.Y. Shim,"MAPLE - MNR: Preliminary Thermalhydraulic Studies",Proceedings 10th Annual Canadian Nuclear Soc., P.J. Fehrenbach Ed.,CNS Press,Toronto Vol.3, p10.14-10.20,1989.

4. Y. Zvirin,"A Review of Natural Circulation Loops in PWR and other Systems",EPRI Report NP-1676-sr,January,1981.

5. A. Bejan,"Coonvection Heat Transfer"John Wiley & Sons, New York,1984.

6. J.J. Duderstadt and L.J. Hamilton,"Nuclear Reactor Analysis"John Wiley & Sons, New York,1976.

7. F.M. White,"Fluid Mechanics"2nd Ed.,McGraw Hill,New York, 1986.

8. P.J. Mills,"Thermalhydraulic Specifications for MAPLE - MNR" Sept.,1988.

CRITICAL HEAT FLUX ON HORIZONTAL CYLINDERS IN A CROSS FLOW

by

Nirmala Arifin

Dept. of Chemical Engineering and Applied Chemistry
University of Toronto

23 March 1990

NOMENCLATURE

A_h, A_w : heater surface area

A_j : vapour jet cross-sectional area

D : heater diameter

d : diameter of bubble

Fr : Froude number , $u_\infty / \sqrt{gD}$

G : gravity influence parameter , $u_\infty / \sqrt[4]{g\sigma/\rho_f}$

h_{fg} : latent heat of vaporization

q_{max} , q_{co} : critical heat flux

$q_{co,Z}$: Zuber's critical heat flux for infinite flat plate, eqn (2)

R : radius of heater

R' : dimensionless radius $R/\sqrt{\sigma/g(\rho_f-\rho_g)}$

r : density ratio , ρ_f/ρ_g

St : Strouhal Number

u_j : velocity of vapour relative to approaching velocity

u_∞ : bulk liquid velocity

v_i : volumetric growth rate of vapour bubbles

We_f : liquid Weber number $2R\rho_f u_\infty^2/\sigma$

We_g : vapour Weber number $2R\rho_g u_\infty^2/\sigma$

α : ratio of width of 2-D vapour jet to diameter of cylinder

δ : thickness of vapour blanket

δ_c : critical thickness of liquid film

λ_d : the most susceptible (dangerous) wavelength of Taylor instability

λ_c : Helmholtz critical wavelength

ρ_f , ρ_ℓ : liquid density

ρ_g , ρ_v : vapour density

ε : theoretical volumetric ratio of accompanying liquid to a moving spherical bubble

ϕ : dimensionless peak heat flux, eq.(5)

τ_D, τ : hovering period of bubble, time of bubble break off

σ : surface tension between saturated liquid and its vapour

INTRODUCTION

The process of boiling has been of increasing interest recently because of the necessity to transfer large heat fluxes in devices such as power generators and spacecraft. An important design consideration when equipment is chosen to operate in a boiling environment is termed as the burnout or critical heat flux (CHF). This critical point separates the nucleate and film boiling regions. The film boiling region is generally characterized by extremely high surface temperature. Hence, to be able to accurately predict the critical heat flux will be valuable in insuring efficient and safe design.

This paper attempts to review the recent development in the research on critical heat flux in a cylinder in a horizontal cross flow.

THEORETICAL MODELS OF CRITICAL HEAT FLUX

There are two conflicting theories on the prediction of the critical heat flux. The first theoretical model is the Mechanical Energy Stability Criterion (MESC) proposed by Lienhard and Eichhorn (1). The second one is based on the hydrodynamic instability model suggested by Haramura and Katto (2).

LIENHARD AND EICHHORN'S MESC (MECHANICAL ENERGY STABILITY CRITERION)

In flow boiling, there are two types of structures of escaping vapour. At low liquid velocity, a three dimensional 'jet-like' flow pattern exists. At high velocity, a two dimensional 'sheet-like' flow pattern predominates. The occurence of these flow patterns have been confirmed by Cochran and Andracchio (3), and is shown in Fig 1.

For the 3-D 'jet-like' flow pattern, Lienhard and Eichhorn have postulated that the boiling mechanism is similar to that of pool boiling, and the pool boiling correlation proposed by Sun and Lienhard (4) can be used to predict the critical heat flux in this region. Sun and Lienhard's correlation is later modified by Lienhard and Dhir (5) to fit a more general statement of the hydrodynamic theory to get the expression:

$$\frac{q_{max}}{q_{c.e}} = \begin{cases} 0.94/(R')^{1/4} & \text{for } 0.12 < R' \leq 1.17 \\ 0.904 & \text{for } R' \geq 1.17 \end{cases} \qquad (1)$$

'Jet - like'
Flow Pattern

(a) 0.051-Centimeter-diameter heater; 14.6 centimeters per second.

'Sheet - like'
Flow Pattern

(b) 0.116-Centimeter-diameter heater; 60.4 centimeters per second.

Figure 2. - Water boiling at heat flux just below burnout.

where $q_{c,z}$ is the Zuber's critical heat flux for infinite flat plate:

$$q_{c,z} = \frac{\pi}{24} \rho_g^{1/2} h_{fg} \left[\sigma g (\rho_f - \rho_g) \right]^{1/4} \quad (2)$$

and R' is the dimensionless radius:

$$R' = R / \sqrt{\sigma / g(\rho_f - \rho_g)} \quad (3)$$

For the two dimensional 'sheet-like' flow pattern, the heat flux can be accounted for by the removal of vapour in the configuration shown in Fig 2, such that:

$$q_{max} = \rho_g h_{fg} u_\infty \frac{A_1}{A_h} \left(1 + \frac{u_g}{u_\infty} \right) \quad (4)$$

or

$$\phi = \frac{\pi q_{max}}{\rho_g h_{fg} u_\infty} = \alpha + \alpha \frac{u_g}{u_\infty} \quad (5)$$

Lienhard and Eichhorn use the mechanical energy balance of vapour wake to determine the ratio u_g/u_∞. They postulate that the wake becomes unstable when the vapour carries more mechanical energy into the wake than what can be absorbed in the surface energy of the escaping bubbles. When the critical heat flux occurs,

(rate of change of kinetic energy into control volume) +

(rate of change of surface energy within control volume) = 0

i.e. $\frac{1}{2} \rho_f 2\alpha R u_g^3 - 2 u_\infty \sigma = 0$, or $\frac{u_g}{u_\infty} = \frac{4^{1/3}}{(\alpha We_g)^{1/3}}$ (6)

$$\therefore \phi = \frac{\pi q_{max}}{\rho_g h_{fg} u_\infty} = \alpha + \frac{4^{1/3} \alpha^{2/3}}{We_g^{1/3}} \quad (7)$$

The constant α is determined using Bernoulli and Continuity equations. By assuming potential flow,

$$1 + \frac{4^{1/3}}{(\alpha We_g)^{1/3}} = \frac{\sqrt{3 \rho_f / \rho_g}}{\sqrt{\left[\alpha^2 \left(\frac{K}{5} \right)^2 - 1 \right]}} \quad (8)$$

If α is not influenced by surface tension,

$$\alpha = \text{constant} \; (\rho_f / \rho_g)^{3/4} \quad (9)$$

Equation (8) applies only when the liquid momentum is much greater than the vapour momentum. If this condition is not met, the vapour will flow straight up without allowing the liquid to curve around the back as predicted by potential flow, and α will be close to unity, so

$$\frac{\pi q_{max}}{\rho_g h_{fg} u_\infty} = 1 + \left(\frac{4}{We_g} \right)^{1/3} \quad (10)$$

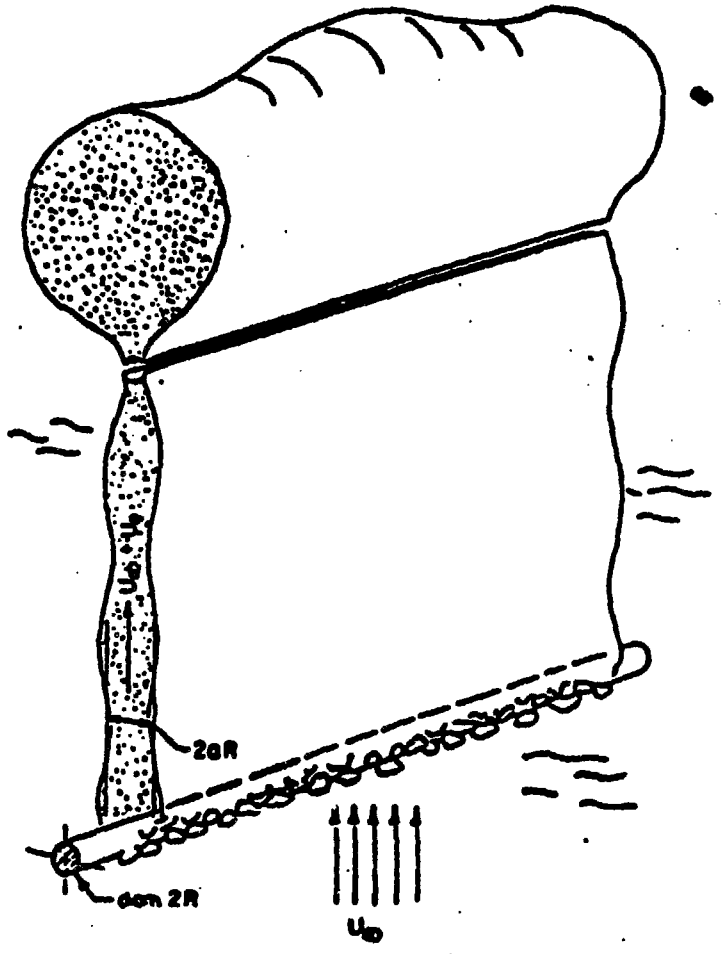

FIG. 2. Vapor removal by the action of two-dimensional jets before burnout occurs.

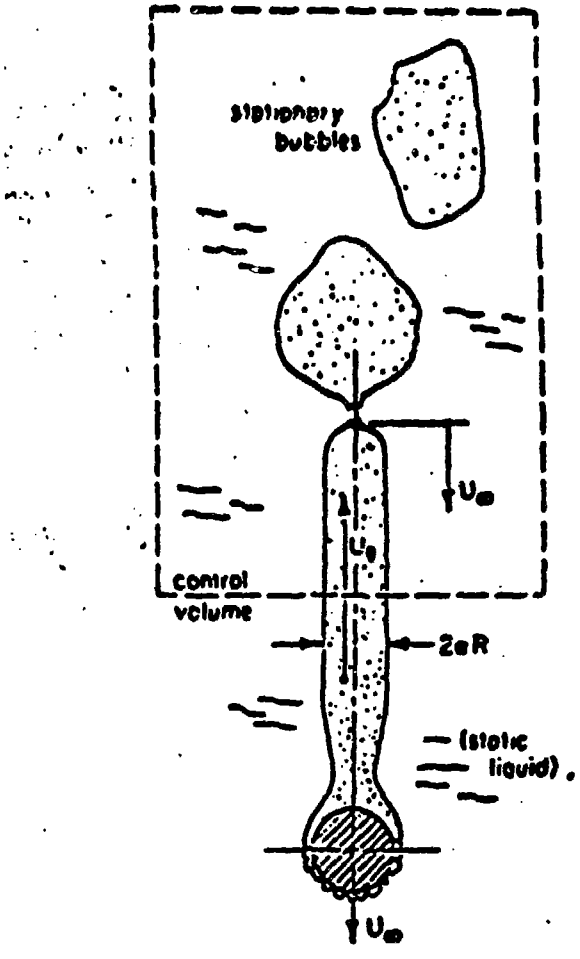

FIG. 3. Control volume for kinetic/surface energy balance.

For high velocity, constant = 1/169 in eqn (9), therefore

$$K = (\rho_f/\rho_g)^{3/4}/169 \qquad (11)$$

and

$$\frac{\pi\, q_{max}}{\rho_g\, h_{fg}\, U_\infty} = \frac{1}{169}\left(\frac{\rho_f}{\rho_g}\right)^{3/4} = \frac{1}{19.2}\left(\frac{\rho_f}{\rho_g}\right)^{1/2}\frac{1}{We_g^{1/2}} \qquad (12)$$

Lienhard and Eichhorn also found that the transition from 'jet-like' flow to 'sheet-like' flow occurs when:

$$We_g = 4\,(\rho_f/\rho_g)\,R' \qquad (13)$$

and transition from 'sheet-like' flow to high velocity equation (eq.12) occurs when :

$$\frac{\pi\, q_{max}}{\rho_f\, h_{fg}\, U_\infty} = 1 + 0.215\sqrt{\rho_f/\rho_g} \qquad (14)$$

Summary of Lienhard and Eichhorn's Model:

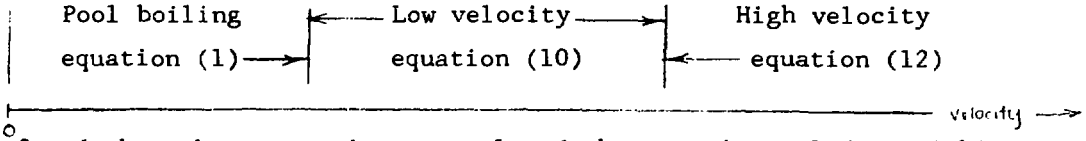

It was found that these equations correlated the experimental data within ± 20 %. However, systematic bias occurs such that the water and isopropanol data are consistently lower than the Freon and methanol data.

KATTO AND HARAMURA'S HYDRODYNAMIC INSTABILITY MODEL

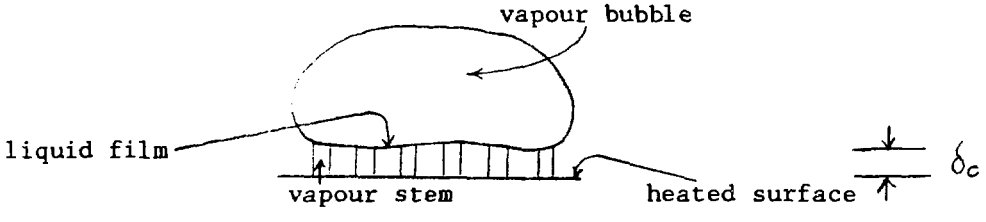

According to Katto and Haramura's model, during boiling, a thin liquid film is formed on the heated surface. The vapour bubble is nourished from the vapour stems in the liquid film and the vapour blanket restricts the feed of liquid from the bulk region to the film. CHF occurs when the liquid film dries up.

In the 'jet-like' flow pattern, the vapour escape configuration is

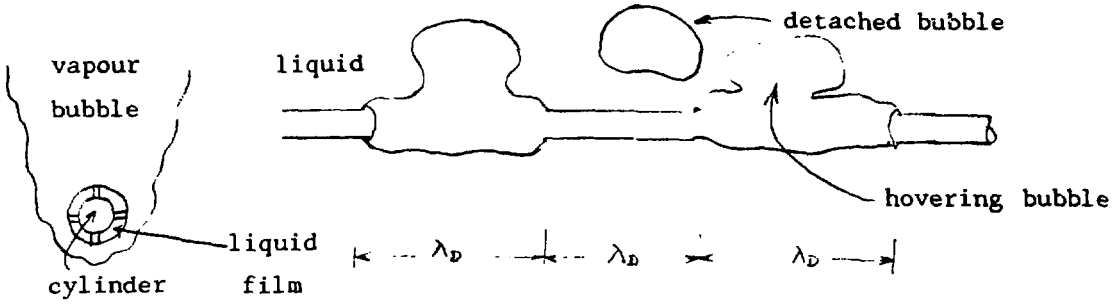

The most susceptible Taylor wavelength is given by

$$\lambda_D = \sqrt{3}\,\pi \left[\frac{\sigma}{g(\rho_f - \rho_v)}\right]^{1/2} \left[1 - \frac{4\sigma}{d^2 g(\rho_f - \rho_v)}\right]^{-1/2} \tag{15}$$

and the volumetric growth rate of the bubble is

$$V_1 = \frac{\pi d \lambda_D q}{\rho_v h_{fg}} \tag{16}$$

The bubbles leave heater periodically at a mean time interval τ_D, and CHF appears when the liquid film evaporates out at the end of the hovering period τ_D. Heat balance gives:

$$\tau_D q A_w = \rho_f \delta_c (A_w - A_v + A_w \delta_c / d) h_{fg} \tag{17}$$

with three unknowns δ_c, A_v/A_w, τ_D.

From hydrodynamic instability analysis,

$$\delta_c = \frac{\lambda_H}{4} = \frac{\pi}{2}\sigma \frac{\rho_f + \rho_v}{\rho_f \rho_v} \left(\frac{A_v}{A_w}\right)^2 \left(\frac{\rho_v h_{fg}}{q}\right)^2 \tag{18}$$

and $$A_v/A_w = 0.584\,(\rho_v/\rho_f)^{0.2} \tag{19}$$

From analysis of the motion of a growing bubble,

$$\tau_D = \left(\frac{3}{4\pi}\right)^{1/5} \left[\frac{4(\varepsilon\rho_f + \rho_v)}{g(\rho_f - \rho_v)}\right]^{1/5} V_1^{1/5} \left[1 + \frac{4}{\tau_1^2} \frac{(\varepsilon\rho_f + \rho_v)}{g(\rho_f - \rho_v)} u\right]^{-1/2} \tag{20}$$

where $\varepsilon = \frac{1}{16}$

Solving equations (15) to (20), assuming $A_v/A_w \ll 1$

$$\frac{q_{co}}{q_{co,2}} = \left(\frac{\sqrt{3}}{k'}\right)^{1/16} \left[1 + \frac{1}{2(k')^2}\right]^{1/32} \left[1 + 0.156 \left(\frac{\rho_v}{\rho_f}\right)^{0.4} \left(1 + \frac{\rho_v}{\rho_f}\right) \frac{1}{k'} \frac{1}{(q_{co}/q_{co,2})^2}\right]^{5/16} \times$$

$$\left[1 + 1.68 \frac{11/16 + (\rho_v/\rho_f)}{\left(\frac{\rho_v}{\rho_f}\right)^{0.4}\left(1 + \frac{\rho_v}{\rho_f}\right)} \cdot \frac{(q_{co}/q_{co,2})^3}{1 + 0.516\left(\frac{\rho_v}{\rho_f}\right)^{0.4}\left(1 + \rho_v/\rho_f\right)\frac{1}{k'}\frac{1}{(q_{co}/q_{co,2})^2}} u'\right]^{1/16} \tag{21}$$

which is the low velocity equation, and

$$\frac{q_{max}}{\rho_v h_{fg}} \Big/ \left[\frac{\sigma g (\rho_\ell - \rho_v)}{\rho_v^2} \right]^{1/4} = 0.131 \qquad (22)$$

$$u' = u \Big/ \left[\sigma g (\rho_\ell - \rho_v) / \rho_v^2 \right]^{1/4} \qquad (23)$$

and R' is as defined previously.

The configuration for the 'sheet-like' flow is

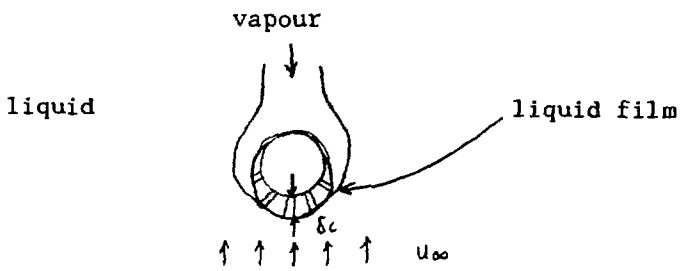

The liquid film receives saturated liquid constantly from the bulk flow at the front stagnation point with thickness δ_ℓ. CHF occurs when liquid film dries up at the rear stagnation point. Heat balance yields:

$$q \pi d/2 = \rho_\ell \delta_\ell u_\infty h_{fg} \qquad (24)$$

Solving equations (18), (19) and (24),

$$\frac{q_{co}}{G h_{fg}} = 0.151 \left(\frac{\rho_v}{\rho_\ell} \right)^{0.467} \left(1 + \frac{\rho_v}{\rho_\ell} \right)^{1/2} \left(\frac{\sigma \rho_\ell}{G^2 L} \right)^{1/3}, \quad G = \rho_\ell u_\infty \qquad (25)$$

which is the high velocity equation.

This model is found to be satisfactory for prediction at low velocity. However, the model does not work well in high velocity and transition regions.

COMPARISON BETWEEN THE TWO MODELS

1. Lienhard and Eichhorn's Model

Advantage : The model can predict burnout without knowing the full details of the instability mechanism that actually causes the burnout.

Disadvantages : The model only applies to a specific flow field. In addition, it requires the knoledge of vapour sheet thickness $\propto D$. Other limitations include :

Assumptions :

1. Vapour removal configuration.
2. Gravity effect is negligible.
3. Detached bubbles have negligible surface area per unit volume compared to the wake.
4. α does not depend on surface tension.
5. $\alpha \doteq 1$ for low u_∞ values.
6. Potential flow assumed.

2. Katto & Haramura's Model

Advantages : The model is not tied to a specific flow field, therefore, it can be used for different geometries. The model applies to both pool and flow boiling.

Disadvantages : The models is based on many assumptions that have no experimental verification. Also, there is no fixed transition point between low and high velocity equations.

Assumptions :

1. $\rho_v/\rho_f \ll 1$, usually true except at very high pressure.
2. $A_v/A_w \ll 1$
3. Initial film thickness, $\delta_c = \lambda_H/4$, same in pool and flow boiling.
4. Mechanism : CHF is caused by liquid depletion in heater surface.
5. The way the heated surface is fed with liquid is assumed.
6. Heated surface is assumed to be wettable.
7. Effect of cylinder curvature is neglected.
8. Gravity influence is insignificant to instability mechanism.
9. Zuber's peak heat flux equation (22) applies.

FURTHER DEVELOPMENT

Hasan et. al. (6) have investigated the effect of gravity on the CHF. They have found that the effect of gravity is negligible for $|G| > 10$,

where $$G \equiv \sqrt[4]{We_f\, Fr^2} \approx u_\infty / \sqrt[4]{g\sigma/\rho_f} \qquad (26)$$

They also proposed a new correlation for ϕ when $|G| > 10$:

$$\phi = 0.000917 \; \rho_f/\rho_g \left[1 + \frac{16.3}{We_f^{1/3}} \right] \qquad (27)$$

Kheyrandish et al (7) have provided theoretical prediction of α based on potential flow model. They discovered that alternating current heating could influence Helmholtz wavelength responsible for wake instability. They detected the omission of surface energy absorbed in the escaping bubbles in MESC. Mechanical energy balance then becomes

$$\frac{1}{2} \rho_g \alpha D u_g^3 - 2 u_{\infty} \sigma + \pi d \sigma / \tau = 0 \qquad (28)$$

Since $\pi d^2/4 = \alpha D (u_g + u_{\infty}) \tau$

$$\frac{u_g}{u_{\infty}} = \left(\frac{4}{\alpha We_g} \right)^{1/3} \left[1 - \sqrt{\pi St \, \phi} \right]^{1/3} \qquad (29)$$

Sadasivan and Lienhard (8) have investigated the effect of gravity in crossflow normal to gravity. They had the following findings :

1. q_{max} is the same for upflow and transverse flow regardless of gravity influence.
2. Gravity exert greater influence on a.c.-influenced burnout data.
3. Criteria for gravity- uninfluenced data :
   - A.C.- influenced : $r^2/Fr^3 \lesssim 75$
   - A.C.- uninfluenced : $r^{1.7}/Fr \lesssim 3$:
4. α was found to correlate empirically for Kheyrandish's gravity- uninfluenced correlation.
5. $\frac{\phi}{\phi_{pred}} = f(r, Fr)$

   This equation is tentative for A.C.-uninfluenced data.

Ungar and Eichhorn (9) have given a more complete hydrodynamic prediction of q_{max} based on Haggerty and Shea's stability criterion. However, it was no longer considered as an MESC. They also classified three distinct modes of vapour removal pattern:

- $G < 8$: 2-D periodic bubble breakoff
- $8 < G < 10$: transition, 3-D periodic breakoff
- $G > 10$: random breakoff

They started from the equation $\phi = \alpha (u_g / u_c + 1)$ (29)

then they used Haggerty and Shea's Helmoltz wavelength to obtain :

$$\phi = \alpha (2\pi St \sqrt{3\alpha/(2 w_g)} + 1) \quad (30)$$

for $G \leq 8$.

The value α was determined experimentally

$$\alpha = 0.200\ Fr^{c} \quad (31)$$

where $$c = 0.141\ r^{0.258} \quad (32)$$

and empirically ,

$$St = 0.947\ (Fr + 0.614)^{-1.5} \quad (33)$$

ACKNOWLEDGEMENT

The constant supervision and encouragement from Professor M. Kawaji throughout this project is gratefully acknowledged. The author also would like to thank Matthew Ko for his support and assistance in the preparation of this manuscript.

REFERENCES

1. Lienhard, J.H., and Eichhorn, R., " Peak Boiling Heat Flux on Cylinders in a Cross Flow ", Int. J. Heat Mass Transfer, Vol.19, pp 1135-1142 (1976).

2. Haramura, Y., and Katto, Y., " A New Hydrodynamic Model of Critical Heat Flux, Applicable Widely to both Pool and Forced Convection Boiling on Submerged Bodies in Saturated Liquids ", Int. J. Heat Mass Transfer, Vol.26, No.3, pp 389-399 (1983).

3. Cochran, T.H., and Andracchio, C.R., " Forced Convection Peak Heat Flux on Cylindrical Heaters in Water and Refrigerant-113 ", NASA TN D-7553, Feb.1774.

4. Sun, K.H., and Lienhard, J.H., " The Peak Pool Boiling Heat Flux on Horizontal Cylinders ", Int. J. Heat Mass Transfer, Vol.13, pp 1425-1439 (1970).

5. Lienhard, J.H., and Dhir, V.K., " Hydrodynamic Prediction of Peak Pool Boiling Heat Fluxes from Finite Bodies ", J. Heat Transfer, Trans. ASME, pp 152-158 , May 1973.

6. Hasan, M.Z., et al., " Boiling Burnout during Cross Flow over Cylinders, beyond the Influence of Gravity ", J. Heat Transfer, Trans. ASME, pp 478-484, Vol. 103, Aug 1981.

7. Kheyrandish, K., et al., " A Model for Fluid Flow during Saturated Boiling on a Horizontal Cylinder ", J. Heat Transfer, Trans. ASME, pp 485-490, Vol. 109, May 1987.

8. Sadasivan, P., and Lienhard, J.H., " Burnout of Cylinders in Flow Boiling: the Role of Gravity Influences on the Vapour Plume ", ASME/AIChE Heat Transfer Conference, Pittsburgh, PA., 1987.

9. Ungar, E.K., and Eichhorn, R., " A New Hydrodynamic Prediction of the Peak Heat Flux from the Horizontal Cylinders in Low Speed Upflow ", ASME/AIChE Heat Transfer Conference, Houston, TX, July 1988.

X-RAY SPECTRUM ANALYSIS USING FOURIER TRANSFORM TECHNIQUES

A.A. MIRZAI, J.S.C. MckEE, and G.R. SMITH

University of Manitoba Accelerator Centre, University of Manitoba, Winnipeg, Manitoba, R3T 2N2, Canada

Abstract

A digital filter is designed to separate background and statistical noise from the peaks observed in a measured X-ray spectrum by making maximum use of the Fourier transform techniques. In this approach no assumptions are made about the method of production or the functional form of the background.

1. Introduction

The process of Proton Induced X-ray Emission (*PIXE*) followed by detection of the X-ray represents a highly sensitive, multielement analytical method. The basic purpose of the method is the determination of the absolute concentrations of elemental constituents in a sample under investigation. After generating an experimental *PIXE* X-ray spectrum, the first step toward an estimate of the concentrations of elements in the sample, is to evaluate the areas of all observed peaks in the spectrum. Investigators engaged in application of this method are aware of the difficulties inherent in the exact evaluation of peak areas and, ultimately, the intensities of X-radiations from individual elements in the measured spectra. The X-ray spectra are not simple. They may contain overlapping peaks, and these features are superimposed on a not insignificant, energy-dependent background. Finally, the data show statistical fluctuations. Determination of the smallest X-ray peak detectable by this technique is complicated by the presence of this background component.

The problems of both background subtraction and noise suppression in a digitized X-ray spectrum can be treated in a number of ways. We have investigated using Fourier transform techniques utilizing an appropriately designed digital filter, as this approach has not previously been exploited successfully. In this paper we first discuss the translation invariance of the system as a method for improving or pre-conditioning data for Fourier transformation. Translational invariance requires that peaks, appearing in different regions of the spectrum have the same width. Then, we outline the design criteria for a digital filter function which, when used with Fourier transform techniques, will simultaneously suppress the noise and background components of the pre-conditioned spectra. The goal of this exercise is the estimation of the area under spectral features remaining after stripping of noise and background components from the pre-conditioned spectra has been completed and calculating the error associated with

this estimate. We describe our progress towards attaining this goal.

2. Pre-conditioning the spectrum

The greatest benefit will be obtained from a Fourier transformation incorporating a response function which is translationally invariant [1,2]. This means we require that the spectrum of interest should contain peaks having constant line-widths. Clearly, this condition is not fulfilled by Si(Li) or Ge X-ray spectra because the width varies as the square root of the energy in each case. For example, the useful working energy range of a Si(Li) detector is from less than 1 KeV up to 20 KeV. From a detector with a resolution specified as 150 to 170 eV *FWHM* at 6 KeV, the observed line-widths change from about 100 eV at 1 KeV to 250 eV at 20 KeV. However, this behavior of the line-width dependence on energy can be used to convert the observed spectrum to one containing peaks of constant width. Following the procedure of Hay [3], the linear relationship between the square of a peak width and its energy was used to perform the transformation of the energy axis of X-ray spectra and produce peaks with constant line-widths. Figure 1(a) shows a portion of an experimental spectrum of a leaf sample, taken at an incident proton energy of 40 MeV with a silicon detector and Figure 1(b) represents the pre-conditioned version of the same spectrum. In Figure 1(a) the standard deviations of visible peaks varied from 2.024 to 3.300 channels. After pre-conditioning, all the peaks in the spectrum exhibit a constant width of σ_c=3.182 channels. A function that is to be submitted to Fourier transformation needs to be "periodical" in some way that allows reasonable continuity conditions at the endpoints. then the background contribution to the spectrum can be determined without "ringing" at these points. The method selected was to increase the range of the original data, which was initially 1024 channels, to 2048 channels. Those additional channels were filled by reflecting the initial spectrum in a "mirror" located in channel 1024. The result of pre-conditioning and reflection is shown in Figure 1(c). However, expanding the length of the baseline of data from 1024 to 2048 channels must not be misconstrued as doubling the data to be fitted. The Fourier transform of these data will include an infinite number of frequencies, and while this step seems to double the number of data points, care is taken throughout the application of the technique, to keep the number of frequencies used to half the number of initial data channels.

3. Data smoothing

Let the measured data be represented as

$$m\ (E) = t\ (E) + b\ (E) + n\ (E) \qquad (1)$$

where $m\ (E)$ is the measured translationally invariant reflected data, $b\ (E)$ is background and $n\ (E)$ is the noise component. If we introduce the noise-free signal $s\ (E)$

as

$$s\ (E) = t\ (E) + b\ (E) \tag{2}$$

equation (1) can be written as follows

$$m\ (E) = s\ (E) + n\ (E) \tag{3}$$

The noise component, $n\ (E)$, is of random origin and is due principally to statistical fluctuations in the number of counts in a channel. Using Fourier transforms M(ν), S(ν) and N(ν) of $m\ (E)$, $s\ (E)$ and $n\ (E)$ respectively, we get

$$M\ (\nu) = S\ (\nu) + N\ (\nu) \tag{4}$$

where ν is the variable in the frequency/conjugate and, by analogy, can be related to inverse channel number. The components S(ν) and N(ν) can be separated by means of a filtering function $W_N(\nu)$ so that

$$S\ (\nu) = W_N\ (\nu) \times M\ (\nu) \tag{5}$$

Because these statistical fluctuations, (the noise components), are uncorrelated, channel to channel, they are attributed to high frequencies. To determine proper filter function $W_N\ (\nu)$ it is useful to plot the power spectrum $|\ M\ (\nu)\ |^2$ vs ν. Such plots for the pre-conditioned, symmetrical leaf spectrum, shown in Figure 1(c) and the pre-conditioned leaf spectrum, shown in Figure 1(b), are seen in Figures 2(a) and 2(b) respectively. Note that we can also separate the power spectra of the two components $|\ S\ (\nu)\ |^2$ and $|\ N\ (\nu)\ |^2$. The filter function $W_N\ (\nu)$ must be of a form that passes frequencies below the cutoff frequency, identified in Figure 2(b), but also eliminates those frequencies above the cutoff where the noise component $N\ (\nu)$ dominates.

4. Background subtraction

After removing the noise component, $n\ (E)$ or $N\ (\nu)$, we attempt to recover the true spectrum, $t\ (E)$, from equation (2). The most obvious feature which distinguishes background from peaks and noise is the slow variation of the background with energy compared with the faster variation of structure in the peaks. Using Fourier transforms $S\ (\nu)$, $T\ (\nu)$ and $B\ (\nu)$ of $s\ (E)$, $t\ (E)$ and $b\ (E)$ respectively in equation (2) we have, symbolically,

$$S\ (\nu) = T\ (\nu) + B\ (\nu) \tag{6}$$

Now, the problem reduces to devising a second filter function, $W_B\ (\nu)$ so that when applied to $S\ (\nu)$ recovers the sought quantity $T\ (\nu)$,

$$T\ (\nu) = W_B\ (\nu) \times S\ (\nu) \tag{7}$$

5. Filter design

Replacing for the value of $S(\nu)$ in equation (7) from equation (5) we get

$$T(\nu) = W_B(\nu) \times [W_N(\nu) \times M(\nu)] \tag{8}$$

or,

$$T(\nu) = W(\nu) \times M(\nu) \tag{9}$$

where $W(\nu)$ is the filter function with two components $W_B(\nu)$ and $W_N(\nu)$, which when convoluted with the transformed measured spectrum $M(\nu)$, produces the true spectrum $T(\nu)$. Finally, the inverse transform of $T(\nu)$ will produce the noise/background free spectrum $t(E)$ in channel number (energy) domain.

Figure 2(c) represents the required filter function $W(\nu)$, with the frequencies characteristic of the background ν_b, of the peaks, ν_{p1} and ν_{p2}, and the cutoff frequency ν_c, identified. This filter function simultaneously suppresses the noise and background components when applied to the measured spectrum $M(\nu)$ as seen from the discussion which follows.

Because the background varies smoothly over the whole spectrum, we anticipate that it is characterized by lower frequencies than those associated with the spectral peaks. Therefore, the component $B(\nu)$ in equation (6) has significant values only at low frequencies ($\nu < \nu_{p1}$)and background component of filter function, $W_B(\nu)$ will operate only in the frequency range $\nu_b \leq \nu < \nu_{p1}$. Then,

$$W_{Bi} = \sum_{i=\nu_b}^{\nu_{p1}} f_i \tag{10}$$

In view of the statistical nature of the data an important assumption can be made, namely that the count numbers in different channels are statistically independent and the distribution function can be approximated by a normal distribution. Therefore, the values of f_i were obtained by fitting a Gaussian, the near tail of the filter function in Figure 2(c), to these ν-points.

We will show later that the application of this filter function in the range $\nu_b \leq \nu \leq \nu_{p1}$ removes nearly the whole background.

now we turn our attention to the other portion of the filter function, i.e. $W_n(\nu)$, used to remove the noise component $N(\nu)$ in equation (4). As mentioned earlier, the high frequencies ($\nu \gg \nu_{p1,2}$) contribute to $N(\nu)$, i.e. they belong to statistical noise, and are more easily separated than the background component. As far as the design of the noise component of the filter function, $W_N(\nu)$, is concerned, the optimal filter proved to be a good choice for this purpose. Referring to Figure 2(b) the formula for the optimal filter can be written as

$$g(\nu) = \frac{|S(\nu)|^2}{|S(\nu)|^2 + |N(\nu)|^2}, \qquad \nu = \nu_{p1} + 1, \ldots\ldots \nu_{p2} \tag{11}$$

so that $W_N(\nu)$ will be close to unity where the noise is negligible, and close to zero where the noise is dominant. The intermediate dependence given by equation (11) turns out to be the optimal way of interpolating between these two extremes. Although there is no way to separate $|S(\nu)|^2$ and $|N(\nu)|^2$ from $|M(\nu)|^2$ alone, the power spectrum of Figure 2(b) clearly shows a signal (peaks + background) region added to a noise tail. The tail is extrapolated back into the region dominated by spectral peaks as a "noise model". Note that a flat model is used for this case. Now we draw the straight line through the power spectrum of the measured data. The difference between these two curves will be the model of the signal power. It might seem logical to assign the range of frequencies between ν_{P1} (characteristic frequency denoting the beginning of the spectral peaks) and the cutoff frequency ν_c in Figure 2(c) to be operated upon by the optimal filter. However, it is important that the filter function be a smoothly varying function of frequency so that oscillations are not introduced in the inverse transformation. A sharp cutoff in one domain implies damped oscillatory behavior in the other [4]. In order to eliminate this problem a smooth Gaussian was fitted between the characteristic frequency point ν_{p2} and the cutoff frequency ν_c. ν_{p2} is the frequency at which the values of the filter function calculated from equation (11) vary sharply. Finally, the values of the filter function in the last portion between the cutoff frequency, ν_c, and the terminal frequency point, ν_t, were made zero in order to remove that portion of the noise completely.

Based on the above discussion the relation for the noise component of the filter function, $W_N(\nu)$, to remove the noise component can be written as follows

$$W_{N_{ijk}} = \sum_{i=\nu_{p1}+1}^{\nu_{p2}} g_i + \sum_{j=\nu_{p2}+1}^{\nu_c} h_j + \sum_{k=\nu_c+1}^{\nu_t} z_k \tag{12}$$

where g_i represents those values of the filter function obtained from the formula of optimal filter (equation 11), h_j corresponds to the smooth Gaussian, far tail of the filter function, and finally the values corresponding to z_k are equal to zero.

6. Application of the filter function to the data and the experimental results

In section 5 we discussed the filter design and constructed the filter function from the relation

$$W(\nu) = W_B(\nu) \times W_N(\nu) \tag{13}$$

where $W_B(\nu)$ and $W_N(\nu)$ are the background and the noise components of the filter function. By applying this filter function to the Fourier transformed measured data, $M(\nu)$, the true function (peaks only), $T(\nu)$, will be obtained

$$T(\nu) = W(\nu) \times M(\nu) \tag{14}$$

An inverse Fourier transform of $T(\nu)$ will provide the background and noise free spectrum, $t(E)$, in channel number domain.

Although the number of frequencies, ($\nu_b \leq \nu \leq \nu_{p1}$), assigned for background subtraction might be varying under different circumstances, in fact only first few low frequencies contribute. Figure 3(a) represents the fit of the background function to the X-ray spectrum of the leaf specimen and Figure 3(b) shows the corresponding background subtracted (true spectrum) when the following filter parameters are used.

$\nu_b = 1$, $\nu_{p1} = 4$

When a Gaussian is fitted to the first four ν-points, the following values for the first four points were obtained.

$f_1 = 0.655, f_2 = 0.775, f_3 = 0.952, f_4 = 1.000$

After fixing ν_b and ν_{p1} to the above values, the background function is insensitive to the choice of the frequency, ν_{p2}, and the cutoff frequency, ν_c. By having $\nu_b = 1$, it is only the value of ν_{p1} which is the decisive factor for background subtraction.

Note however that there is "ringing" under the peaks and an "oscillation" that extends from about channel 400 to channel 700 in Figure 3(a). This problem will have to be addressed and the work is proceeding. Eventually, it is anticipated that the accuracy and precision of concentration measurements using the technique described above will be considerably superior to earlier methods used.

7. Summary

The Fourier transform has been used as another approach for investigating the information content of X-ray spectra. The criteria for the design of a digital filter have been discussed. Using Fourier transform techniques without resorting to the conventional fitting methods, allows the subtraction of most of the background and suppresses statistical noise components. The major advantages over conventional techniques are that the shape of the background function need not be known explicitly and by using minimum number of free parameters, a decrease in physical intervention in the data extraction procedure can be affected.

References

[1] T.J. Kennett, W.V. Prestwich and A. Robertson, Nucl. Instr. and Meth. 151(1978)285.

[2] T.J. Kennett, W.V. Prestwich and A. Robertson, Nucl. Instr. and Meth. 151(1978)293.

[3] H.J. Hay, Nucl. Instr. and Meth. B10/11(1985)624.

[4] A.V. Oppenheim and R.W. Schafer, Digital signal processing (1975), Englewood Cliffs, New Jersey, Prentice Hall.

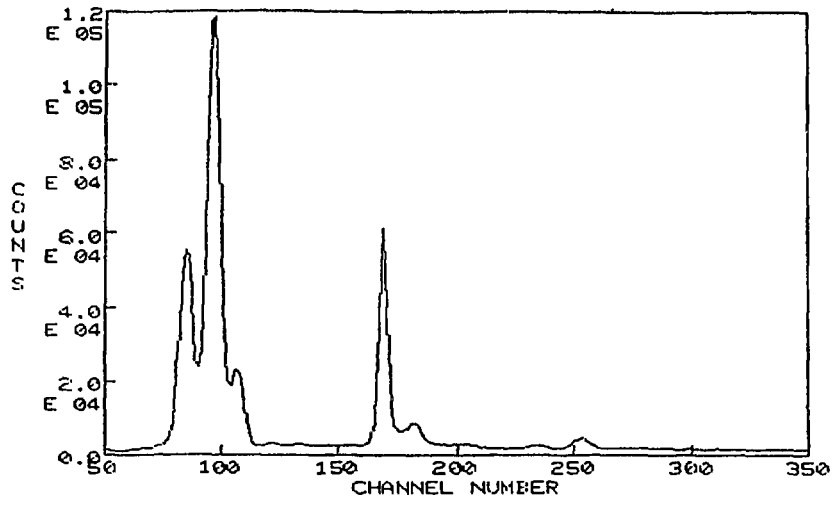

Figure 1(a) Typical X-ray spectrum of a leaf sample at an incident proton energy of 40 MeV (silicon detector).

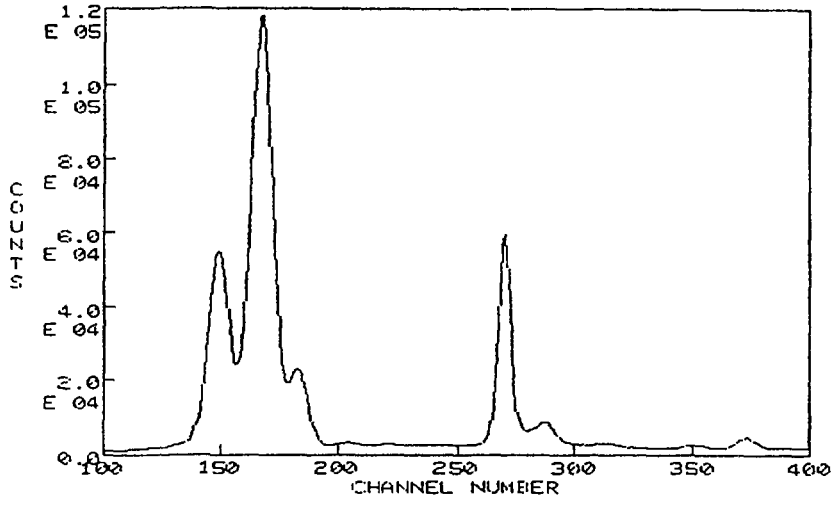

Figure 1(b) Spectrum of the same leaf sample as in Figure 1(a) after pre-conditioning to produce constant-width peaks.

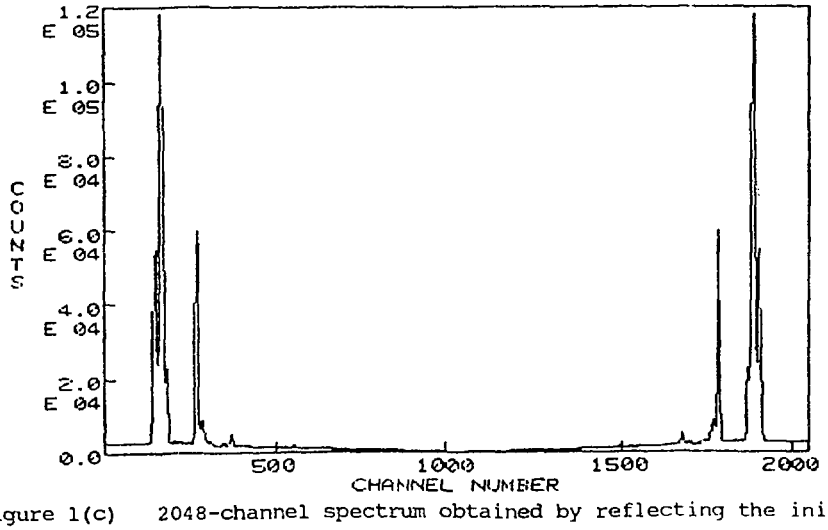

Figure 1(c) 2048-channel spectrum obtained by reflecting the initial pre-conditioned spectrum in a "mirror" located in channel 1024.

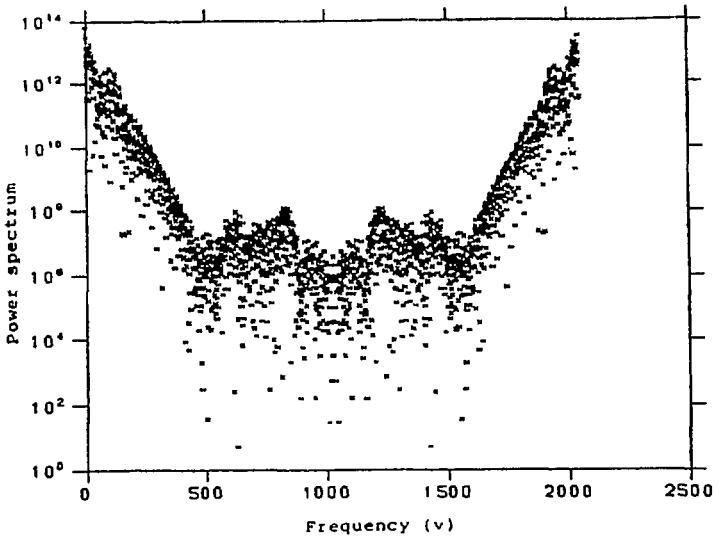

Figure 2(a) Power spectrum of the data of Figure 1(c).

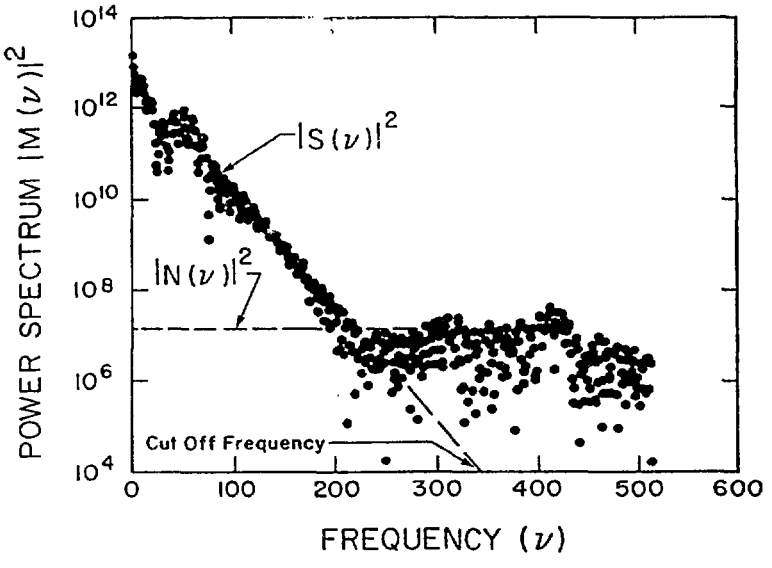

Figure 2(b) Power spectrum of the pre-conditioned leaf sample.

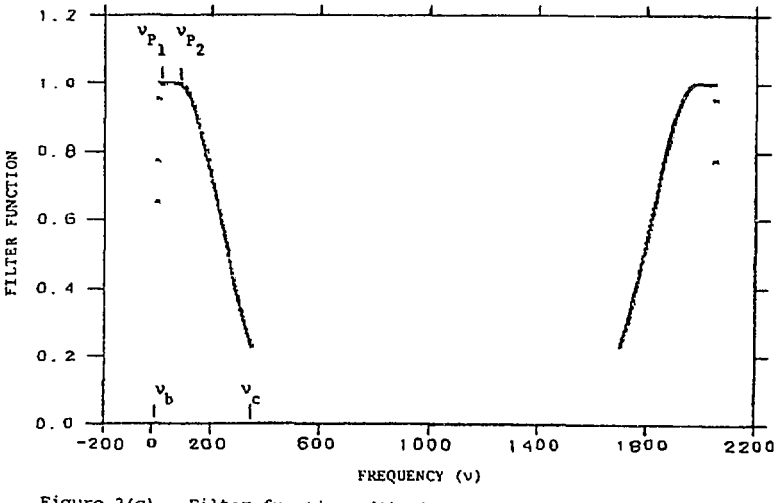

Figure 2(c) Filter function with the frequencies characteristic of the background, ν_b, of the peaks, ν_{p_1} and ν_{p_2}, and the cutoff frequency ν_c.

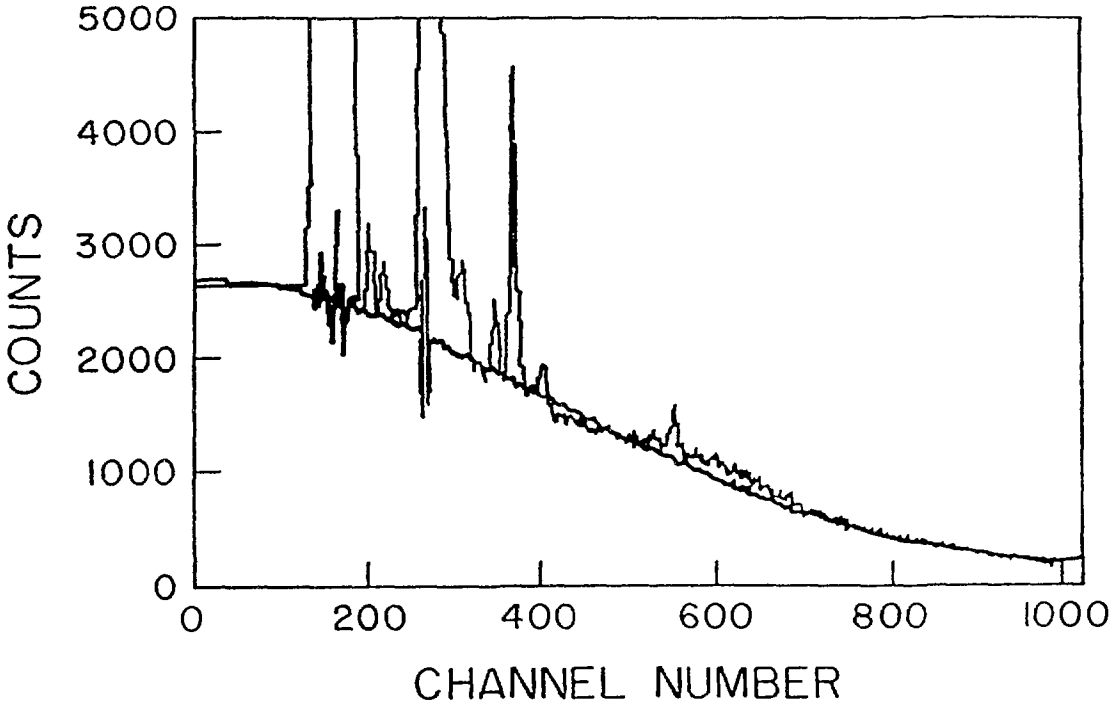

Figure 3(a) Background function fitted to the X-ray spectrum of the leaf sample.

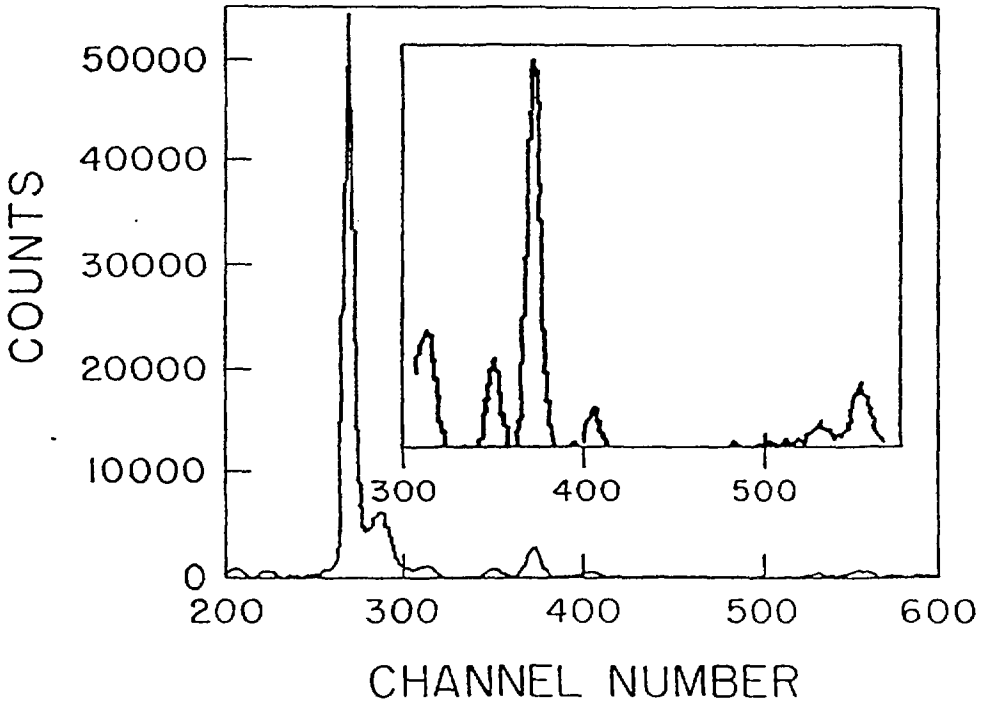

Figure 3(b) Background-free peaks of the X-ray spectrum of the leaf sample.

THE EFFECT OF BUNDLE GEOMETRY ON VOID FRACTION AND FRICTION PRESSURE DROP IN ADIABATIC TWO-PHASE FLOW ACROSS A HORIZONTAL ROD BUNDLE

R.Dowlati

Department of Chemical Engineering and Applied Chemistry
University of Toronto, Toronto, Ontario M5S 1A4

ABSTRACT

Extensive work has been performed on two-phase heat transfer and pressure drop for in-tube and parallel flow geometries. However, only limited information is available for use in vertical, cross-flow boiling over a horizontal tube bundle. Since many heat exchangers employed in the process industries are used to boil fluids and involve two-phase flow on the shell-side, such as steam generators in the CANDU reactors, it is important to have a clear and concise understanding of the boiling and two-phase flow characteristics. Such information may help in preventing the over-design of boilers and to predict critical heat flux (CHF) in the tubes.

In this work, the hydrodynamics of two-phase flow in three geometrically different horizontal rod bundles are studied. Void fraction and pressure drop characteristics have been experimentally investigated for adiabatic, vertical, air/water two-phase flow across the horizontal rod bundles at near atmospheric pressures. The effect of bundle geometry is analyzed and the new proposed correlations are and applied to predict the total pressure drop in boiling freon experiments.

Each bundle contained 20 rows of 5 rods, each rod 80 mm in length. In bundle 'A', the rods (19 mm O.D.) were placed in a square in-line geometry with a pitch-to-diameter ratio (P/D) of 1.3. Bundle 'B' had the same in-line array with P/D=1.75 and 12.7 mm O.D. rods. In bundle 'C', the rods (19 mm O.D.) were placed in a staggered (60 degree) layout with P/D=1.3.

Air injected through a porous tube into the water stream below the bundle provided a relatively uniform two-phase mixture. A single-beam gamma densitometer was used to measure the void fraction at various elevations in the bundle and pressure drop across the bundle was measured using a differential pressure transducer. The data were obtained for mass velocity, G, ranging from 27 to 818 kg/m^2 s and quality from 2×10^{-4} to 0.33. Details of the experimental procedure and the results are given in refs. [1,2], and only briefly outlined below.

The void fraction profiles were generally uniform within each of the three bundles and thus a bundle average void fraction was obtained by averaging the void fraction profiles. Also for all bundles, it was found that the homogeneous flow model significantly overpredicted the void fraction data and also showed a strong mass velocity effect. In correlating the present data, the Martinelli parameter, commonly used to correlate void fraction data for in-tube flow, was also found to be unsatisfactory for the bundles tested because of the strong mass velocity effect.

The present void fraction data from the three bundles were also to be well correlated in terms of the dimensionless gas velocity, j_g^*, given by Wallis [3]. Very little difference was observed in the void fraction measurements between the three bundles for a given value of j_g^*. The correlation developed is similar

in form to that suggested by Chisholm and Laird [4] for two-phase flow in circular tubes.

The frictional pressure drop was obtained from the total pressure drop measurement by neglecting the accelerational component and subtracting the gravity component, which was calculated using the void fraction data. For G>200 kg/m² s, the two-phase friction multiplier, ϕ_ℓ^2, calculated from the frictional pressure drop data could be well correlated in terms of the Martinelli parameter for all three bundles.

In order to test the applicability of the void fraction and two-phase friction multiplier correlations under boiling two-phase flow conditions, the total pressure drop data of Hsu [5] and Reinke [6] were analyzed. Both carried out boiling freon experiments in an electrically heated 5x27 tube bundle. Hsu's in-line array bundle had P/D=1.3 and that of Reinke's was of the same P/D, however, with a staggered array. Most of the pressure drop data from both studies were well predicted within ±20%. (Fig.3).

REFERENCES

1. Dowlati, R., Kawaji, M. and Chan, A.M.C., "Void Fraction and Friction Pressure Drop in Two-Phase Flow Across a Horizontal Tube Bundle," *AIChE Symposium Series*, v. 84, no. 263, 1988, pp. 126-132.
2. Dowlati, R., Chan, A.M.C. and Kawaji, M., "Pitch-to-Diameter Effect on Two-Phase Flow Across an In-Line Tube Bundle," submitted to the AIChE Journal, 1989.
3. Wallis, G.B., *One-Dimensional Two-Phase Flow*, McGraw-Hill, New York, 1972.
4. Chisholm, D. and A.D.K. Laird, "Two-Phase Flow in Rough Tubes," *ASME Trans.*, v. 80, 1958, pp. 276-286.
5. Hsu, J.T., "A Parametric Study of Boiling Heat Transfer in Horizontal Tube Bundles," Ph.D. Thesis, University of Wisconsin, Milwuakee (Dec.1987).
6. Reinke, M.J., "A Comparison of the Boiling Heat Transfer and Two-Phase Pressure Drop Characteristics of an Inline and a Staggered Tube Bundle," M.Sc. Thesis, Univ. Wisconsin, Milwaukee (Dec., 1987).